THE ELASTIC SCATTERING OF PROTONS FROM Li^6 NUCLEI

Thesis by

James A. McCray

In Partial Fulfillment of the Requirements

for the Degree of

Doctor of Philosophy

California Institute of Technology

Pasadena, California

1962

ABSTRACT

The differential elastic scattering cross section for protons from Li^6 nuclei has been measured for energies from 0.45 Mev to 2.9 Mev at six different angles. A measurement was also made of the $Li^6(p, \alpha)He^3$ reaction cross section in order to determine its absolute value. The scattering data is consistent with an s- and p-wave phase shift analysis with a p-wave $5/2^-$ state at about $E_p(Lab) = 1.84$ Mev, with resonant parameters consistent with the parameters previously assigned to the corresponding mirror level in Li^7, and a very broad s-wave $1/2^+$ state near or above $E_p(Lab) = 2.76$ Mev. The data is also consistent with a p-wave $3/2^-$ state with a different behavior of the s-wave scattering at higher energies, if an appropriate channel spin mixture is chosen. A p-wave $1/2^-$ state is not consistent with the data. No evidence for the existence of a $3/2^+$ state near $E_p(Lab) = 1$ Mev with an appreciable Γ_p/Γ has been found.

The stopping cross section for protons on lithium follows the Bloch formula from 0.8 Mev to 2.8 Mev.

ACKNOWLEDGMENTS

The author wishes to express his gratitude to Dr. C. A. Barnes for suggesting this work and for his continued encouragement and guidance throughout the past years. The advice given by Dr. R. F. Christy on the theoretical analysis of the data was also greatly appreciated. The author would also like to thank the faculty and staff of the Kellogg Radiation Laboratory for providing such a stimulating atmosphere in which to work. The cheerful assistance of Mrs. Barbara Zimmerman in performing part of the calculations and the patient understanding and help from the author's wife, Diane, were major factors in the bringing of this work to completion.

TABLE OF CONTENTS

I. INTRODUCTION

One of the most informative techniques available to the experimental nuclear physicist is the elastic scattering of charged particles from nuclei. The coherence of the various scattering processes gives rise to interference terms in the scattering cross section between the Rutherford amplitudes and the nuclear amplitudes. These additional terms frequently assist in the determination of many of the parameters describing the nuclear states involved. These parameters may then be compared to the predictions of nuclear theory.

Perhaps the most interesting nuclei to study are the light mirror nuclei at low energies because here one usually has well-separated anomalies in the elastic scattering and reaction cross sections which may be related to resonant behavior in the compound nucleus. The charge symmetry of nuclear forces may then be checked by comparing the level structure of the mirror nuclei.

A very interesting case, which has already been the object of many studies, is that of Li^7 and Be^7 (Brown, 1951; Ajzenberg-Selove, 1959). The first three levels of Be^7 have been well established experimentally, but the region between 6 and 8 Mev has not been fully studied. This region may be reached by bombarding a sample of Li^6 nuclei with a well-defined beam of protons and observing the particles which come out. The following possibilities must be considered:

$$Li^6 + p \rightarrow Be^{7*} \rightarrow \begin{cases} Li^6 + p & (a) \\ He^3 + \alpha & (b) \\ Be^7 + \gamma & (c) \\ Li^{6*} + p' & (d) \\ Be^6 + n & (e) \\ Li^5 + d & (f) \\ He^4 + d + p & (g) \end{cases}$$

The region of interest above corresponds to protons of energy between about 0.4 and 3.0 Mev. Although the three-body break-up threshold (g) occurs at 1.716 Mev, the energy in the center of mass system available to the three particles will not be sufficient over the region studied to allow the particles to penetrate the coulomb barrier. However, if the deuteron and the proton combine to form a He^3 particle, then there is enough energy available for separation. Thus the contribution of the three-body break-up compared to the α-He^3 break-up may be neglected over the region studied. The (e) and (f) modes need not be considered since there is not enough energy available in the compound nuclear system to allow such decays. The inelastic scattering process (d) requires at least a proton energy of 7/6 (2.184) Mev to reach the first excited state in Li^6 and at least d-wave protons, so this process would not be important except perhaps in the high energy part of the region considered. The radiative capture of protons (c) has been studied (Bashkin, 1955; Warren, 1956) up to 0.75 Mev and has been found to have a cross section of about 10^{-31} cm^2. Gamma rays were observed to the ground state and to the first excited state of Be^7, and the

angular distributions obtained indicated that, if the process occurred through a compound state, it would have to have negative parity. McCray and Smith (1962) have also looked at the radiative capture of protons by Li^6 at higher energies (1 Mev to 2 Mev) and have found large $\cos^2\theta$ terms in the angular distributions. However, the yield curve increases with energy without exhibiting resonant behavior.

The reaction $Li^6(p, \alpha)He^3$ (b) has been studied by several investigators (Bashkin, 1951; Marion, 1956) and all have found a broad resonance at about 1. 85 Mev and evidence of a broad structure at lower energies. There is, however, some confusion as to the value of the cross section, although all investigators obtain values in the region 10^{-27} to 10^{-25} cm^2. Marion et al. (Marion, 1956) measured angular distributions for this reaction and found large $\cos\theta$ terms which might indicate the presence of two compound nuclear states of opposite parity. They assumed the 1. 85 Mev resonance to be formed by p-wave protons since they did not nave to consider terms higher than $\cos^2\theta$ in their angular distribution. From the integrated cross section they were able to fit the 1. 85 Mev resonance with a single level Breit-Wigner curve assuming $J^\pi = 5/2^-$ for the state. With this assignment for the 1. 85 Mev resonance, the other interfering state would then have + parity; and if formed by s-wave protons, would have to be $3/2^+$, since the $5/2^-$ state can only be formed in the 3/2 spin channel. The elastic scattering of protons from Li^6 (a) was investigated by Bashkin and Richards (1951) only at one back angle with a natural Li target. They found an elastic scattering anomaly with

a cross section of about 10^{-25} cm^2. In the above region of interest it is seen that the radiative decay mode is negligible compared to particle decay, so we have here a system with essentially two channels, scattering and one reaction, and perhaps two broad interfering levels.

It was the purpose of this investigation to measure experimentally the elastic scattering of protons from Li^6 nuclei in the range E_p = 0.45 Mev to 2.9 Mev, to check the $Li^6(p,\alpha)He^3$ reaction, and to then analyze the above data in order to deduce the quantum numbers of the states involved.

II. DISCUSSION OF THE EXPERIMENT

A. APPARATUS

This experiment was performed in two parts. The low energy work from 0.45 Mev to 1.2 Mev involved the use of the 2-Mev Van de Graaff accelerator, 80° electrostatic analyzer, 2.5-inch scattering chamber, 10.5-inch magnetic spectrometer and cesium iodide scintillation counter with amplifier and scaler, all of which have been previously described. (Lauritsen, 1941; Fowler, 1947; Snyder, 1950; Mozer, 1956) The work from 1.0 Mev to 2.9 Mev was accomplished with the use of the 3-Mev Van de Graaff accelerator, 90° electrostatic analyzer, 6-inch scattering chamber, 16-inch magnetic spectrometer and a cesium iodide scintillation counter like the one above. The 6-inch scattering chamber with target holder and furnace was constructed during the course of this experiment and will be discussed in more detail in the section on target preparation.

B. THICK TARGET TECHNIQUE

1. Derivation of Equations

Consider now the situation described by figure 1a. A beam of particles of known energy E_{1B} impinges upon a thick target. Some of the particles scatter from the front surface or produce reactions at the front surface, and the resultant particles leave with energy E_{2B}. Others penetrate the target and scatter or interact at various depths inside. For any scattering or reaction event, E_2 is determined non-relativistically by conservation laws to be

$$E_2 = \alpha(E_1, \theta)E_1 \tag{1}$$

where

$$\alpha^{1/2} = \mu \pm (w + \mu^2)^{1/2} \tag{2}$$

$$\mu = \frac{(M_1 M_2)^{1/2}}{M_1 + M_3} \cos\theta \tag{3}$$

$$w = \frac{M_3}{M_2 + M_3} \frac{Q}{E_1} + \frac{M_3 - M_1}{M_2 + M_3} \tag{4}$$

M_0 = mass of target nucleus

M_1 = mass of incoming particle

M_2 = mass of outgoing particle

M_3 = mass of residual nucleus

E_0 = kinetic energy of target nucleus

E_1 = kinetic energy of incoming particle

E_2 = kinetic energy of outgoing particle

E_3 = kinetic energy of residual nucleus

θ = laboratory angle between incoming particle M_1 and outgoing particle M_2

$$Q = E_3 + E_2 - E_1 - E_0$$

The magnetic spectrometer will accept particles of energy $E_{20} \pm (\Delta E_{20}/2)$. The energy E_{20} may be set so that ΔE_{20} corresponds only to particles emerging from a definite lamina Δs at a depth s inside the target. The spectrometer accepts particles which leave the target within a certain solid angle Ω_L. The number N of detected particles from a reaction or scattering process is proportional to the number of incident particles impinging on the target,

which is equal to the total charge collected divided by the charge per particle, to the number of target nuclei per unit area facing the beam, and to the solid angle accepted by the magnetic spectrometer. The proportionality factor is defined as the cross section and is a function of the incident energy and the angle of observation. Thus

$$N = \frac{CV}{Ze} \int_{\theta}\int_{\phi}\int_{s} \frac{d\sigma(E_1,\theta)}{d\Omega} \frac{n\, ds}{\cos\theta_1} d\Omega \tag{5}$$

where n is the number of target nuclei per unit volume, θ and ϕ are polar angles with respect to the beam direction and Z axis, and θ_1 is shown in figure 1a.

The stopping power $\epsilon(E)$ is defined as

$$\epsilon(E) = -\frac{1}{N_s} \frac{dE}{dx} \tag{6}$$

where N_s is the number of stopping atoms per unit volume. From figure 1a, one has then the following relations:

$$\frac{1}{N_s} \int_{E_{1B}}^{E_1} \frac{dE}{\epsilon(E)} = -\frac{s}{\cos\theta_1} \tag{7}$$

$$\frac{1}{N_s} \int_{E_2}^{E_{20}} \frac{dE}{\epsilon(E)} = -\frac{s}{\cos\theta_2} \tag{8}$$

where θ_2 is defined in figure 1a.

In order to proceed further with equation 5, one must change variables from s to E_{20}, giving

$$N = \frac{CV}{Ze} \frac{n}{\cos \theta_1} \int_{\theta} \int_{\varphi} \int_{E_{20}} \frac{d\sigma(E_1, \theta)}{d\Omega} \frac{\partial s}{\partial E_{20}} dE_{20} d\Omega \tag{9}$$

Equations 7 and 8 may be combined to give

$$s = - \frac{\cos \theta_2}{N_s} \int_{E_2}^{E_{20}} \frac{dE}{\epsilon(E)} = - \frac{\cos \theta_1}{N_s} \int_{E_{1B}}^{E_1} \frac{dE}{\epsilon(E)} \tag{10}$$

which may then be differentiated with respect to E_{20} to give

$$\frac{\partial s}{\partial E_{20}} = - \frac{\cos \theta_2}{N_s} \left[\frac{1}{\epsilon(E_{20})} - \frac{\partial E_2 / \partial E_{20}}{\epsilon(E_2)} \right] = - \frac{\cos \theta_1}{N_s} \frac{\partial E_1 / \partial E_{20}}{\epsilon(E_1)} \tag{11}$$

This assumes E_{1B} and $\cos \theta_1$ constant.

Now

$$\frac{\partial E_2}{\partial E_{20}} = (\partial E_2 / \partial E_1) \, (\partial E_1 / \partial E_{20}) \tag{12}$$

Hence

$$\frac{\partial E_1}{\partial E_{20}} = \frac{1}{\epsilon(E_{20}) \left[\frac{1}{\epsilon(E_2)} \frac{\partial E_2}{\partial E_1} + \frac{1}{\epsilon(E_1)} \frac{\cos \theta_1}{\cos \theta_2} \right]} \tag{13}$$

and

$$\frac{\partial s}{\partial E_{20}} = - \frac{\cos \theta_1}{N_s \epsilon(E_{20})} \left[\frac{1}{\frac{\cos \theta_1}{\cos \theta_2} + \frac{\epsilon(E_1)}{\epsilon(E_2)} \left(\frac{\partial E_2}{\partial E_1} \right)} \right] \tag{14}$$

Thus

$$N = \frac{CV}{Ze} \frac{n}{N_s} \int_{\theta} \int_{\phi} \int_{E_{20}} \frac{\frac{d\sigma}{d\Omega}(E_1, \theta) dE_{20} d\Omega}{\epsilon(E_{20}) \left[\frac{\cos \theta_1}{\cos \theta_2} + \frac{\epsilon(E_1)}{\epsilon(E_2)} \left(\frac{\partial E_2}{\partial E_1} \right) \right]} \tag{15}$$

If $\frac{d\sigma}{d\Omega}(E_1, \theta)$ is a slowly varying function of θ and E_1, if $\epsilon(E_{20})$ is a slowly varying function of E_{20}, and if $\partial E_2/\partial E_1$ is a slowly varying function of E_1, then equation 15 may be integrated to give

$$N = \frac{CV}{Ze} \frac{n}{N_s} \frac{\frac{d\sigma}{d\Omega}(E_1, \theta)\, \Omega_L \Delta E_{20}}{\epsilon(E_{20})\left[\frac{\cos\theta_1}{\cos\theta_2} + \frac{\epsilon(E_1)}{\epsilon(E_2)}\left(\frac{\partial E_2}{\partial E_1}\right)\right]} \tag{16}$$

where $\frac{d\sigma}{d\Omega}(E_1, \theta)$ now is the cross section averaged over the magnetic spectrometer window, and Ω_L is the laboratory solid angle seen by the magnetic spectrometer. The energy spread ΔE_{20} accepted by the magnetic spectrometer is then related to the momentum resolution of the spectrometer $R = \frac{p}{\Delta p}$ by

$$\Delta E_{20} = \frac{2E_{20}}{R} \tag{17}$$

The equation then for the experimentally determined laboratory cross section is

$$\frac{d\sigma}{d\Omega}(E_1, \theta) = \frac{N_s}{n}\left(\frac{ZeR}{2CV\Omega_L}\right) \epsilon(E_{20})\left[\frac{\cos\theta_1}{\cos\theta_2} + \frac{\epsilon(E_1)}{\epsilon(E_2)}\left(\frac{\partial E_2}{\partial E_1}\right)\right]\frac{N}{E_{20}}$$

A further approximation may be made, if one looks at a lamina close to the front of the thick target. Then $\epsilon(E_1) \simeq \epsilon(E_{1B})$ and $\epsilon(E_2) \simeq \epsilon(E_{20})$ so equation 18 becomes

$$\frac{d\sigma}{d\Omega}(E_1, \theta) = \frac{N_s}{n}\left(\frac{ZeR}{2CV\Omega_L}\right)\left[\left(\frac{\partial E_2}{\partial E_1}\right)\epsilon(E_{1B}) + \frac{\cos\theta_1}{\cos\theta_2}\epsilon(E_{20})\right]\frac{N}{E_{20}} \tag{19}$$

For elastic scattering $\partial E_2/\partial E_1 = \alpha$ which now is a function of angle

only. One should see the thesis of Bardin (1961) for a more general discussion of the thick target equation.

Since the above is the laboratory cross section at energy E_1, one must find a relation between E_1 and the experimentally determined quantities E_{1B} and E_{20}. From equation 10 one may write

$$\int_{E_{1B}}^{E_1} \frac{dE}{\epsilon(E)} = \frac{\cos\theta_2}{\cos\theta_1} \int_{E_2}^{E_{20}} \frac{dE}{\epsilon(E)} \tag{20}$$

Now if $\epsilon(E)$ is a slowly varying function of E over the range E_{1B} to E_1 and E_2 to E_{20}, then the following approximation is sufficiently accurate

$$\frac{E_1 - E_{1B}}{\epsilon(\overline{E}_1)} = \frac{\cos\theta_2}{\cos\theta_1} \frac{E_{20} - E_2}{\epsilon(\overline{E}_2)} \tag{21}$$

where $\overline{E}_1$ and $\overline{E}_2$ are intermediate average energies. In order to solve this equation for E_1, one must then use equation 1 which gives E_2 as a function of E_1. For the particular case of elastic scattering, equations 1 and 21 may be combined to give

$$E_1 = \frac{\frac{\cos\theta_1}{\cos\theta_2}\epsilon(\overline{E}_2)E_{1B} + \epsilon(\overline{E}_1)E_{20}}{\frac{\cos\theta_1}{\cos\theta_2}\epsilon(\overline{E}_2) + \alpha\epsilon(\overline{E}_1)} \tag{22}$$

The stopping powers in this equation may first be evaluated at E_{1B} and E_{20} and an E_1 determined. Then with $\epsilon(\overline{E}_1) = \epsilon(\frac{E_{1B}+E_1}{2})$ and $\epsilon(\overline{E}_2) = \epsilon(\frac{E_{20}+\alpha E_1}{2})$ a new E_1 is determined. This iterative procedure is continued until E_1 is stable. If one is looking near the

front edge of the target, usually the first approximation is sufficient, and as one moves back into the target, one or more iterations become necessary. For the case of a reaction one must first estimate what E_1 might be, determine $a(E_1, \theta)$ from equations 2, 3, and 4, use equation 22 to compute E_1 and then iterate until stability in E_1 is reached. Also for the case of a reaction one must use

$$\frac{\partial E_2}{\partial E_1} = E_1 \frac{\partial a}{\partial E_1} + a = a \mp \frac{\frac{M_3 Q}{M_2 + M_3} a^{1/2}}{(w^2 + \mu^2)^{1/2} E_1} \tag{23}$$

in equations 18 and 19.

In order to compare the measured cross sections with the theoretical equations, a conversion must be made to the center of mass system, using

$$\left(\frac{d\sigma}{d\Omega}\right)_{CM} = \frac{d\Omega_L}{d\Omega_{CM}} \left(\frac{d\sigma}{d\Omega}\right)_L \tag{24}$$

where

$$\frac{d\Omega_L}{d\Omega_{CM}} = \frac{(1-y^2)^{1/2}}{[(1-y^2)^{1/2} + z]^2} \tag{25}$$

with

$$y = x \sin \theta_L$$

$$z = x \cos \theta_L$$

and

$$x^2 = \frac{\frac{M_1 M_2}{M_0 M_3}}{\left[1 + \frac{M_0 + M_1}{M_0} \frac{Q}{E_1}\right]}$$

In the above work E_{1B} and E_{20} have been referred to as

measured quantities. The energy E_{1B} is that of the incoming beam of particles and is determined by the use of a cylindrical electrostatic analyzer. For such an instrument the energy of a particle passing through a circular equilibrium orbit is

$$E_{1B} \simeq \frac{ZeV}{2 \ln \frac{r_1}{r_2}} \left(1 + \frac{E_{1B}}{2M_0c^2}\right) \tag{27}$$

where r_1 and r_2 are the inner and outer radii of the cylindrical analyzer, V is the voltage across the plates, Ze is the charge per incident particle, and M_0c^2 is the rest energy of the incident particle.

A small fraction of the voltage V is measured by a potentiometer, so equation 27 may be written

$$E_{1B} = ZC_{EA}V_{EA}\left(1 + \frac{E_{1B}}{2M_0c^2}\right) \tag{28}$$

The constant C_{EA} is then determined by the use of a well-known resonant or threshold reaction.

The energy E_{20} is that of the outgoing particles and is measured by the use of a double-focusing magnetic spectrometer. The energy of a particle passing through an instrument of this kind is

$$E_{20} \simeq \frac{(ZeBr)^2}{2M_0c^2}\left[1 - \left(\frac{ZeBr}{2M_0c^2}\right)^2\right] \tag{29}$$

where B = magnetic field at particle orbit, and r = radius of circular orbit.

The magnetic field is determined by a constant torque fluxmeter so equation 29 may be written

$$E_{20} \simeq \frac{Z^2 C_{MS}}{M_0 I^2} \left(1 - \frac{E_{20}}{2M_0 c^2}\right) \tag{30}$$

where I is the fluxmeter coil current. The constant C_{MS} is determined by scattering particles of known energy from the front surface of a thick target of heavy nuclei.

If at some fixed angle one plots the number of particles counted, for a definite charge collected, as a function of fluxmeter current, the resulting graph is called a spectrometer profile. Figures 2 through 6 illustrate such profiles.

2. Following Procedure

The object of the experiment is to obtain the scattering cross section as a function of energy (excitation curve) and of angle (angular distribution). However, to take a profile at each energy and angle would be almost prohibitive in the time required. Fortunately it is not necessary, for one can pick a depth within the target, corresponding to some point upon the Li^6 profile and then follow along at approximately the same depth within the target as the incident energy or spectrometer angle is varied. Assume that the difference between the energy of the particles seen by the magnetic spectrometer E_{20} and that of the particle originating in the front surface αE_{1B} is always a certain fraction of the energy αE_{1B}. Then

$$aE_{1B} - E_{20} = KaE_{1B} \tag{31}$$

or

$$E_{20} = (1 - K)aE_{1B}$$

In terms of the fluxmeter current this becomes approximately

$$I = \left[\frac{C_{MS} Z^2}{M_0 E_{20}} \right]^{1/2} = \left[\frac{C'_{MS}}{E_{20}} \right]^{1/2} = \left[\frac{C'_{MS}}{1-K} \right]^{1/2} \left(\frac{1}{(a)^{1/2}} \right) \left(\frac{1}{(E_{1B})^{1/2}} \right) \tag{32}$$

Thus one decides on the value of K, usually 0.02 to 0.04, determines $(C'_{MS}/(1-K))^{1/2}$, and uses equation 32 to find the new fluxmeter setting as one changes either or both angle and energy.

The choice of K is dependent upon the particular target. One necessary condition in the use of equations 18 and 19 is that the lamina contain only the element of interest or its isotopes, in this case Li^6 and Li^7. Consequently, if one of the contaminants C^{12} or O^{16} has diffused into the target, one must be certain to follow far enough back so that the Li^6 is not diluted. The condition of the front edge of the target may be estimated by looking at the Li^6 profile and the low energy sides of the contaminants. A rounding off of the Li^6 edge and a low energy tail on the contaminants indicates diffusion (see figure 4). The amount of contamination is a function of the residual gas pressure in the target chamber, time, and the amount of charge accumulated at a particular spot on the target.

C. CALIBRATION OF APPARATUS

1. Electrostatic Analyzers

The 80^{o} electrostatic analyzer was calibrated at the beginning and end of the first part of the experiment and the agreement in the values of C_{EA} was found to be about 1/1000. The average value obtained was $C_{EA} = 1.000 \pm 0.1\%$. The method used was to observe the resonant γ's from $F^{19}(p, \alpha\gamma)O^{16}$ at the $E_p = 872.5 \pm 0.4$ kev resonance. (Marion, 1961) One of the curves showing the gamma ray yield, from a target of thickness s, as a function of potentiometer setting is shown in figure 7. The center of this curve E_1 is equal to $E_R + \frac{s}{2}$, so by combining this with the equation

$$E_{1B} = E_1 + \Delta E_1 + ZeV_T \tag{33}$$

where ΔE_1 is the energy loss due to surface contamination and V_T is the target potential with respect to ground, and equation 28, one obtains

$$C_{EA} \simeq \frac{E_R}{ZV_{EA}} \left(1 - \frac{E_R}{2M_0c^2}\right)\left(1 + \frac{b}{E_R}\right) \tag{34}$$

where

$$b = \frac{s}{2} + \Delta E_1 + ZeV_T \tag{35}$$

The first target was CaF_2 evaporated on a copper backing and the thickness s was estimated by weighing the CaF_2, which was to be placed in a tantalum boat, and assuming the mass to be distributed evenly on a hemispherical shell at a known distance. The target was

estimated in this way to be about 2 kev thick to 0.9-Mev protons. The target was made in a bell jar and then immediately placed in the scattering chamber so ΔE_1 due to contaminant surface layers was assumed to be negligible. For electron suppression the target was kept at +300 volts. The second target was made by holding a piece of copper over an HF bottle.

The 90° electrostatic analyzer was calibrated at various times during the high energy part of the experiment, using the $Li^7(p, n)Be^7$ threshold.* Either thin evaporated natural Li or LiF targets on thick backings were used and the neutrons counted by a B^{10} plastic scintillation counter. An integral bias technique was used so that from a $(\text{yield})^{2/3}$ versus potentiometer voltage plot, shown in figure 8, the constant C_{EA} could be obtained by extrapolating to zero yield. The necessary relation is

$$Y^{2/3} = \text{constant}\left[C_{EA} V_{EA}\left(1 + \frac{E_{1B}}{2M_0c^2}\right) - E_{th}\right] \tag{36}$$

Thus at threshold

$$C_{EA} = \frac{E_{th}}{V_{EA}\left(1 + \frac{E_{th}}{2M_0c^2}\right)} \tag{37}$$

The value for E_{th} used was that given by Marion (1961); E_{th} = 1880.7 ± 0.4 kev. The average value of nine determinations made at different times during the course of the experiment was C_{EA} = 2.274 ± 0.1% Mev/volt.

*The author is indebted to R. K. Bardin for the use of his calibration data.

2. Magnetic Analyzers

Both the 10.5-inch and the 16-inch magnetic spectrometers were calibrated by scattering protons from clean copper surfaces. The calibration constant C_{MS} will thus depend upon the electrostatic analyzer constant C_{EA} and can be determined from the equations

$$C_{MS} = \frac{M_0 I^2 E_{20}}{Z^2\left(1 - \frac{E_{20}}{2M_0c^2}\right)} \tag{38}$$

$$E_{20} = \frac{\alpha Z C_{EA} V_{EA}}{1 - \frac{Z C_{EA} V_{EA}}{2M_0c^2}} - \left(\alpha + \frac{\epsilon_2}{\epsilon_1}\right)\Delta E_1 + (1-\alpha) Z e V_T \tag{39}$$

where the fluxmeter setting I now is the value corresponding to half way up the profile.

The variations in C_{MS} were of the order $\pm 0.3\%$; therefore the 16-inch spectrometer was calibrated on every run by scattering protons from copper and that particular C_{MS} was used for that data. The 10.5-inch spectrometer was not calibrated with the use of copper profiles for every run; however, it was possible to calibrate the spectrometer from the C^{12} and O^{16} contamination peaks and, if the contamination appeared to be small, the Li^6 edges were also used. The magnetic spectrometer constant used then was the average of the above values for each particular run.

3. Magnetic Spectrometer Resolution-to-Solid Angle Ratios

A determination of the factor $ZeR/2CV\Omega_L$ must be made before equations 18 or 19 can be used. This was accomplished by using

for N in equation 19 the number of protons scattered by a clean copper surface, corresponding to a definite charge CV collected, and by assuming that the scattering cross section follows the Rutherford formula. The values of the Li^6 cross sections determined in this work, therefore, depend upon this assumption. For the high energy work this determination was made two or three times during each run and the average value used for that particular data. No special attempt was made to keep the trigger voltage of the integrator constant from run to run; however, the same capacitor was used for the copper scattering as for the Li^6 runs. For the low energy work different capacitors were used for the copper scattering and Li^6 runs and the integrator firing voltage was measured once during each run. The low energy work, therefore, depends upon the measured capacitor ratios.

4. Determination of Scattering Angles

For any particular reaction or scattering cross section measurement, one first selects the desired angles in the center of mass system and then converts to the laboratory system by using the equation

$$\cot \theta_L = \frac{x + \cos \theta_{CM}}{\sin \theta_{CM}} \qquad (40)$$

where x is given by equation 26.

For each scattering chamber the horizontal magnet angle θ_H was calibrated by first scanning the incident proton beam with a small aperture at a fixed distance from the center of the chamber to deter-

mine a yield distribution as a function of angle.* Then the magnet aperture was scanned to determine the number of protons scattered, as a function of angle, into it. The difference in the centroids of the two distributions then gives $\pi - \theta_H$. This was done at a backward angle and at an angle near 90° in order that a correction curve might be drawn. The scattering plane for the 6-inch chamber was horizontal, but the geometry of the 2.5-inch chamber, shown in figure 9, was more complicated. The particle beam enters the scattering chamber 10° above the horizontal plane and leaves 10° below it. The equation relating the horizontal magnet angle θ_H to the scattering angle θ_L is

$$\sin \frac{\theta_L}{2} = \cos \alpha \sin \frac{\theta_H}{2} \qquad (41)$$

where here $\alpha \simeq 10^\circ$. A correction to θ_H was found necessary for both scattering chambers and was of the order of $+0.5^\circ$ to $+1^\circ$.

D. TARGET PREPARATION

Since Li forms Li_2O and LiOH very rapidly in air, it is necessary to perform the actual evaporation somewhere in the scattering chamber. The targets must be smooth and they must not deteriorate too quickly under particle bombardment. Freshly evaporated copper on a clean microscope slide was found to be a very satisfactory backing material for the Li targets. The microscope slides provided the smoothness and the copper provided enough thermal conductivity to

*The author is indebted to R. K. Bardin for the angle calibration data on the 6-inch scattering chamber.

prevent deterioration by local heating. The slides were cleaned first with a detergent and distilled water, then placed in chromic acid for a few minutes, rinsed in distilled water, and dried with lint-free gauze. The copper evaporation was performed in a vacuum bell jar and the copper blanks then placed immediately in the scattering chamber. A furnace was situated below each scattering chamber so that with the use of a long target rod, the Li evaporations could be carried out and the targets moved directly up into the scattering chamber.

Two Li^6 metal samples were used, one of 94.5% purity and the other of 99.7% purity. Most of the work was done with the higher purity sample. The Li^6 metal was cleaned under kerosene, then transferred directly to the furnace and the system placed under vacuum. For the low energy work with the 2.5-inch scattering chamber, a long narrow cold trap was used. The furnaces were made from tantalum sheets. However, satisfactory results were not always achieved with this set-up, so for the high energy work, improvements were made. Figure 10 shows a cross section of the 6-inch variable angle scattering chamber. In this set-up the second copper blank may be lowered through the cylindrical cold trap into the furnace area while the upper calibration copper blank is isolated from the Li furnace area by shields. The cylindrical cold trap was designed so that it was as near as possible to the target position for scattering. The better targets obtained with this set-up were possible mainly because of the improved local vacuum. An additional feature of the new set-up was the use of a very pure carbon rod "cannon" type

furnace which was heated by a coil of molybdenum wire. This furnace held the Li well, was very directional, and could be used many times. An indication of the quality of the targets obtained with the two different set-ups is found by comparing the contamination peaks in the profiles of figures 3 and 5. In the earlier work the Li^6 targets were used for one or two days. However, a procedure was finally developed so that the Li^6 targets were not used for a period longer than eight hours.

E. STOPPING POWER MEASUREMENTS

In order to use the thick target equation 18 or 19, one must first know the stopping power ϵ as a function of energy. The values used here were those given in the review article by Whaling (1958). There was, however, some doubt about the values of the Li stopping powers for higher energies. Values deduced from old α-particle data of Rosenblum (1928) were considerably higher than that predicted by the Bloch equation. Consequently, a determination of the relative stopping powers of Li was made over the region 0.8 Mev to 2.9 Mev. The technique used was to scatter protons first from a clean copper target, then from a copper target on which a thin layer of lithium had been evaporated. Figures 1b and 1c indicate the situation from which one obtains experimentally the energy displacement δE_{20} of the copper edge. Figure 11 illustrates the displacement for two different spots on the same copper + lithium target. For a given target spot the relative displacements are found for several energies

and relative stopping powers determined. These values were then normalized to the low energy measurements which are believed to be accurate on an absolute scale.

Referring to figures 1b and 1c, one finds (Warters, 1953)

$$\delta E_{20} = E_{2B} - E_{20} \tag{42}$$

and

$$E_{20} = \alpha(E_{1B} - \Delta E_1) - \Delta E_2 \tag{43}$$

where

$$\alpha = \alpha_{Cu}$$

Thus

$$\alpha\Delta E_1 + \Delta E_2 = \delta E_{20} \tag{44}$$

From the definition of stopping power

$$-\frac{1}{N_s}\frac{\Delta E_1}{s/\cos\theta_1} = \epsilon(\overline{E}_1) \text{ and } -\frac{1}{N_s}\frac{\Delta E_2}{s/\cos\theta_2} = \epsilon(\overline{E}_2) \tag{45}$$

Therefore

$$-\delta E_{20} = \frac{N_s s}{\cos\theta_1}[\alpha\epsilon(\overline{E}_1) + \beta\epsilon(\overline{E}_2)] \tag{46}$$

where

$$\beta = \frac{\cos\theta_1}{\cos\theta_2} \tag{47}$$

If now $\epsilon(\overline{E}_1)$ and $\epsilon(\overline{E}_2)$ are expanded in Taylor series about some energy E_x, one may write

$$-\delta E_{20} = \frac{N_s s}{\cos\theta_1}\left[(\alpha+\beta)\epsilon(E_x) + \{\alpha(\overline{E}_1 - E_x) + \beta(\overline{E}_2 - E_x)\}\frac{\partial\epsilon}{\partial E}\Big|_{E=E_x} + \ldots\right] \tag{48}$$

where $\overline{E}_1 - E_x$ and $\overline{E}_2 - E_x$ are assumed small. Setting the coefficient of the $\frac{\partial \epsilon}{\partial E}$ term equal to zero gives

$$E_x = \frac{\alpha \overline{E}_1 + \beta \overline{E}_2}{\alpha + \beta} \tag{49}$$

Now $\overline{E}_1$ and $\overline{E}_2$ may be written as

$$\overline{E}_1 \simeq E_{1B} - \frac{\Delta E_1}{2} \tag{50}$$

and

$$\overline{E}_2 \simeq E_{20} + \frac{\Delta E_2}{2} \tag{51}$$

So E_x becomes

$$E_x = \frac{\alpha E_{1B} + \beta E_{20}}{\alpha + \beta} + \frac{\beta \Delta E_2 - \alpha \Delta E_1}{2(\alpha + \beta)} \tag{52}$$

With the use of equation 44 and recalling $E_{2B} = \alpha E_{1B}$, this may be written as

$$E_x = \frac{E_{2B} + \beta E_{20}}{\alpha + \beta} + \frac{\delta E_{20}}{2(\alpha+\beta)} \left[\frac{\beta(\frac{\Delta E_2}{\Delta E_1}) - \alpha}{(\frac{\Delta E_2}{\Delta E_1}) + \alpha} \right] \tag{53}$$

Equation 48 becomes

$$\epsilon(E_x) = - \frac{\cos \theta_1}{N_s s} \frac{\delta E_{20}}{\alpha + \beta} \tag{54}$$

The above two equations then are used to compute the relative stopping powers. In order to estimate the correction term in equation 53, one may use

$$\frac{\Delta E_2}{\Delta E_1} \simeq \beta \frac{\epsilon(E_{20})}{\epsilon(E_{1B})} \tag{55}$$

and the theoretical Bloch equation (see Whaling, 1958)

$$\epsilon(E) = \frac{aZ_1^2 Z_2}{E}\left[\ln \frac{E}{Z_2} + b\right] \tag{56}$$

For two different energies and the same target spot and geometry, equation 54 gives

$$\epsilon(E_x') = \frac{\delta E_{20}'}{\delta E_{20}}\ \epsilon(E_x) \tag{57}$$

The results of this determination are given in figure 12 and show that experimentally the stopping power for Li does follow the Bloch curve at higher energy. This curve was then used in the reduction of the $Li^6(p, p)Li^6$ data.

F. CORRECTIONS TO YIELDS

There are three corrections which must be made in this experiment in order to obtain the yield N to be used in equations 18 or 19. The first of these is a background subtraction. For this experiment the major background consisted either of protons scattered from the Li^7 contamination in the target or of α^{++}s and He^{3++}s from the reaction $Li^6(p, \alpha)He^3$. The Li^7 thick target profile, shown in figure 4, was only present when the lower purity Li^6 sample was used. The nature of the background at more forward angles may be determined from the profile in figure 6. The curve through the dots is the unrestricted profile. The crosses indicate the profile obtained when an 0.5 mil Al foil is placed at the end of the magnet. The α^{++}s and He^{3++}s are stopped while the protons are energetic enough to

pass through the foil. The circles show the profile obtained 24 hours later.

A second correction to be made is the loss due to high counting rate. Assume that the scintillation counter, consisting of CsI crystal, photo-multiplier, pre-amplifier, amplifier, and scalar, is dead for a time ρ seconds after each recorded event. If the observed counting rate is n_R, then the fraction of a second during which the apparatus is dead is $n_R\rho$. The fraction of time during which the apparatus is sensitive is $1 - n_R\rho$. This is then the fraction of the true number of events N_R. Thus

$$\frac{n_R}{N_R} = 1 - n_R\rho \tag{58}$$

or

$$N_R = \frac{n_R}{1 - n_R\rho} \tag{59}$$

The dead time ρ of the scintillation counter was obtained by scattering protons from copper. If, for a definite charge CV collected, one increases the counting rate n_R, the time t required for the collection decreases. The difference Δ_i in the number of counts recorded n_i and the true number of counts N is

$$\Delta_i = N - n_i = (N_R - n_{R_i})t_i = \frac{n_{R_i}^2 t_i \rho}{1 - n_{R_i}\rho} \tag{60}$$

or

$$\Delta_i = \frac{n_i^2 \rho}{t_i\left(1 - \frac{n_i \rho}{t_i}\right)}$$

An estimate of the true number of counts is made by counting at a very low counting rate. The counting rate is then increased and the time t_i recorded. The differences Δ_i in the number of counts recorded n_i and the above estimate for N is then plotted against $1/t_i$. This is shown in figure 13. From equation 60 one can see that at low counting rates Δ may be approximated by a straight line with a slope equal to $n_i^2\rho$. With the use of the equation

$$\rho \simeq \frac{\text{slope}}{N^2} \tag{61}$$

the dead time ρ was found to be about 10 μsec. This correction was found necessary for the copper calibrations and the forward angle Li^6 yields.

A third consideration is that of charge exchange. Some of the protons, α-particles or He^3-particles, which scatter or are produced within the target, will pick up electrons on the way out and thus will not be observed in the magnetic spectrometer as protons or α's or He^3's. Allison (1958) has measured the probability of this happening as a function of energy and gives data for various solids. In the present experiment corrections for this effect were less than one per cent for proton scattering but were slightly larger for the $Li^6(p, \alpha)He^3$ reaction.

There are two other important factors to be considered which may affect the yield. As the experiment is being performed one must check the operation of the scalar and the current leakage of the integrator.

The screening effect of the electrons on the scattering cross

section was estimated by the Born approximation (Bohm, 1951) for the $Li^6 + p$ scattering and by a classical approximation (Wenzel, 1952) for the Cu + p scattering and found to be less than 0.3% in both cases. Therefore a correction was not made for this effect.

G. EXPERIMENTAL RESULTS

1. Excitation Curves

The cross section for the elastic scattering of protons from Li^6 nuclei was measured from about 0.45 Mev to 2.9 Mev at intervals of 12.5 or 20 kev for c.m. angles near the zeros of the first and second Legendre polynomials and near the farthest back angle obtainable ($\sim 160^\circ$). The results are shown in figure 14 and indicate that the scattering is Rutherford near 0.4 Mev and that $\sigma_{scattering}/\sigma_{Rutherford}$ rises gradually up to about 1.1 Mev where it then exhibits resonant behavior up to about 3 Mev. The decrease in cross section from the backward angle to 90° suggests that the resonance might be formed by odd ℓ-wave protons. The cross section measured at 90° will then be the most informative, since the interference terms will vanish; this is shown in figure 15. A comparison of the 160° data ($\theta_L \sim 156^\circ$) with that of Bashkin and Richards (1951) at $\theta_L \sim 164^\circ$ indicates that their cross sections are about 2/3 of the values measured in the present experiment.

No indication was found of a large anomaly in the vicinity of 1 Mev.

2. Angular Distributions

The scattering cross section was also measured at c.m. angles near 140°, 110°, and 70° at intervals of 100 kev. Figures 16 through 40 show the 25 angular distributions obtained. The error bars indicate relative errors and are 3% for the backward angles and 4% for the more forward angles 90° and 70°. The scattering cross sections determined are given in Table 1.

3. The $Li^6(p,\alpha)He^3$ Reaction

In order to analyze the scattering data it is necessary to know the reaction cross section. Since the reported values (Marion, 1956; Bashkin, 1951; Ajzenberg-Selove, 1959) for this reaction varied by at least a factor of 3, a new determination was deemed necessary. The thick target method was used and the angle of the spectrometer set at $\theta_L = 95^{\circ}45'$ to detect the He^3's coming off in the backward hemisphere which correspond to the α's in the forward direction which Marion (1956) measured at $\theta_L = 60^{\circ}$. The thick target profile obtained for an incident proton energy of 2.3 Mev is shown in figure 41. Since pulse height analysis was not used, the resulting curve is the superposition of the α profile and the He^3 profile. The two profiles may be separated with the use of the thick target equation 18. The positions at which the halfway points of the front edges of the profiles should appear are indicated by the lower arrows. The spread in fluxmeter current ΔI in which the profiles should rise was estimated from the equation

$$\Delta I = \frac{1}{2}\left(\frac{\Delta E_{20}}{E_{20}}\right) I_{1/2} \qquad (62)$$

where $\Delta E_{20}/E_{20}$ was calculated from (Cohen, 1949)

$$\left(\frac{\Delta E_{20}}{E_{20}}\right)^2 = \left(\frac{1}{R}\right)^2 + \left(\frac{1}{E_{20}}\frac{\partial E_{20}\Delta\theta}{\partial\theta}\right)^2 \qquad (63)$$

Here

$$R = \frac{p}{\Delta p} = 2(1 + M)\frac{r}{\Delta r} \qquad (64)$$

the momentum resolution of the magnet, and may be obtained from either this equation and the measured values of central path radius r, exit slit width Δr and magnification M, or from the measured resolution-to-solid angle ratios if the solid angles are known. A value for $\Delta\theta$ was obtained from the measurements on scattering angle and $\frac{1}{E_{20}}\frac{\partial E_{20}}{\partial\theta}$ was determined from the kinematical equation (Brown, 1951)

$$\frac{1}{E_{20}}\frac{\partial E_{20}}{\partial\theta} = -\frac{1}{E_{20}}\frac{2(M_1M_2E_{1B}E_{20})^{1/2}\sin\theta}{M_2+M_3-\left(\frac{M_1M_2E_{1B}}{E_{20}}\right)^{1/2}\cos\theta} \qquad (65)$$

For $\theta_L = 95^o45'$ the calculated spreads ΔI were determined mainly by the $\partial E_{20}/\partial\theta$ term and are indicated by the bars at the bottom of the graph.

From figure 41 one can see that the yield of the top of the He^3 profile should contain only He^{3++} particles; therefore, this yield was used to calculate the cross section for the reaction $Li^6(p, He^3)He^4$ at $\theta_L = 95^o45'$, which should then be the same as the cross section for the reaction $Li^6(p, \alpha)He^3$ at $\theta_L = 60^o$. When

this was done it was found that the cross section was about 50% of the value stated by Marion (1956) but in agreement with the results of Burcham and Freeman (1950). By assuming the relative cross sections of Marion et al. to be correct and normalizing to the above value, one can then use equations 18 and 22 to predict the yield of He^{3++}'s at some depth within the target. This was done and a line drawn through this point and the yield at the front of the He^3 profile. The α profile shown in figure 41 was then found by subtracting the He^3 profile from the total profile. The cross section for $Li^6(p, \alpha)He^3$ was then computed from the α profile yield and was found to be about 60% of the value quoted by Marion et al. Estimates of the reaction cross section made at other angles and energies from the He^3 profiles also indicated differences of about the same amount. Therefore, the $Li^6(p, \alpha)He^3$ reaction cross sections of Marion et al. were assumed to be correct on a relative scale, and were normalized to 55% of the values quoted. The integrated reaction cross section for $Li^6(p, \alpha)He^3$ is shown in figure 42. These normalized values were then used in the analysis of the scattering data. A later reexamination of the work of Marion et al. turned up a factor of 1/2 so that their measurements are now in agreement with those of Burcham and Freeman (1950) and the present determination.

4. Probable Error

The uncertainties of the relative stopping cross sections were mostly a result of the uncertainty in locating the mid-points of the copper profiles. The relative energy losses in the lithium layers

were found from the difference of two measured quantities. Hence the % uncertainty depends upon the magnitude of this difference, i. e., on the thickness of the layer. The uncertainties were found to vary from 2 to 7 % and are shown on the stopping cross section diagram. Since the measured curve for the stopping cross section agreed with the Bloch formula, it was assumed that the stopping cross sections used in the determination of the scattering cross sections could be determined relatively from the Bloch curve to within an uncertainty of 2%. The absolute uncertainty for the stopping cross sections of protons on lithium and protons on copper was assumed to be 3%, the value given by Bader, et al. (Bader, 1956).

The uncertainties in the measured Li^6 scattering cross sections were estimated to be about 3% relative error for all angles. The absolute error was estimated to be about 5%. The sources of these uncertainties and their respective contributions are shown in table 2, and were combined as independent errors to give the values stated above. These uncertainties may also be taken as reasonable estimates for the probable error in the ratio, $\sigma_{scattering}/\sigma_{Rutherford}$, since the coherent errors make only a small contribution to the combined error.

III. THEORETICAL ANALYSIS OF THE DATA

A. DISCUSSION OF THE THEORETICAL EQUATION

From the basic concepts of non-relativistic quantum mechanics one can derive the cross section for the elastic scattering of charged particles with spin i from charged nuclei with spin I in terms of a scattering matrix $S^{J}_{a,\, s'\ell';\, as\ell}$ which relates the amplitudes of the outgoing waves to those of the incoming waves. The reaction cross section is also found in the same manner. The concept of channel spin $\vec{s}$ is introduced such that

$$\vec{s} = \vec{I} + \vec{i}$$

$$s = |I - i|, \ldots, I + i \tag{66}$$

A given set of two particles is denoted by the index a and is referred to as a channel. For relative orbital angular momentum $\vec{\ell}$ a compound nuclear state may have a total spin $\vec{J}$ such that

$$\vec{J} = \vec{s} + \vec{\ell}$$

$$J = |s - \ell|, \ldots, s + \ell \tag{67}$$

For each possible state of given J one may associate amplitudes for various modes of formation and decay. These amplitudes are complex and may be related to a resonant description of the state. The object of the analysis is to deduce the various parameters of the resonant formulation. The technique of analysis of elastic scattering data used is that described by Christy (1956) and Mozer (1956) and involves the

display of the amplitude matrix $[A_{\alpha a,\, s's,\, \nu'\nu}]$. Here the index ν designates the magnetic substates of the channel spin s and the primes indicate the outgoing channel. An element of the amplitude matrix is given by

$$A_{\alpha a,\, s's,\, \nu'\nu} = \sqrt{R}\, e^{i\xi}\delta_{s's}\delta_{\nu'\nu} + \frac{i\sqrt{\pi}}{k_a}\sum (2\ell+1)^{1/2} e^{i(\eta_\ell + \eta_{\ell'} - 2\eta_0)}$$

$$\times\, (\ell\, s\, o\, \nu/JM)(\ell' s' m_{\ell'}, \nu'/JM) f^J_{ss'\ell\ell'} Y^{m_{\ell'}}_{\ell'} \qquad (68)$$

where

$$f^J_{ss'\ell\ell'} = S^J_{\alpha s'\ell';\alpha s\ell} - \delta_{s's}\delta_{\ell'\ell} \qquad (69)$$

The first term is the amplitude for Rutherford scattering with

$$R = \left(\frac{n}{2k_a \sin^2\frac{\theta}{2}}\right)^2 \quad \text{(Rutherford cross section)} \qquad (70)$$

$$\xi = -n \ln \sin^2\frac{\theta}{2} \quad \text{(Rutherford phase shift)} \qquad (71)$$

$$n = \frac{Z_1 Z_0 e^2}{\hbar v_a} \qquad (72)$$

where $v_a = \hbar k_a/\mu$ is the relative velocity, μ the reduced mass and θ the center of mass angle.

$$\eta_\ell - \eta_0 = \sum_{j=1}^{\ell} \tan^{-1}\frac{n}{j} \quad \text{(Coulomb phase shift)} \qquad (73)$$

The second term is the nuclear part and consists principly of a Clebsch Gordan coefficient for formation of the state $(\ell\, s\, o\, \nu/JM)$ and one for decay of the state $(\ell' s' m_{\ell'}, \nu'/JM)$, the spherical harmonic $Y^{m_{\ell'}}_{\ell'}$ of the exit channel, and the nuclear amplitude $f^J_{ss'\ell\ell'}$ for formation and decay of a nuclear state of definite spin J. The sum

in equation 68 is

$$\sum = \sum_{J=0}^{\infty} \sum_{\ell=|J-s|}^{J+s} \sum_{\ell'=|J-s'|}^{J+s'} \tag{74}$$

where one should keep in mind that for an incoming beam along the z axis $m_\ell = 0$ so that $M = \nu = m_{\ell'} + \nu'$.

The differential cross section for scattering from magnetic sub-state ν of entrance channel spin s to magnetic sub-state ν' of exit channel spin s' is found by squaring the appropriate element of the amplitude matrix.

$$d\sigma_{\alpha s'\nu', \alpha s\nu} = |A_{\alpha\alpha, s's, \nu'\nu}|^2 \tag{75}$$

The differential cross section for scattering from channel spin s to s' for an unpolarized beam, is found by averaging over the magnetic sub-states of s and summing over those of s'.

$$d\sigma_{\alpha s', \alpha s} = \frac{1}{2s+1} \sum_{\nu=-s}^{s} \sum_{\nu'=-s'}^{s'} d\sigma_{\alpha s'\nu', \alpha s\nu} \tag{76}$$

If in addition the particle detectors are spin insensitive, one must average over initial channel spins and sum over final channel spins.

$$d\sigma_{\alpha,\alpha} = \sum_{s=|I-i|}^{I+i} \sum_{s'=|I'-i'|}^{I'+i'} \frac{2s+1}{(2I+1)(2i+1)} d\sigma_{\alpha s', \alpha s} \tag{77}$$

The final equation for the elastic scattering cross section is then

$$d\sigma_{\alpha,\alpha} = \frac{1}{(2I+1)(2i+1)} \sum_{s=|I-i|}^{I+i} \sum_{s'=|I'-i'|}^{I'+i'} \sum_{\nu=-s}^{s} \sum_{\nu'=-s'}^{s'} |A_{\alpha\alpha, s's, \nu'\nu}|^2 \tag{78}$$

For a particular incident particle and target nucleus the amplitude matrix elements are worked out for the lowest orbital angular momentum waves which are thought to contribute to the scattering. The amplitude matrix for the case of $Li^6(p, p)Li^6$ with only s- and p-waves contributing is shown in figure 43. The scattering amplitudes within each element or box are coherent and give rise to cross product or interference terms when the matrix element is squared. The final cross section is then found by squaring each box, adding them and dividing by $(2I + 1)(2i + 1)$.

The elements of the scattering matrix $S^J_{as'\ell' t;as\ell}$ are complex quantities and are related to a resonant description by the relation (see Mozer's thesis (Mozer, 1956) for a more complete discussion).

$$S = f + ig = e^{2i\phi}[1 + \frac{\Gamma_p}{\Gamma}(e^{2i\delta} - 1)] \tag{79}$$

where

$$\delta = \cot^{-1}\frac{E_R - E}{\Gamma/2} \qquad \text{(resonant phase shift)} \tag{80}$$

ϕ is the "potential phase shift" which for the case of a charged hard sphere would be

$$\phi = -\tan^{-1}\frac{F_\ell(ka)}{G_\ell(ka)} \tag{81}$$

where a is the "interaction radius." The latter quantity is not well defined but is sometimes given by

$$a = R_0(A_1^{1/3} + A_0^{1/3}) \tag{82}$$

with

$$R_0 = 1.45 \times 10^{-13} \text{ cm}$$

$F_\ell(ka)$ and $G_\ell(ka)$ are the coulomb wave functions evaluated at the interaction radius a and wave number k.

In general, however, ϕ will also contain the "tails" of other states at energies far from the region being considered. The relation 79 enables us to separate a rapidly varying energy-dependent behavior in the scattering from the slowly-varying non-resonant scattering.

The resonant parameters of a state are

the resonant energy E_R

the total width Γ

the proton width Γ_p

other partial widths Γ_α, Γ_γ, Γ_n, ...

The partial widths are a measure of the probability of the state decaying via a certain mode and thus the partial widths must add up to the total width for decay of the state.

$$\Gamma = \Gamma_p + \Gamma_\alpha + \Gamma_\gamma + \Gamma_n + \ldots \tag{83}$$

For a given mode of decay the nuclear part of the probability for decay may be separated out by defining the "reduced" width.

$$\Gamma_{i\ell} = 2k_i P_\ell \gamma_{i\ell}^2 \tag{84}$$

where i denotes a particular channel and ℓ denotes the angular momentum wave involved. k_i is the relative wave vector for the channel i.

$$k_i = \frac{2\pi}{\lambda_i} = \frac{2\pi p_i}{h} = \frac{\mu_i v_i}{\hbar} \tag{85}$$

where v_i is the relative velocity of the two particles involved, and

$$\mu_i = \frac{M_1 M_0}{M_1 + M_0} \quad \text{the "reduced mass" for channel i} \tag{86}$$

P_ℓ is the penetration factor and depends upon the relative wave factor, the angular momentum involved, and the interaction radius.

$$P_\ell(k_i a_i) = \frac{1}{F_\ell^2(k_i a_i) + G_\ell^2(k_i a_i)} \tag{87}$$

where F_ℓ is the regular Coulomb wave function, and G_ℓ is the irregular Coulomb wave function. For a very broad state the level shift of the state (Thomas, 1951) must be considered. The resonant energy is equal to the actual energy of the state (in the CM system) plus a level shift in energy.

$$E_{R_\lambda} = E_\lambda + \Delta_\lambda \tag{88}$$

where the index λ denotes the state.

The level shift is given by

$$\Delta_{i\ell} = -\frac{\gamma_{i\ell}^2}{a_i}\left[\ell + \frac{d(\ln A_\ell)}{d(\ln k_i a_i)}\right] \tag{89}$$

The quantity A_ℓ is just

$$A_\ell(k_i a_i) = \left[F_\ell^2(k_i a_i) + G_\ell^2(k_i a_i)\right]^{1/2} \tag{90}$$

The total level shift then is the sum of those for each mode of decay.

$$\Delta_\lambda = \sum_{i\ell} \Delta_{i\ell} \tag{91}$$

The partial width of decay is given by

$$\Gamma_i = \sum_{\ell} 2k_i P_\ell \gamma_{i\ell}^2 \qquad (92)$$

From equations 79 and 81 one sees that since ϕ is negative for "potential" type scattering; the complex points describing the scattering matrix element begin at $(1, 0)$ and move in a clockwise direction on the unit circle as the relative energy of the incoming channel increases.

From equations 79 and 80, however, one sees that the complex points describing the resonant scattering move in a counter-clockwise direction (δ's are positive) and the distance of the points to the point $(1, 0)$ depends upon the value of Γ_p/Γ. When $E = E_R$, i.e., at resonance, δ becomes $\pi/2$ and thus for pure resonant scattering the complex points describing the resonant scattering should cross the real axis at $1 - 2(\Gamma_p/\Gamma)$.

If Γ_p/Γ is close to unity and the potential scattering small, then the resonant complex point should be near the point $(-1, 0)$. If Γ_p/Γ is small then it will be in the vicinity of the point $(1, 0)$ and will depend mainly on the potential phase shift.

B. APPLICATION TO $Li^6(p, p)Li^6$

For this case one must combine a proton of spin and parity $1/2^+$ to a Li^6 nucleus of spin and parity 1^+. Thus there are two possible channel spins, $1/2^+$ and $3/2^+$. If one considers only s-waves, then nuclear states in Be^7 may be formed which have total spins and parities of $J^\pi = 1/2^+$ or $3/2^+$. The spin and parity associated with p-waves is 1^-. Thus nuclear states may be formed through the $1/2$ spin

channel which have $J^{\pi} = 1/2^-$ and $3/2^-$. States which may be formed through the $3/2$ spin channel have $J^{\pi} = 1/2^-$, $3/2^-$ and $5/2^-$. The above possibilities then must be considered in constructing the amplitude matrix shown in figure 43.

The experimental data indicates the presence of a strong resonance in the vicinity of 1.85 Mev. The angular distributions show a decrease in cross section from backward angles to $\theta_{CM} = 90^{\circ}$. If only s- and p-waves are assumed to be important in this energy region then this nuclear resonance would have to be formed by p-waves.* The spin and parity of this state then must be either $1/2^-$, $3/2^-$ or $5/2^-$. The assumption will be made that there is only one p-wave nuclear resonance in the region investigated.

The mirror nuclei Li^7 and Be^7 shown in figure 44 have corresponding levels for the first and second excited states. There is also a well-defined state at 7.47 Mev in Li^7 which should correspond to the resonance seen in Be^7 at 7.18 Mev. From the total absorption cross section for neutrons on Li^6 and the cross section for the reaction $Li^6(n,\alpha)H^3$, the spin of the above state in Li^7 was found to be $5/2^-$ (Johnson, 1954). It was not possible because of the divergent cross section at forward angles and the unknown s-wave background, to perform a similar analysis in the case of $Li^6(p, p)Li^6$ and $Li^6(p, \alpha)He^3$. However, it seemed reasonable to assume that the state in Be^7 at 7.18 Mev is the mirror state of the $5/2^-$ state in Li^7; therefore, an analysis was performed for the $Li^6(p, p)Li^6$ scattering under the assumption that only s- and p-waves contribute and that the p-wave

*The reduced proton width calculated by assuming f-wave exceeds the single particle limit.

scattering is only through a $5/2^-$ resonant state. The amplitude matrix for this case is shown in figure 45 and is of course much simpler than that for the more general situation of s- and p-waves. The differential cross section for scattering is found by squaring each box, adding them together and dividing by six. There are three unknown complex amplitudes which describe the scattering, one for the resonant p-wave state and two for the s-wave scattering, one for each spin channel. The real and imaginary parts of these complex amplitudes are written as follows:

$$
\begin{aligned}
f^{\frac{1}{2}}_{\frac{1}{2}\,\frac{1}{2}\,s\,s} &= f_{\frac{1}{2}} + i g_{\frac{1}{2}} - 1 \\
f^{\frac{3}{2}}_{\frac{3}{2}\,\frac{3}{2}\,s\,s} &= f_{\frac{3}{2}} + i g_{\frac{3}{2}} - 1 \\
f^{\frac{5}{2}}_{\frac{3}{2}\,\frac{3}{2}\,p\,p} &= f_{\frac{5}{2}} + i g_{\frac{5}{2}} - 1
\end{aligned}
\tag{93}
$$

It is also convenient to define the quantities X, Y and U in terms of the above amplitudes.

$$
X = \frac{1}{3} f_{\frac{1}{2}} + \frac{2}{3} f_{\frac{3}{2}}
\tag{94}
$$

$$
Y = \frac{1}{3} g_{\frac{1}{2}} + \frac{2}{3} g_{\frac{3}{2}}
$$

$$
U = 1 - \frac{1}{3}\left(f^2_{\frac{1}{2}} + g^2_{\frac{1}{2}}\right) - \frac{2}{3}\left(f^2_{\frac{3}{2}} + g^2_{\frac{3}{2}}\right)
\tag{95}
$$

It is also to be noted that

$$U = \frac{k^2 \sigma_R(\text{s-wave})}{\pi} \tag{96}$$

where σ_R is the integrated s-wave reaction cross section. The differential cross section for scattering may then be written in the following way:

$$\begin{aligned}\frac{d\sigma}{d\Omega}(\theta, E) = R + \left(\frac{\sqrt{R}}{k}\sin\xi - \frac{1}{2k^2}\right)(X-1) - \frac{\sqrt{R}}{k}\cos\xi\, Y - \frac{U}{4k^2} \\ + \frac{1}{2k^2}\left\{\left(f_{\frac{3}{2}} - 1\right)\left[\left(f_{\frac{5}{2}} - 1\right)\cos 2(\eta_1-\eta_0) - g_{\frac{5}{2}}\sin 2(\eta_1-\eta_0)\right]\right. \\ \left. + g_{\frac{3}{2}}\left[\left(f_{\frac{5}{2}} - 1\right)\sin 2(\eta_1-\eta_0) + g_{\frac{5}{2}}\cos 2(\eta_1-\eta_0)\right]\right\}\cos\theta \\ - \frac{\sqrt{R}}{k}\left\{\left(f_{\frac{5}{2}} - 1\right)\sin\left[2(\eta_1-\eta_0)-\xi\right] + g_{\frac{5}{2}}\cos\left[2(\eta_1-\eta_0)-\xi\right]\right\}\cos\theta \\ + \frac{9}{50\,k^2}\left(1 + \frac{7}{6}\cos^2\theta\right)\left[\left(f_{\frac{5}{2}} - 1\right)^2 + g_{\frac{5}{2}}^2\right]\end{aligned} \tag{97}$$

The first line is the s-wave scattering in the form given by Christy (1956). The second line is the s-wave, p-wave interference term. The third line is the p-wave, Rutherford interference term, and the fourth line is the resonant contribution to the $5/2^-$ p-wave state.

The object of the analysis is to find a set of six coefficients, $f_{1/2}$, $g_{1/2}$, $f_{3/2}$, $g_{3/2}$, $f_{5/2}$, $g_{5/2}$, as functions of energy which describe the 25 angular distributions over the energy region considered. These coefficients must, however, also be consistent with

the reaction data for $Li^6(p, \alpha)He^3$ and they must vary smoothly as a function of energy.

C. TECHNIQUE OF ANALYSIS OF DATA AND RESULTS

An extension of the method given by Christy (1956) was used to determine a set of the six coefficients at each energy. Equation 97 may be written in terms of X and Y as a straight line. The energy will now be considered fixed and only the angle θ will be varied.

$$Y = A(\theta)X + C(\theta) \tag{98}$$

where the slope is given by

$$A(\theta) = \frac{\sin \xi - \frac{1}{2k\sqrt{R}}}{\cos \xi} \tag{99}$$

and is only a function of kinematical variables and the atomic numbers Z_1 and Z_0. Recall that ξ and R are functions of angle.

The intercept $C(\theta)$ may be written as the sum of two parts.

$$C(\theta) = B(\theta) + D(\theta) \tag{100}$$

where

$$B(\theta) = \frac{[k\sqrt{R} - \sin \xi + \frac{1}{k\sqrt{R}} \{ \frac{1}{2} - k^2(\frac{\sigma_R}{4\pi} + \frac{d\sigma(\theta)}{d\Omega})\}]}{\cos \xi} \tag{101}$$

is the s-wave intercept. This term involves the measured scattering differential cross section $d\sigma(\theta)/d\Omega$ and the integrated s-wave reaction cross section σ_R (s-wave).

The intercept $D(\theta)$ contains the contribution of the p-wave

resonant scattering, p-wave, Rutherford interference scattering and s-wave, p-wave interference scattering. Since the $5/2^-$ p-wave state is formed only through the $3/2$ spin channel, the s-wave, p-wave interference term contains only the s-wave $3/2$ spin channel amplitude. The intercept $D(\theta)$ may then be written as follows:

$$D(\theta) = ZG(\theta) + H(\theta) \tag{102}$$

where

$$Z = (f_{\frac{3}{2}} - 1)S + g_{\frac{3}{2}} \tag{103}$$

is not a function of angle but only a function of energy. The quantities S, $G(\theta)$ and $H(\theta)$ are given by

$$S = \frac{(f_{\frac{5}{2}} - 1)\cos 2(\eta_1 - \eta_0) - g_{\frac{5}{2}} \sin 2(\eta_1 - \eta_0)}{(f_{\frac{5}{2}} - 1)\sin 2(\eta_1 - \eta_0) + g_{\frac{5}{2}} \cos 2(\eta_1 - \eta_0)} \tag{104}$$

$$G(\theta) = \frac{1}{2k\sqrt{R}} [(f_{\frac{5}{2}} - 1)\sin 2(\eta_1 - \eta_0) + g_{\frac{5}{2}} \cos 2(\eta_1 - \eta_0)] \frac{\cos \theta}{\cos \xi} \tag{105}$$

$$H(\theta) = -\{(f_{\frac{5}{2}} - 1)\sin[2(\eta_1 - \eta_0) - \xi] + g_{\frac{5}{2}} \cos[2(\eta_1 - \eta_0) - \xi]\} \frac{\cos \theta}{\cos \xi}$$
$$+ \frac{9}{50k\sqrt{R}} \frac{(1 + \frac{7}{6}\cos^2\theta)}{\cos \xi} [(f_{\frac{5}{2}} - 1)^2 + g_{\frac{5}{2}}^2] \tag{106}$$

In this experiment angular distributions were taken at six different angles, hence six straight line equations may be written in terms of X and Y. The complex scattering amplitudes are restricted by the

conservation of particles to lie within the unit circle in the complex plane. This then results in restrictions on X, Y, and U. These are

$$\begin{aligned} &-1 \leq X \leq 1 \\ &-1 \leq Y \leq 1 \\ &0 \leq U \leq 1 \\ &X^2 + Y^2 \leq 1 - U \end{aligned} \tag{107}$$

The slopes $A(\theta)$ of the six lines are calculated and the s-wave intercepts $B(\theta)$ are computed. If the scattering is describable in terms of s-wave protons alone, then the six lines must intersect within experimental error at some point in the complex plane, which is just the point (X, Y) for this energy. At low energies the six lines do intersect as shown in figure 46. The s-wave intercepts $B(\theta)$ were computed for each of the twenty-five energies and the six lines for X, Y plotted in the complex plane. At higher energies the six lines no longer intersect within experimental error, indicating that s-waves alone are not sufficient to describe the scattering. The plot of the six straight lines with s-wave intercepts at an energy near the peak of the assumed $5/2^-$ p-wave resonance is shown in figure 47.

The next step was to assume reasonable parameters for the p-wave amplitude $f_{5/2} + ig_{5/2}$ and calculate p-wave intercepts $D(\theta)$ for the six angles. The resonant description given by equation 70 was assumed for the p-wave amplitude for a state with $J^\pi = 5/2^-$. The p-wave potential scattering was neglected in the analysis since no good estimate of its contribution could be made. The resonant phase

shift certainly dominates over most of the resonant region. With this assumption the parameters $f_{5/2}$ and $g_{5/2}$ become:

$$f_{\frac{5}{2}} - 1 = \frac{\Gamma_p}{\Gamma} (\cos 2\delta_{\frac{5}{2}} - 1)$$
$$g_{\frac{5}{2}} = \frac{\Gamma_p}{\Gamma} \sin 2\delta_{\frac{5}{2}} \tag{108}$$

with

$$\cot \delta_{\frac{5}{2}} = \frac{E_R - E}{\Gamma/2} \tag{109}$$

A reasonable choice must be made for the resonant parameters Γ_p, Γ, and E_R as a function of energy. From the $Li^6(p, \alpha)He^3$ integrated reaction cross section (figure 42), one may find values for the reduced proton width γ_p^2 and the reduced alpha width γ_α^2. The p-wave reaction cross section is given by

$$\sigma_R(\text{p-wave}) = \frac{\pi}{k^2} \frac{\Gamma_p \Gamma_\alpha}{(E_R - E)^2 + \frac{\Gamma^2}{4}} \tag{110}$$

and becomes at resonance

$$\sigma(E_R) = \frac{4\pi}{k^2} \frac{\Gamma_p \Gamma_\alpha}{\Gamma^2} \tag{111}$$

This combined with the relation

$$\Gamma = \Gamma_p + \Gamma_\alpha$$

yields two sets of values for Γ_p and Γ_α for an assumed s-wave reaction background, one set with large Γ_p and small Γ_α, the other

with small Γ_p and large Γ_α. The magnitude of the resonance in the scattering data indicates that Γ_p is large. These two modes are the dominant modes of decay for the state.

The relative wave vectors for the p-Li^6 system and the α-He^3 system are given in terms of the incident proton energy E_1 in the laboratory system as

$$k_p^2 = 3.536E_1 \times 10^{24} \text{ cm}^{-2}$$
$$k_\alpha^2 = 7.027[E_1 + 4.692] \times 10^{24} \text{ cm}^{-2} \tag{113}$$

The parameters n defined in equation 72 must also be known in order to compute the penetration factors. These are given by

$$n_p^2 = \frac{0.2248}{E_1}$$
$$n_\alpha^2 = \frac{0.7937}{E_1 + 4.692} \tag{114}$$

In all of the above expressions the laboratory proton energy E_1 must be expressed in Mev.

Since the angular momentum quantum number of the incoming proton with respect to the Li^6 nucleus was assumed to be $\ell = 1$, the penetration factor for the entrance channel is given by equation 87 with $\ell = 1$ and k_p as given above. The interaction radius a_p for the p-Li^6 system was taken from equation 82 which gives $a_p = 4.08 \times 10^{-13}$ cm. The penetration factors were found from the graphs given by Sharp, et al. (Sharp, 1955).

The relative orbital angular momentum of the α-He^3 system

which results from the breakup of the Be^7 nucleus in a resonant $J^{\pi} = 5/2^-$ state is found from the conservation of angular momentum and conservation of parity. Since the α-particle has spin and parity 0^+ and the He^3 spin and parity $1/2^+$, the only possible exit channel spin quantum number and parity is $s' = 1/2^+$. Thus from equation 67 the lowest possible relative orbital angular momentum quantum number with negative parity in the exit channel is $\ell' = 3^-$. The penetration factor is then given by equation 87 with $\ell' = 3$ and k_α as given above. The interaction radius was taken from equation 82 which gives $a_\alpha = 4.39 \times 10^{-13}$ cm.

The reduced proton width γ_p^2 and reduced α-width γ_α^2 were found from equation 84, which are in this case

$$\Gamma_p = 2k_p P_1 \gamma_p^2 \quad \text{and} \quad \Gamma_\alpha = 2k_\alpha P_3 \gamma_\alpha^2 \tag{115}$$

Since the magnitude of the s-wave background is not known apriori, various choices may be made resulting in sets of reduced widths γ_p^2 and γ_α^2. These values, however, are very close to the "best" values for the reduced widths γ_n^2 and γ_α^2 of the corresponding mirror state in the Li^7 nucleus as given by Gabbard (1961). The discrepancy between the previously reported value of γ_α^2 for the Be^{7*} state (Marion, 1956) and the γ_α^2 for the corresponding Li^{7*} state (Gabbard, 1961) appears to be a result of a computational error. Since there was no criterion for making a different choice, Gabbard's values were then used to compute the resonant parameters of the $5/2^-$ p-wave state in Be^7. The resonant energy of the state was determined from the elastic scattering data at 90°. This data is shown in figure 15. At

this angle the p-wave interference terms of equation 97 disappear leaving only the resonant contribution of the p-wave state.

$$\sigma_{\frac{5}{2}} = \frac{9}{50\, k_p^2} \left[(f_{\frac{5}{2}} - 1)^2 + g_{\frac{5}{2}}^2 \right] \tag{116}$$

This term may be written as a function of the resonant phase shift as follows:

$$\sigma_{\frac{5}{2}} = \frac{18}{25\, k_p^2} \left(\frac{\Gamma_p}{\Gamma} \right)^2 \sin^2 \delta_{\frac{5}{2}} \tag{117}$$

The total width Γ and the partial widths Γ_p and Γ_a were calculated as functions of energy using Gabbard's values for γ_p^2 and γ_a^2 and equations 112 and 115. Since this state is very broad the resonant energy was computed from equations 88, 89, and 91 which become in this case

$$E_R = E_\lambda + \Delta_\lambda \tag{118}$$

$$\Delta_\lambda = \Delta_p + \Delta_a$$

$$\Delta_p = -\frac{\gamma_p^2}{a_p} \left[1 + \frac{d(\ln A_1)}{d(\ln k_p a_p)} \right]$$

$$\Delta_a = -\frac{\gamma_p^2}{a_a} \left[3 + \frac{d(\ln A_3)}{d(\ln k_a a_a)} \right] \tag{119}$$

The above level shifts were calculated with the aid of the graphs of Coulomb wave functions of Sharp et al. (Sharp, 1955), and were determined from the slopes of the A_ℓ^2 versus ka graphs. The resonant energy E_λ was chosen so that when the calculated p-wave

resonant cross section equation 117, is added to the calculated Rutherford cross section, equation 70, the resulting curve is symmetrically placed beneath the measured curve.

The p-wave reaction cross section for the $5/2^-$ state may also be written in terms of the resonant phase shift

$$\sigma_R(\tfrac{5}{2}) = \frac{4\pi}{k_p^2}\left(\frac{\Gamma_a}{\Gamma}\right)\left(\frac{\Gamma_p}{\Gamma}\right)\sin^2\delta_{\frac{5}{2}} \qquad (120)$$

This was calculated as a function of energy and subtracted from the measured integrated reaction cross section to give the s-wave reaction background σ_R (s-wave) which is necessary in the computation of the scattering cross section (see figure 42). The p-wave scattering amplitudes were then calculated for the twenty-five energies from equation 108. The variation of this scattering amplitude in the complex plane is shown in figure 48. The coefficients $H(\theta)$ and $G(\theta)$ were then calculated for the six angles at each of the twenty-five energies. The coefficient $D(\theta)$ cannot be calculated completely since the factor Z given by equation 103 contains the unknown s-wave 3/2 channel spin scattering amplitude; however, Z at a given energy must be the same for all angles.

If a scattering cross section can be described in terms of s-waves only, then at each energy all of the straight lines must intersect at some point (X, Y). If the reaction cross section is also known, then the function U is determined. For the case of two channel spins there are two complex scattering amplitudes and hence four unknown s-wave parameters. The quantities X, Y, and U defined by equations

94 and 95 give only three relations between the four unknowns. However, if there is a p-wave state present, then the s-wave, p-wave interference term will give a fourth relation between the unknown s-wave parameters. In this particular case the relation is given by the coefficient Z as defined in equation 103 and must also be determined from the scattering cross section. Of the four equations relating U, X, Y, and Z to $f_{1/2}$, $g_{1/2}$, $f_{3/2}$, and $g_{3/2}$, three are linear and one quadratic. The unknowns $f_{1/2}$ and $g_{1/2}$ may be eliminated from the equations 94 and 95, giving an equation for $f_{3/2}$, $g_{3/2}$ which is just a circle in the complex plane with the center at X, Y and the radius a function of X, Y, and U.

$$\left(f_{\frac{3}{2}} - X\right)^2 + \left(g_{\frac{3}{2}} - Y\right)^2 = \frac{1}{2}\left[(1-U) - (X^2+Y^2)\right] \tag{121}$$

The equation 103 is just a straight line for $f_{3/2}$, $g_{3/2}$ in the complex plane with a slope dependent only on the p-wave state and an intercept which is a function of Z.

$$g_{\frac{3}{2}} = -S f_{\frac{3}{2}} + (S + Z) \tag{122}$$

If a solution for $f_{3/2}$, $g_{3/2}$ is possible, the straight line must intersect the circle and will in general give two solutions for the 3/2 complex scattering amplitude. The restriction that the complex scattering amplitudes $(f_{1/2}, g_{1/2})$ and $(f_{3/2}, g_{3/2})$ must lie within the unit circle, the restrictions on (X, Y), and the requirement of smoothly varying curves for the points $(f_{1/2}, g_{1/2})$, $(f_{3/2}, g_{3/2})$ and (X, Y), in the

complex plane as a function of energy provide a basis for making a choice between the two solutions. The complex point $(f_{1/2}, g_{1/2})$ may also be found geometrically, from equations 94, by constructing a straight line from the point $(f_{3/2}, g_{3/2})$ through the point (X, Y) to a distance which is twice that of the distance between $(f_{3/2}, g_{3/2})$ and (X, Y).

The procedure used to determine the s-wave parameters (see figures 47 and 49) was as follows: If the six straight lines for X, Y do not intersect at some point in the complex plane within experimental error, then the coefficient $H(\theta)$ was added to each $B(\theta)$. If the lines intersect, then this would indicate a value of zero for Z. If they do not, then a value of Z may be chosen and the six coefficients $ZG(\theta)$ determined. These are then added to the intercepts $B(\theta) + H(\theta)$. If the lines still do not intersect, a different value for Z may be chosen and the procedure repeated. If the lines do then intersect for some value of Z and the point (X, Y) is within the circle $(1 - U)^{1/2}$, and the straight line for $f_{3/2}$, $g_{3/2}$ intersects with the circle for $f_{3/2}$, $g_{3/2}$ and the points $(f_{3/2}, g_{3/2})$ and $(f_{1/2}, g_{1/2})$ lie within the unit circle, and all three of the complex points are a smooth extension of the three curves constructed previously at lower energies; then this solution is taken to be an acceptable one.

The s-wave, p-wave interference term in the cross section may be written as

$$\sigma_{sp}(E, \theta) = \sigma_{sp}(E) \cos \theta \qquad (123)$$

where $\sigma_{sp}(E)$ is related to the coefficient Z by

$$\sigma_{sp}(E) = \frac{1}{2k_p^2}\left(\frac{\Gamma_p}{\Gamma}\right)\{\sin[2\delta_{\frac{5}{2}} + 2(\eta_1-\eta_0)] - \sin 2(\eta_1-\eta_0)\}Z \qquad (124)$$

The variation of this quantity as a function of energy was computed from the Z's determined in the analysis and is shown in figure 50. The above technique was then used, beginning at low energies and proceeding to higher energies, to determine an acceptable set of s-wave parameters $f_{1/2}$, $g_{1/2}$, $f_{3/2}$ and $g_{3/2}$. The resulting complex points are shown in figure 48 along with the points (X, Y) and $(f_{5/2}, g_{5/2})$. Table 3 gives the numerical values of these quantities obtained in the analysis.

At each energy these six values for $f_{1/2}$, $g_{1/2}$, $f_{3/2}$, $g_{3/2}$, $f_{5/2}$, $g_{5/2}$ were substituted into equation 97 for each of the six angles and values of $\frac{d\sigma}{d\Omega}$ / R obtained. The solid curves drawn on each angular distribution represent the results of these calculations.

Given this set of s-wave parameters as a function of energy it was then possible to calculate the s-wave scattering cross section at 90° as a function of energy and to add this contribution to the sum of the Rutherford scattering cross section and the resonant p-wave scattering cross section to give the scattering cross sections predicted by equation 97 at this angle. The result is shown in figure 15 and appears to be a reasonable fit to the measured scattering cross section.

IV. CONCLUSIONS

Over the region studied, equation 97 appears to describe the measured elastic scattering cross section. The p-wave scattering is consistant with resonant scattering through a state of spin and parity $J^{\pi} = 5/2^{-}$ with resonant parameters in agreement with those from the mirror level in Li^7 and with the $Li^6(p, \alpha)He^3$ reaction cross section.* The s-wave scattering phase shift in the $3/2^{+}$ spin channel (figure 51) does not show a resonance in the region from 0.45 to 2.9 Mev but qualitatively follows the energy variation of charged hard sphere scattering with an interaction radius of about 2 fermis. Hence if a $3/2^{+}$ state exists at about 6.35 Mev excitation in the compound nucleus Be^7, it must have a small Γ_p/Γ and a large Γ_α/Γ. This state should then show up in the elastic scattering of He^3's from He^4. It should also be noted that the mirror level of this proposed state could not be excited in the $Li^6(d, p)Li^7$ reaction. (Hamburger, 1960) This evidence also suggests a small value of Γ_n/Γ for this state. Of possible interest here are the cluster model calculations of Pearlstein (1960) and Khanna (1961) who conclude that neither an alpha-particle plus mass-three clustering, nor a neutron plus Li^6 cluster, will yield the proposed $3/2^{+}$ state. The p-wave $5/2^{-}$ state at about 7.2 Mev excitation is now usually assigned the configuration $^4P_{5/2}$, (Inglis, 1953; Marion, 1957) on an L-S coupling model. These calculations also predict a state with configuration $^2F_{5/2}$ somewhere in the excitation range, ~5 to ~7 Mev.

*The possibility of a $3/2^{-}$ assignment for the p-wave state cannot be excluded. A $1/2^{-}$ assignment is inconsistent with the data. (See Appendix III.)

If such a state falls within the region corresponding to 0.45 Mev $\leq E_p \leq$ 1.4 Mev, the present experiment suggests that the state must have a small value of Γ_p/Γ. (See figure 46.)

The s-wave scattering phase shift in the $1/2^+$ spin channel has qualitatively the same behavior as that in the $3/2^+$ channel at low energy but begins to exhibit resonant behavior at about 1.5 Mev and goes through $\delta = \pi/2$ at about 2.76 Mev. This suggests the presence of a broad $1/2^+$ s-wave state in Be^7 at an excitation energy of about 8 Mev, although the resonance energy may not be accurately given by the present analysis.

Resonant parameters for the three states discussed above are listed in table 4. These parameters are consistent with the measured elastic scattering cross section for $Li^6(p, p)Li^6$ and the reaction cross section for $Li^6(p, \alpha)He^3$. The parameters for the $3/2^+$ state (proposed by Marion to explain the energy and angular variation of the $Li^6(p, \alpha)He^3$ reaction) were obtained from the re-adjusted $Li^6(p, \alpha)He^3$ integrated reaction cross section, using the scattering data to make a choice between the two possible sets of values for Γ_p/Γ and Γ_α/Γ. The $1/2^+$ state seems necessary to understand the scattering data in terms of s- and p-waves alone. An analysis of the scattering data of Harrison and Whitehead (Harrison, 1961) in terms of s-, p-, and d-waves should shed further light on this region. The parameters for the p-wave $5/2^-$ mirror level in Li^7 as given by Gabbard (1961) are also shown in table 5 for comparison.

APPENDIX I

Calculation of Measured Elastic Scattering Cross Section

An example of the reduction of the measured yield to scattering cross section will be given for the data shown on the Li^6 profile in figure 5. The relation between yield and laboratory cross section is given by equation 19 as follows:

$$\frac{d\sigma(E_1, \theta)}{d\Omega} = \frac{N_s}{n}\left(\frac{ZeR}{2CV\Omega_L}\right)[\alpha\epsilon(E_{1B}) + \beta\epsilon(E_{20})]\ \frac{N}{E_{20}}$$

where

$$\alpha = \frac{\partial E_2}{\partial E_1}\ ; \quad \beta = \frac{\cos\theta_1}{\cos\theta_2}$$

The resolution-to-solid angle ratio and the factor $Ze/2CV$ was determined as a product $(ZeR/2CV\Omega_L)$ by scattering protons from copper just before and after the particular Li^6 run.

The energies E_{1B} and E_{20} for the copper scattering were determined from equation 28 and 30.

E_{1B} = 1.298 Mev

E_{20} = 1.252 Mev Cu(p, p)Cu

$\theta_L = 81^o13'$; $\alpha = 0.9734$; $\beta = 1$

$\theta_{CM} = 82^o14'$

$\frac{d\Omega_{CM}}{d\Omega_L}$ = 1.0047 from equations 25 and 26

The Rutherford scattering cross section equation 70 may be written

$$R = 1.296\left[Z_1 Z_0 \left(\frac{M_1+M_0}{M_0}\right) \frac{\csc^2 \theta_{CM/2}}{E_1} \right]^2 \times 10^{-3} \text{ barns/steradian}$$

The laboratory energy E_1 was computed from equation 22 which becomes in this case

$$E_1 = \frac{\eta E_{1B} + E_{20}}{\alpha + \eta}$$

where

$$\eta = \frac{\epsilon(\overline{E}_2)}{\epsilon(\overline{E}_1)} = \frac{\epsilon(E_{20})}{\epsilon(\overline{E}_{1B})}$$

From the stopping cross section curve for protons on copper (Whaling, 1956)

$$\epsilon(E_{1B}) = 11.1 \times 10^{-15} \text{ ev-cm}^2$$

$$\epsilon(E_{20}) = 11.3 \times 10^{-15} \text{ ev-cm}^2$$

$$\eta = 1.018$$

Hence

$$E_1 = 1.292 \text{ Mev}$$

The Rutherford cross section then becomes

$$R = 3.600 \text{ barns/steradian}$$

which in the laboratory system is

$$\frac{d\sigma(E_1, \theta)}{d\Omega} = \left(\frac{d\Omega_{CM}}{d\Omega_L}\right) R = 3.617 \text{ barns/steradian}$$

$$\alpha\epsilon(E_{1B}) + \beta\epsilon(E_{20}) = 22.10 \times 10^{-15} \text{ ev-cm}^2$$

$\frac{N_s}{n} = 1$ for pure copper (an average mass of 63.55 a. m. u. was assumed)

$N = 9.361 \times 10^4$ counts (corrected for dead time of apparatus)

Hence

$$\left(\frac{ZeR}{2CV\Omega_L}\right) = \frac{E_{20}\dfrac{d\sigma(E_1, \theta)}{d\Omega}}{\dfrac{N_s}{n}\left(\alpha\epsilon(E_{1B}) + \beta\epsilon(E_{20})\right) N}$$

$$\left(\frac{ZeR}{2CV\Omega_L}\right) = \frac{(1.252 \times 10^{-6})(3.617 \times 10^{-24})}{1(22.10 \times 10^{-15})(9.361 \times 10^4)} = 2.189 \times 10^{-9}$$

The energies E_{1B} and E_{20} for the Li^6 scattering were also determined from equations 28 and 30.

$E_{1B} = 1.298$ Mev

$E_{20} = 0.9527$ Mev

$Li^6(p, p)Li^6$

$\theta_L = 81^\circ 13'$; $\alpha = 0.7510$; $\beta = 1$

$\theta_{CM} = 90^\circ 45'$

$$\frac{d\Omega_L}{d\Omega_{CM}} = 0.9634$$

From the measured stopping cross section of protons in lithium (figure 12)

$\epsilon(E_{1B}) \simeq 2.10 \times 10^{-15}$ ev-cm^2

$\epsilon(E_{20}) \simeq 2.67 \times 10^{-15}$ ev-cm^2

$\eta = 1.271$

$E_1 = 1.287$ Mev

The Rutherford cross section is

$R = 0.0374$ barns/steradian

$\alpha\epsilon(E_{1B}) + \beta\epsilon(E_{20}) = 4.247 \times 10^{-15}$ ev-cm^2

$\frac{N_s}{n}$ = 1.007 (from the spectroscopic analysis given by the supplier of the Li)

$N_{ave} = 7.900 \times 10^3$ counts

Background = 490 counts

The yield becomes

$N = 7.410 \times 10^3$ counts

Equation 19 then gives for the laboratory scattering cross section for protons with laboratory energy E_1(Lab) = 1.287 Mev from Li^6 nuclei at a center-of-mass angle of 90° 45'

$$\frac{d\sigma}{d\Omega})_L = \frac{(1.007)(2.189 \times 10^{-9})(4.247 \times 10^{-15})(7.410 \times 10^3)}{(0.9527 \times 10^6)}$$

$$= 0.07281 \text{ barns/steradian}$$

From equation 24 the center-of-mass cross section becomes

$$\frac{d\sigma}{d\Omega})_{CM} = (0.9634)(0.07281) = 0.07015 \text{ barns/steradian}$$

The ratio of the elastic scattering cross section to the Rutherford cross section is then

$$\frac{\frac{d\sigma}{d\Omega})_{CM}}{R} = \frac{(0.07015)}{(0.03744)} = 1.874$$

E_1(Lab) = 1.287 Mev

θ_{CM} = 90° 45'

APPENDIX II

Determination of S-wave Scattering Amplitudes

An example of the scattering analysis will be given for the case of E_1(Lab) = 1.879 Mev. Since the method used is described in Section III-c only an outline of the procedure with definite numbers will be given here. A program was written so that most of the calculations could be made on the Burrough's 220 computer. An attempt to fit the data with s-wave protons alone was made first by computing the values of the slopes of the six lines $Y = A(\theta)X + B(\theta)$ and the six intercepts. The input parameters for this part of the program are (see Tables 1 and 5)

Laboratory incident proton energy, E_1

Center-of-mass s-wave integrated reaction cross section σ_R

Center-of-mass angle θ_{CM}

Differential elastic scattering center-of-mass cross section $d\sigma(\theta)/d\Omega$

The computer calculates equation 99 which gives $A(\theta)$ and equation 101 which gives $B(\theta)$. In addition the computer calculates $-B(\theta)/A(\theta)$ and two other quantities $b(\theta)$ and $c(\theta)$ defined by the following equations:

$$b(\theta) = \frac{\cos \xi(\theta)}{k(R(\theta))^{1/2}} \tag{125}$$

$$c(\theta) = 1 - \frac{\sigma_R}{4\pi R(\theta)} \tag{126}$$

The quantity $-B(\theta)/A(\theta)$ is useful in plotting the straight lines

and the quantities $b(\theta)$ and $c(\theta)$ are helpful in computing the ratio of the measured elastic scattering cross section to the Rutherford scattering cross section which is now given (for s-waves) by

$$\frac{\frac{d\sigma(\theta)}{d\Omega}}{R(\theta)} = b(\theta)[A(\theta)(X-1) - Y] + c(\theta) \qquad (127)$$

For the case of E_1(Lab) = 1.879 Mev these parameters were computed to be (from table 5, σ_R(s-wave) $\simeq$ 0.068 barns.)

θ_{CM}	A	B	-B/A	b	c
$70^\circ 41'$	-0.6424	-1.327	-2.066	1.796	0.8656
$90^\circ 45'$	-1.265	-0.8757	-0.6921	2.847	0.6919
$110^\circ 48'$	-1.841	-0.6855	-0.3724	3.881	0.4485
$126^\circ 6'$	-2.224	-0.7999	-0.3596	4.579	0.2413
$140^\circ 53'$	-2.527	-1.343	-0.5314	5.128	0.0530
$159^\circ 7'$	-2.784	-2.079	-0.7466	5.590	-0.1238

The six lines were then plotted in the complex plane and are shown in figure 47. Since they did not intersect at some point within the circle $(1 - U)^{1/2}$ within experimental error, it was assumed that the resonance at this energy was not an s-wave resonance. Resonant parameters for an assumed p-wave $5/2^-$ state were then estimated by the procedure given on page 45 and resulted in the following set of values at the energy E_1(Lab) = 1.879 Mev (see Table 5)

$$\Gamma_p(CM) = 0.834$$
$$\Gamma(CM) = 0.872$$

$$E_R(CM) = 1.559$$

A program was also written for the computer to calculate the quantities $f_{5/2}$, $g_{5/2}$, S, G(θ), and H(θ). These are defined in equations 108, 109, 104, 105, and 106. The resulting values are

$$f_{5/2} = -0.888$$

$$g_{5/2} = -0.218$$

$$S = 1.009$$

θ_{CM}	G	H	ZG
$70^{\circ}41'$	-0.4604	1.790	0.2026
$90^{\circ}45'$	0.02636	1.944	-0.0116
$110^{\circ}48'$	0.9389	2.537	-0.413
$126^{\circ}6'$	1.816	3.483	-0.799
$140^{\circ}53'$	2.666	4.688	-1.173
$159^{\circ}7'$	3.494	6.100	-1.537

The above intercepts H(θ) were then added to the s-wave intercepts to give the dashed lines in figure 47. It is evident that there is still no intersection and the s-wave, p-wave interference intercepts ZG(θ) must be added to the intercepts B(θ) + H(θ). Various values of Z were tried with the result that only the choice $Z = -(0.44 \pm 0.02)$ would yield an acceptable solution for the s-wave scattering amplitudes. The values of ZG(θ) are also included above for this value of Z. These additional intercepts were added to the B(θ) + H(θ) intercepts to give the lines plotted in figure 49. The choice

of Z was made simultaneously with the choice for the complex point (X, Y) and the graphical solution of equations 121 and 122 for the complex point $(f_{3/2}, g_{3/2})$ and the complex point $(f_{1/2}, g_{1/2})$. Most solutions for the s-wave scattering amplitudes were discarded because they gave a complex point for $(f_{1/2}, g_{1/2})$ outside the unit circle.

An additional restriction on the above choice was that all three complex points be reasonable extrapolations of the values found at lower and higher energies. The numbers actually obtained were

$$X = 0.82 \quad ; \quad Y = 0.02$$

$$f_{3/2} = 0.85 \quad ; \quad g_{3/2} = -0.29$$

$$f_{1/2} = 0.77 \quad ; \quad g_{1/2} = 0.63$$

$$\{\tfrac{1}{2}[(1-U)-(X^2+Y^2)]\}^{1/2} = 0.31$$

The angular distribution was then calculated from the equation

$$\frac{\frac{d\sigma(\theta)}{d\Omega}}{R(\theta)} = b(\theta)[A(\theta)(X-1)-Y + H(\theta) + ZG(\theta)] + c(\theta) \qquad (128)$$

which gave for $E_1(\text{Lab}) = 1.879$ Mev the following ratios

θ_{CM}	$70^\circ 41'$	$90^\circ 45'$	$110^\circ 48'$	$126^\circ 6'$	$140^\circ 53'$	$159^\circ 7'$
$\frac{d\sigma}{d\Omega}/R$	4.62	6.78	9.90	14.3	20.3	28.1
$\frac{d\sigma}{d\Omega}_{exp}/R$	4.37	6.80	10.3	14.1	20.0	27.1

The second line gives the experimentally determined ratios which are to be compared with the calculated ratios.

APPENDIX III

Consideration of the possible $1/2^-$ and $3/2^-$ assignments for the 1.84 Mev p-wave resonance

If the single p-wave resonance assumed in the analysis has the assignment $J^\pi = 1/2^-$ or $3/2^-$, the state may be formed through either spin channel and a channel spin mixing parameter must be introduced. The scattering amplitude for the $1/2^-$ assignment then becomes

$$f_{ijpp}^{1/2^-} = a_i a_j (f_{1/2^-} + i g_{1/2^-} - 1) \quad i, j = 1/2 \text{ or } 3/2 \qquad (129)$$

where $a_{1/2}^2$ is the probability of forming the $1/2^-$ p-wave state through the $1/2$ spin channel and $a_{3/2}^2$ is the probability of forming the $1/2^-$ p-wave state through the $3/2$ spin channel. Since the a_i^2 are probabilities and there are only two spin channels, the following relation must hold

$$a_{1/2}^2 + a_{3/2}^2 = 1 \qquad (130)$$

Since there is only one additional quantity involved, one speaks of the channel spin mixing parameter M which is defined here to be equal to $a_{1/2}^2$. The f and g are defined as in equations 108 and 109.

The scattering cross section is then found from the amplitude matrix in the same way as that described for the case of $J^\pi = 5/2^-$. All of the terms for a $J^\pi = 1/2^-$ p-wave state must be considered including the channel spin flip terms (i. e. scattering events which involve a change of channel spin). The correctness of the p-wave resonant term in the cross section may be checked by integrating the cross section over solid

angle. The interference terms drop out and the result must agree with the Breit-Wigner formula at resonance

$$\sigma_{\text{Scatt.}}(\text{Res.}) = \frac{2J+1}{6}\,\frac{4\pi}{k^2}\left(\frac{\Gamma_\rho}{\Gamma}\right)^2 \tag{131}$$

The scattering cross section for a single $J^\pi = 1/2^-$ p-wave resonant state is found to be

$$\frac{d\sigma}{d\Omega}(\theta, E) = R + \left(\frac{\sqrt{R}}{k}\sin\xi - \frac{1}{2k^2}\right)(X-1) - \frac{\sqrt{R}}{k}\cos\xi\, Y - \frac{U}{4k^2}$$

$$+ \frac{1}{3}\left(\frac{Z}{2k^2}\right)\left[(f_{1/2^-} - 1)\sin 2(\eta_1-\eta_o) + g_{1/2^-}\cos 2(\eta_1-\eta_o)\right]\cos\theta$$

$$- \frac{1}{3}\frac{\sqrt{R}}{k}\left\{(f_{1/2^-} - 1)\sin[2(\eta_1-\eta_o)-\xi] + g_{1/2^-}\cos[2(\eta_1-\eta_o)-\xi]\right\}\cos\theta$$

$$+ \frac{1}{12k^2}\left[(f_{1/2^-} - 1)^2 + g^2_{1/2^-}\right] \tag{132}$$

The coefficient Z is defined similarly to equation 103 but now

$$Z = \left[a^2_{1/2}f_{1/2} + a^2_{3/2}f_{3/2^-} - 1\right]S + \left(a^2_{1/2}g_{1/2^+} + a^2_{3/2}g_{3/2}\right) \tag{133}$$

The coefficient S is defined as in equation 104 with the index $5/2$ replaced by $1/2^-$. The s-wave $1/2$ channel spin parameters, $f_{1/2}$ and $g_{1/2}$, may be eliminated from the equation for Z by using equations 94. This then gives a straight line equation in terms of the s-wave $3/2$ spin channel parameters, $f_{3/2}$ and $g_{3/2}$, which has the same form as equation 122 with the same slope but different intercept.

$$g_{3/2} = -S\,f_{3/2} + \frac{Z + S - 3M(SX + Y)}{1 - 3M} \tag{134}$$

This equation combined with the circle equation 121 must then yield an acceptable solution for the s-wave scattering if this choice of J^{π} is correct. The p-wave resonant parameters may be found from the $Li^6(p, \alpha)He^3$ reaction cross section by the procedure given on page 45. An arbitrary s-wave background was chosen which was similar to that used for the $J^{\pi} = 5/2^-$ case.

With the assumption that only s- and p-wave contributions are present, the assignment $J^{\pi} = 1/2^-$ is excluded by the experimental data. This is primarily due to the fact that the p-wave intensity term is isotropic for $J = 1/2$, and this restriction makes it impossible to fit the observed angular distributions.

The analysis in terms of a $3/2^-$ p-wave state proceeds in exactly the same manner as that for the $1/2^-$ case. The scattering amplitude is given by

$$f_{ijpp}^{3/2^-} = \alpha_i \alpha_j (f_{3/2^-} + i g_{3/2^-} - 1) \quad i, j = 1/2 \text{ or } 3/2 \qquad (135)$$

The channel spin mixing parameter M is defined in the same way as above. The scattering cross section then becomes

$$\begin{aligned}\frac{d\sigma}{d\Omega}(\theta, E) = R + \left(\frac{\sqrt{R}}{k}\sin\xi - \frac{1}{2k^2}\right)(X-1) - \frac{\sqrt{R}}{k}\cos\xi\, Y - \frac{U}{4k^2} \\ + \frac{2}{3}\left(\frac{Z}{2k^2}\right)\left[(f_{3/2^-} - 1)\sin 2(\eta_1 - \eta_o) + g_{3/2^-}\cos 2(\eta_1 - \eta_o)\right]\cos\theta \\ - \frac{2}{3}\frac{\sqrt{R}}{k}\left\{(f_{3/2^-} - 1)\sin[2(\eta_1 - \eta_o) - \xi] + g_{3/2^-}\cos[2(\eta_1 - \eta_o) - \xi]\right\}\cos\theta \\ + \frac{1}{300k^2}\left[\beta + 3(50-\beta)\cos^2\theta\right]\left[(f_{3/2^-} - 1)^2 + g_{3/2^-}^2\right] \qquad (136)\end{aligned}$$

where

$$\beta = 34 + 72M - 81M^2 \qquad (137)$$

Z is defined as in equation 133. The straight line equation for the 3/2 channel spin s-wave parameters is given by equation 134 and the circle equation is given by equation 121.

Various values of channel spin mixing parameter M were chosen and an analysis carried out in the same manner as for the $5/2^-$ case and the $1/2^-$ case. The case of M = 1/2 (i.e. if the $3/2^-$ state is formed equally through both spin channels) may be excluded since it gives an almost isotropic p-wave intensity contribution to the scattering. However, for the cases of the $3/2^-$ state being formed almost entirely through either the 1/2 spin channel or the 3/2 spin channel, a fit to the data can be made with a different choice of s-wave background. In these cases the s-wave background does not show resonant behavior in the 1/2 channel spin but may indicate resonant behavior in the 3/2 spin channel at a much higher energy.

REFERENCES

1. F. Ajzenberg-Selove, T. Lauritsen, 1959, Nuclear Physics, 11, 1.
2. S. K. Allison, 1958, R. M. P. 30, 1137.
3. M. Bader, R. E. Pixley, F. S. Mozer and W. Whaling, 1956, P. R. 103, 32.
4. K. Bardin, 1961, Ph. D. Thesis, California Institute of Technology.
5. S. Bashkin and H. T. Richards, 1951, P. R. 84, 1124.
6. S. Bashkin and R. R. Carlson, 1955, P. R. 97, 1245.
7. D. Bohm, 1951, "Quantum Theory," Prentice-Hall Inc., New York, p. 537.
8. A. B. Brown, C. W. Snyder, W. A. Fowler and C. C. Lauritsen, 1951, P. R. 82, 159.
9. W. E. Burcham and J. M. Freeman, 1950, Phil. Mag. 41, 921.
10. R. F. Christy, 1956, Physica XXII, 1009.
11. E. R. Cohen, 1949, Ph. D. Thesis, California Institute of Technology.
12. W. A. Fowler, C. C. Lauritsen and T. Lauritsen, 1947, R. S. I. 18, 818.
13. F. Gabbard, 1961, Private communication to T. Lauritsen.
14. W. D. Harrison and A. B. Whitehead, 1961, B. A. P. S. II-6, 505.
15. D. R. Inglis, 1953, R. M. P. 25, 390.
16. C. H. Johnson, H. B. Willard and J. K. Bair, 1954, P. R. 96, 985.
17. F. C. Khanna, Y. C. Tang and K. Wildermuth, 1961, P. R. 124, 515.
18. C. C. Lauritsen, T. Lauritsen and W. A. Fowler, 1941, P. R. 59, 241.
19. J. B. Marion, G. Weber and F. S. Mozer, 1956, P. R. 104, 1402.
20. J. B. Marion, 1957, Nuclear Physics, 4, 282.

21. J. B. Marion, 1961, R. M. P. 33, 139.

22. J. A. McCray and P. Smith, 1962, to be published.

23. F. S. Mozer, 1956, Ph. D. Thesis, California Institute of Technology and F. S. Mozer, 1956, P. R. 104, 1386.

24. L. D. Pearlstein, Y. C. Tang and K. Wildermuth, 1960, Nuclear Physics, 18, 23.

25. S. Rosenblum, 1928, Ann. de Phys. 10, 408.

26. G. A. Sawyer and J. A. Phillips, 1953, Los Alamos Report 1578.

27. W. T. Sharp, H. E. Gove and E. B. Paul, 1955, A. E. C. L. No. 268, "Graphs of Coulomb Functions," Chalk River, Ontario.

28. C. W. Snyder, S. Rubin, W. A. Fowler and C. C. Lauritsen, 1950, R. S. I. 21, 852.

29. R. G. Thomas, 1951, P. R. 81, 148.

30. J. B. Warren, T. K. Alexander and G. B. Chadwick, 1956, P. R. 101, 242.

31. W. D. Warters, 1953, Ph. D. Thesis, California Institute of Technology, p. 37.

32. W. A. Wenzel, 1953, Ph. D. Thesis, California Institute of Technology, p. 54.

33. W. Whaling, 1958, Handbuch der Physik, Bd. XXXIV, p. 193.

TABLE 1

DIFFERENTIAL ELASTIC SCATTERING CROSS SECTION
(Page 28)

E_1(Lab) (Mev)	θ_{CM} (degrees)	$\frac{d\sigma}{d\Omega}$ (mb)	$\frac{d\sigma}{d\Omega}/R$	E_1(Lab) (Mev)	θ_{CM} (degrees)	$\frac{d\sigma}{d\Omega}$ (mb)	$\frac{d\sigma}{d\Omega}/R$	E_1(Lab) (Mev)	θ_{CM} (degrees)	$\frac{d\sigma}{d\Omega}$ (mb)	$\frac{d\sigma}{d\Omega}/R$
0.495	70°56'	544	0.95	0.792	70°41'	255	1.12	1.087	70°41'	138	1.14
	90°42'	252	0.99		90°42'	119	1.20		90°42'	77.9	1.48
	110°28'	152	1.06		110°28'	77.5	1.40		110°28'	60.5	2.05
	125°28'	114	1.10		125°29'	62.9	1.54		125°29'	51.3	2.38
	140°2'	88.8	1.06		140°2'	53.3	1.65		140°2'	46.2	2.69
	159°32'	78.7	1.14		159°32'	42.9	1.59		159°32'	42.2	2.95
0.594	70°41'	398	0.97	0.892	70°41'	208	1.15	1.186	70°41'	108	1.07
	90°42'	187	1.06		90°42'	101	1.29		90°42'	73.7	1.67
	110°28'	123	1.24		110°28'	66.5	1.51		110°28'	60.4	2.43
	125°29'	87.2	1.22		125°29'	54.8	1.70		125°29'	54.5	3.01
	140°2'	73.0	1.26		140°2'	49.1	1.92		140°2'	50.1	3.47
	159°32'	63.0	1.32		159°32'	40.5	1.92		159°7'	45.3	3.73
0.692	70°41'	308	1.03	0.989	70°41'	164	1.12	1.286	70°41'	96.1	1.12
	90°42'	143	1.11		90°42'	87.9	1.39		90°45'	70.2	1.87
	110°28'	85.0	1.17		110°28'	63.2	1.77		110°48'	58.8	2.82
	125°29'	69.2	1.31		125°29'	52.8	2.03		126°6'	56.5	3.70
	140°2'	56.4	1.32		140°2'	46.8	2.26		140°53'	56.3	4.62
	159°32'	47.0	1.32		159°32'	42.5	2.45		159°7'	55.6	5.38

TABLE 1 (Cont.)

E_1(Lab) (Mev)	θ_{CM} (degrees)	$\frac{d\sigma}{d\Omega}$ (mb)	$\frac{d\sigma}{d\Omega}/R$
1.386	70°41'	90.6	1.22
	90°45'	70.5	2.18
	110°48'	63.9	3.56
	126°6'	65.4	4.98
	140°53'	70.6	6.72
	159°7'	71.2	8.06
1.485	70°41'	96.2	1.49
	90°45'	80.8	2.87
	110°48'	75.7	4.84
	126°6'	82.8	7.24
	140°53'	90.4	9.89
	159°7'	98.8	12.8
1.585	70°41'	113	2.00
	90°45'	96.4	3.90
	110°48'	94.8	6.89
	126°6'	103	10.3
	140°53'	117	14.5
	159°7'	134	19.8
1.681	70°41'	151	2.98
	90°45'	116	5.28
	110°48'	111	9.10
	126°6'	120	13.5
	140°53'	138	19.4
	159°7'	157	26.0
1.780	70°41'	174	3.86
	90°45'	124	6.34
	110°48'	115	10.5
	126°6'	121	15.2
	140°53'	134	21.0
	159°7'	154	28.6
1.879	70°41'	177	4.37
	90°45'	119	6.80
	110°48'	101	10.3
	126°6'	101	14.1
	140°53'	114	20.0
	159°7'	130	27.1
1.976	70°41'	167	4.57
	90°45'	106	6.67
	110°48'	88.5	10.0
	126°6'	82.6	12.8
	140°53'	88.9	17.3
	159°7'	104	23.9
2.076	70°41'	152	4.56
	90°45'	95.5	6.60
	110°48'	74.7	9.31
	126°6'	69.5	11.9
	140°53'	74.2	15.9
	159°7'	83.2	21.1
2.174	70°41'	139	4.60
	90°45'	87.2	6.63
	110°48'	64.5	8.83
	126°6'	58.4	11.0
	140°53'	61.2	14.4
	159°7'	67.3	18.8

TABLE 1 (Cont.)

E_1(Lab) (Mev)	θ_{CM} (degrees)	$\frac{d\sigma}{d\Omega}$ (mb)	$\frac{d\sigma}{d\Omega}/R$
2.273	70°41'	130	4.70
	90°45'	79.8	6.63
	110°48'	57.4	8.58
	126°6'	52.3	10.6
	140°53'	51.4	13.2
	159°7'	56.4	17.2
2.372	70°41'	119	4.69
	90°45'	76.1	6.88
	110°48'	55.5	9.05
	126°6'	47.8	10.7
	140°53'	45.2	12.6
	159°7'	50.2	16.7
2.470	70°41'	111	4.73
	90°45'	72.4	7.10
	110°48'	52.5	9.28
	126°6'	44.5	10.8
	140°53'	41.9	12.7
	159°7'	45.4	16.3
2.570	70°41'	106	4.90
	90°45'	69.6	7.39
	110°48'	50.1	9.57
	126°6'	44.5	10.8
	140°53'	41.9	12.7
	159°7'	45.4	16.3
2.664	70°41'	104	5.17
	90°45'	67.9	7.78
	110°48'	49.6	10.2
	126°6'	41.1	11.6
	140°53'	37.7	13.3
	159°7'	38.2	16.0
2.762	70°41'	100	5.37
	90°45'	66.2	8.14
	110°48'	48.8	10.8
	126°6'	40.2	12.0
	140°53'	36.0	14.3
	159°7'	36.1	16.2
2.861	70°41'	96.7	5.54
	90°45'	64.7	8.52
	110°48'	49.2	11.7
	126°6'	39.9	13.0
	140°53'	35.3	14.4
	159°7'	34.8	16.7

TABLE 2

PROBABLE ERROR IN THE Li^6 SCATTERING CROSS SECTION
(Page 30)

RELATIVE ERROR	ESTIMATED PROBABLE ERROR (%)
1. Resolution to solid angle ratio	
Uncertainty in factor $\alpha\epsilon(E_{1B}) + \beta\epsilon(E_{20})$ due to 0.5° uncertainty in angle and 2% relative uncertainty in ϵ_{Cu}	1.4
Statistical uncertainty in Cu yield	0.5
Fluctuations in firing voltage of current integrator	0.5
Fluctuations in spectrometer energy calibrations	0.3
Uncertainty in Cu Rutherford cross section due to 0.5° error in angle and 0.5% error in E_1	
Back angles	1.0
Forward angles	1.9
2. Uncertainty in factor $\alpha\epsilon(E_{1B}) + \beta\epsilon(E_{20})$ due to 0.5° uncertainty in angle and 2% relative uncertainty in ϵ_{Li}	1.5
3. Statistical uncertainty in Li^6 yield	1.5
4. Fluctuations in firing voltage on current integrator	0.5
5. Uncertainty in target composition N_s/n	0.2
Relative probable error in cross section	
All angles	~3%

TABLE 2 (Cont.)

ABSOLUTE ERROR		ESTIMATED PROBABLE ERROR (%)
1.	Resolution to solid angle ratio	3.5
	Uncertainties are the same as for the relative error with the exception of the factor $\alpha\epsilon(E_{1B}) + \beta\epsilon(E_{20})$ which is uncertain by about 3% on an absolute scale. (Bader, 1956)	
2.	Uncertainty in factor $\alpha\epsilon(E_{1B}) + \beta\epsilon(E_{20})$ for Li	3.0
3.	Statistical uncertainty in Li^6 yield	1.5
4.	Fluctuations of firing voltage of current integrator	0.5
5.	Uncertainty in target composition N_s/n	0.2
Absolute probable error in cross section		
	All angles	~ 5%

TABLE 3

COMPLEX SCATTERING AMPLITUDES (Page 52)

E_1(Lab)	$f_{1/2}$	$g_{1/2}$	$f_{3/2}$	$g_{3/2}$
0.495	0.981	-0.035	0.981	-0.035
0.594	0.973	-0.065	0.973	-0.065
0.692	0.972	-0.068	0.972	-0.068
0.792	0.986	-0.178	0.944	-0.090
0.892	0.939	-0.106	0.982	-0.200
0.989	0.977	-0.217	0.930	-0.130
1.087	0.970	-0.240	0.927	-0.133
1.186	0.962	-0.238	0.928	-0.132
1.286	0.946	-0.215	0.930	-0.140
1.386	0.934	-0.162	0.934	-0.162
1.485	0.932	-0.160	0.932	-0.160
1.585	0.891	-0.038	0.950	-0.215
1.681	0.900	0.070	0.932	-0.240
1.780	0.874	0.424	0.880	-0.273
1.879	0.770	0.630	0.850	-0.286
1.976	0.629	0.779	0.810	-0.318
2.076	0.315	0.950	0.798	-0.323
2.174	0.143	0.987	0.770	-0.370
2.273	-0.058	0.945	0.774	-0.400
2.372	-0.235	0.880	0.760	-0.440
2.470	-0.400	0.788	0.750	-0.455
2.570	-0.470	0.710	0.727	-0.507
2.664	-0.580	0.567	0.710	-0.540
2.762	-0.650	0.465	0.700	-0.580
2.861	-0.688	0.324	0.673	-0.600

TABLE 3 (Cont.)

E_1(Lab)	X	Y	Z	$f_{5/2}$	$g_{5/2}$
0.495	0.981	-0.035	0	0.999	0.034
0.594	0.973	-0.065	0	0.998	0.061
0.692	0.972	-0.068	0	0.995	0.093
0.792	0.960	-0.120	0	0.992	0.121
0.892	0.954	-0.135	0	0.982	0.175
0.989	0.947	-0.155	0	0.964	0.253
1.087	0.942	-0.165	0	0.938	0.332
1.186	0.940	-0.165	0	0.887	0.443
1.286	0.938	-0.165	0	0.810	0.565
1.386	0.934	-0.162	0	0.659	0.725
1.485	0.932	-0.160	0.124	0.413	0.875
1.585	0.928	-0.156	0.740	0.031	0.947
1.681	0.922	-0.135	-0.550	-0.468	0.798
1.780	0.880	-0.040	-0.480	-0.844	0.334
1.879	0.820	0.020	-0.440	-0.888	-0.218
1.976	0.750	0.050	-0.433	-0.704	-0.600
2.076	0.640	0.100	-0.425	-0.461	-0.818
2.174	0.560	0.085	-0.450	-0.285	-0.905
2.273	0.500	0.050	-0.450	-0.088	-0.953
2.372	0.430	0	-0.470	0.035	-0.963
2.470	0.370	-0.040	-0.490	0.142	-0.958
2.570	0.330	-0.100	-0.534	0.209	-0.949
2.664	0.280	-0.170	-0.567	0.266	-0.938
2.762	0.250	-0.230	-0.596	0.317	-0.924
2.861	0.220	-0.290	-0.614	0.353	-0.912

TABLE 4

RESONANT PARAMETERS
(Page 54)

Nucleus	(Units)	Be^{7*}	Be^{7*}	Be^{7*}	Li^{7*}
J^{π}		$(3/2^{+})$	$(1/2^{+})$	$5/2^{-}$	$5/2^{-}$
E_R(Lab)	Mev	0.77	2.76	1.84	0.262
$\Gamma(E_R)$	Mev	1.03	1.23	0.836	0.154
E_λ	(Mev above ground)			7.58	7.70
$\Gamma_{p,n}(E_R)$	Mev	0.025	0.90	0.798	0.118
$\gamma^2_{p,n}$	Mev-f	0.17	1.82	5.02	4.85
$\theta^2_{p,n}$		0.01	0.10	0.28	0.26
$\Gamma_\alpha(E_R)$	Mev	1.00	0.33	0.038	0.036
γ^2_α	Mev-f	1.7	0.25	0.101	0.091
θ^2_α		0.20	0.03	0.012	0.012

TABLE 5

ASSUMED S-WAVE INTEGRATED REACTION CROSS SECTION AND P-WAVE RESONANT PARAMETERS (Page 59)

E_1(Lab) (Mev)	σ_R (barns)	E_R(CM) (Mev)	Γ(CM) (Mev)	Γ_p(CM) (Mev)
0.495	0.068	1.986	0.076	0.053
0.594	0.069	1.960	0.113	0.089
0.692	0.070	1.935	0.150	0.126
0.792	0.070	1.923	0.176	0.151
0.892	0.070	1.901	0.228	0.201
0.989	0.069	1.872	0.292	0.265
1.087	0.067	1.851	0.345	0.316
1.186	0.065	1.823	0.411	0.381
0.286	0.063	1.796	0.468	0.437
1.386	0.063	1.760	0.539	0.507
1.485	0.061	1.723	0.605	0.572
1.585	0.060	1.680	0.660	0.625
1.681	0.058	1.639	0.733	0.697
1.780	0.059	1.595	0.777	0.740
1.879	0.068	1.559	0.872	0.834
1.976	0.072	1.530	0.923	0.884
2.076	0.072	1.501	0.990	0.950
2.174	0.073	1.491	1.054	1.013
2.273	0.076	1.455	1.123	1.080
2.372	0.079	1.438	1.190	1.146
2.470	0.080	1.422	1.242	1.197
2.570	0.082	1.411	1.317	1.271
2.664	0.083	1.402	1.377	1.330
2.762	0.084	1.393	1.439	1.390
2.861	0.084	1.390	1.504	1.454

Figure 1

Thick Target Diagrams (Page 5)

Figure a represents the target beam geometry for a typical situation. The perpendicular to the target surface is oriented at an angle θ_1 from the direction of the incident beam and at an angle θ_2 from the direction of the exit beam. Particles which strike the front surface of the target with bombarding energy E_{1B} scatter or form a reaction at the surface and leave at some angle θ_2 with an energy E_{2B}. The magnetic spectrometer may be adjusted to accept particles which originate only within a certain lamina Δs in the target. The energy of a particle before a scattering or reaction event is given by E_1 and that after the event by E_2. Since some energy is lost by the particles in traveling from the surface to the lamina, E_1 will be less than E_{1B} and similarly the energy of the particle accepted by the spectrometer E_{20} will be less than E_2.

Figures b and c represent the scattering situation in the determination of the stopping cross section for protons in lithium. In the first case the target is just copper; in the second, copper plus a thin layer of lithium.

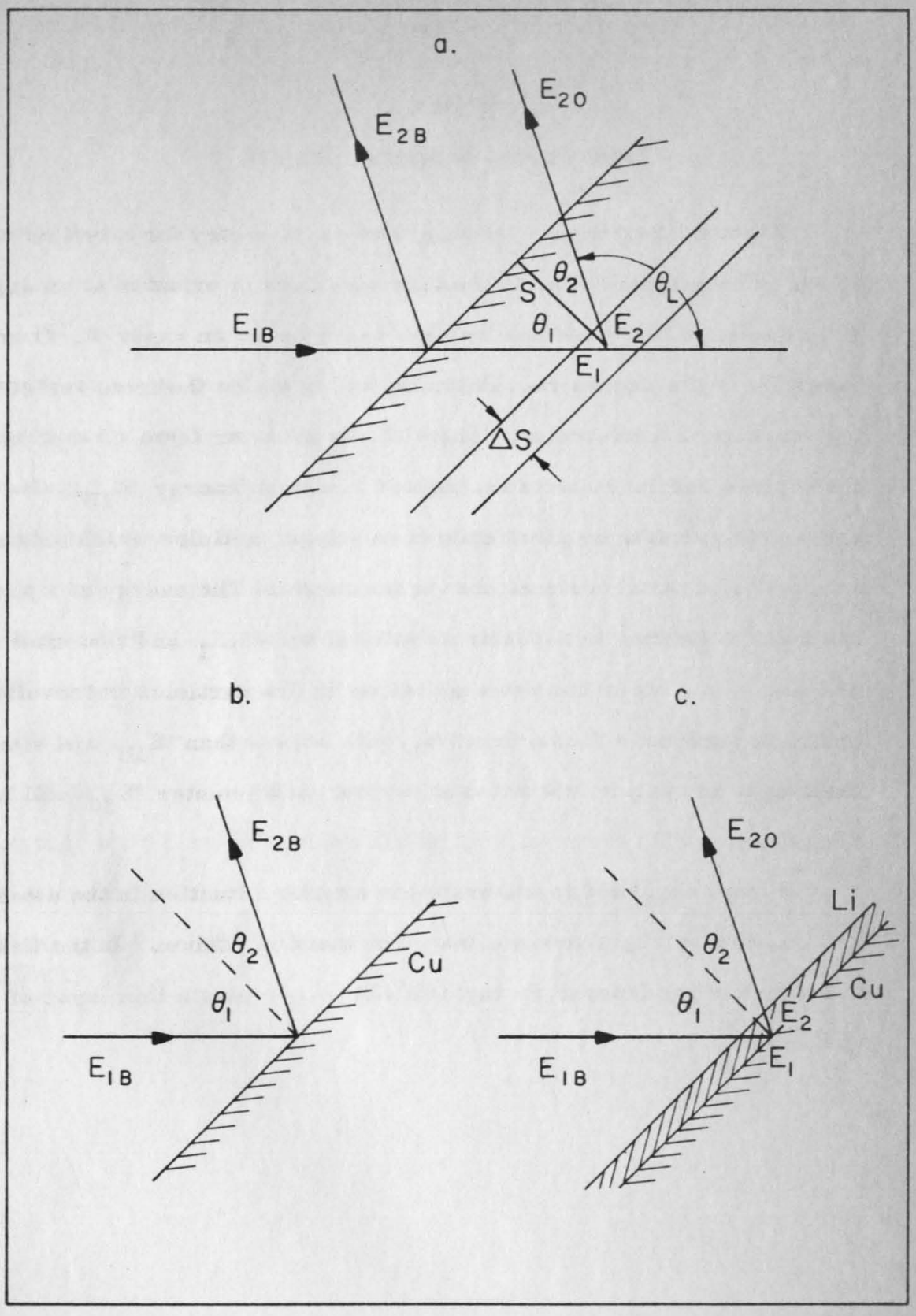
a.
E20
E2B
θ2
S
θL
θ1
E2
E1B
E1
ΔS
b.
E2B
θ2
Cu
θ1
E1B
c.
E20
Li
θ2
Cu
θ1
E2
E1B
E1

Figure 2

Spectrometer Profile of Copper Target (Page 13)

The voltage across a precision resistor is plotted on the abscissa and is proportional to the current through the fluxmeter in the magnetic spectrometer. As indicated on page 13 this current is inversely proportional to the square root of the energy of the particles accepted by the magnetic spectrometer. The yield or number of particles counted for a given charge collected is plotted on the ordinate. At a given angle the protons scattering elastically from copper will have a maximum energy corresponding to those scattered from the front surface of the target. Most of the protons will penetrate into the target, scatter at some point and also come out in the same direction as the protons scattered from the front surface. These, however, will lose energy while passing through the target and will be recorded at a lower energy. The result then is a step function with the front edge at the calculated maximum energy. This copper edge was used to calibrate the magnetic spectrometer i. e. to find the constant C_{MS} in equation 30. The incident proton energy was about 1. 3 Mev and the laboratory angle $81^{o}13'$.

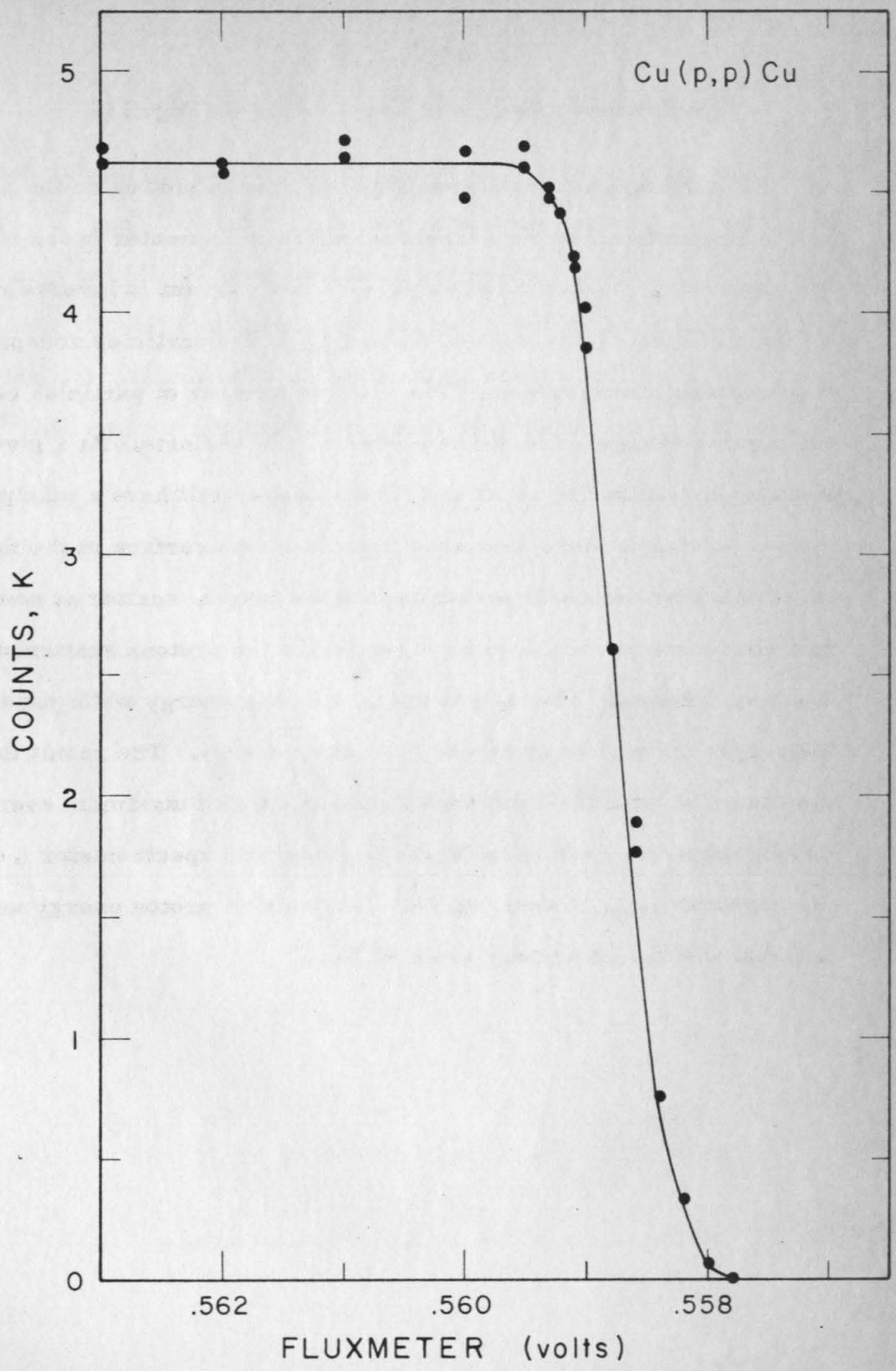
Cu(p,p)Cu
COUNTS, K
0
1
2
3
4
5
.562
.560
.558
FLUXMETER (volts)

Figure 3

Spectrometer Profile of Lithium Target (Page 13)

This profile was taken with the 10.5-inch spectrometer and a Li^6 target in the 2.5-inch scattering chamber. The O^{16} and C^{12} peaks correspond to protons which are scattered from the thin oxygen and carbon contamination layers on the surface of the lithium. The shape of the Li^6 profile is given by equation 18. The incident laboratory proton energy was about 0.80 Mev and the laboratory angle $116^\circ 54'$.

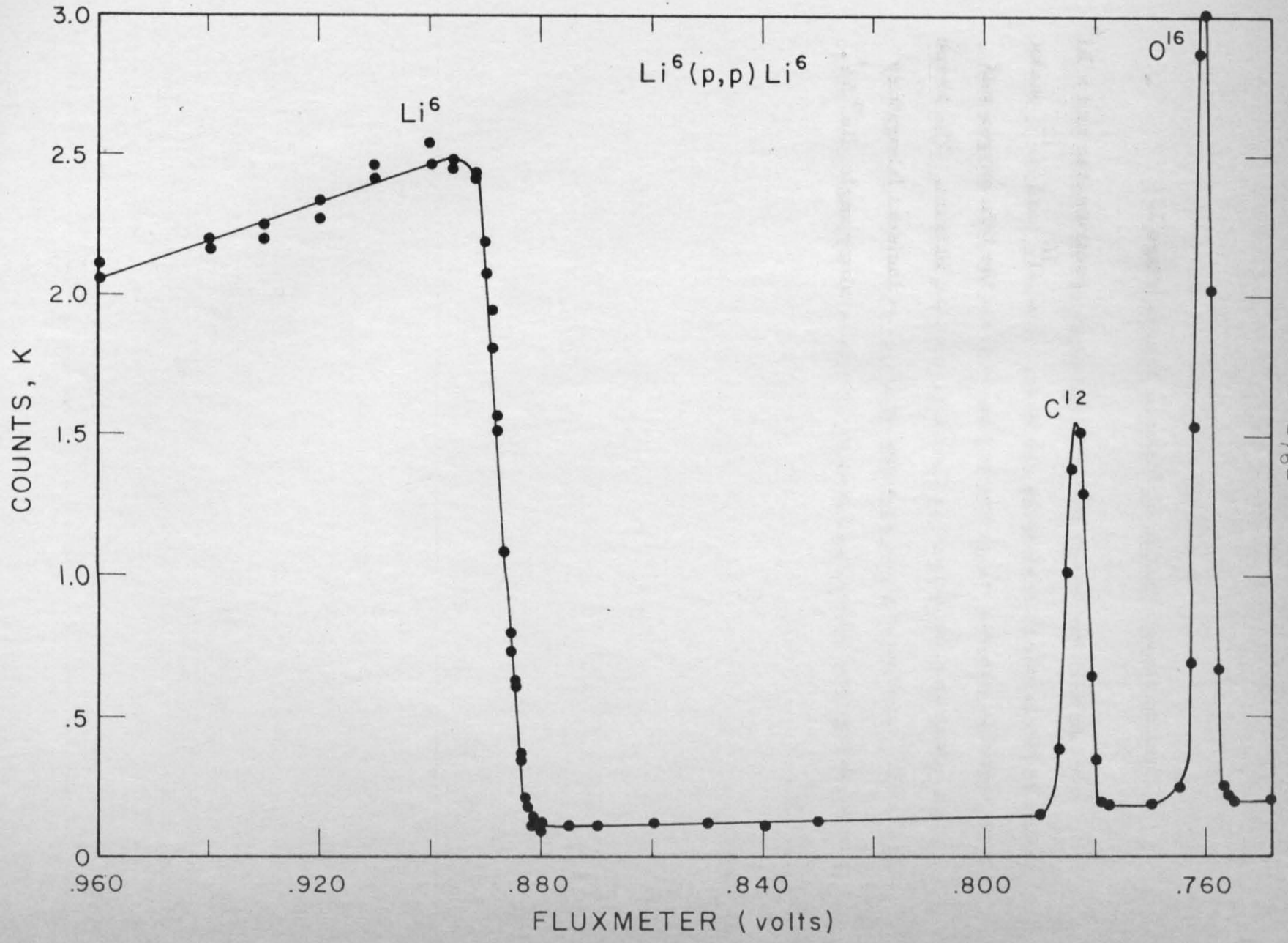
$Li^6(p,p)Li^6$
Li^6
C^{12}
O^{16}
COUNTS, K
FLUXMETER (volts)
3.0
2.5
2.0
1.5
1.0
.5
0
.960
.920
.880
.840
.800
.760

Figure 4

Spectrometer Profile of Lithium Target (Page 14)

This profile was taken with the 10.5-inch spectrometer and a Li^6 target in the 2.5-inch scattering chamber. However, since the purity of the Li^6 sample was only 95.7%, the Li^7 profile is also present. An indication of the age of a target is given by the "tail" on the C^{12} and O^{16} peaks which represent diffusion into the lithium. The incident laboratory proton energy was about 1.00 Mev and the laboratory angle $155^{o}34'$.

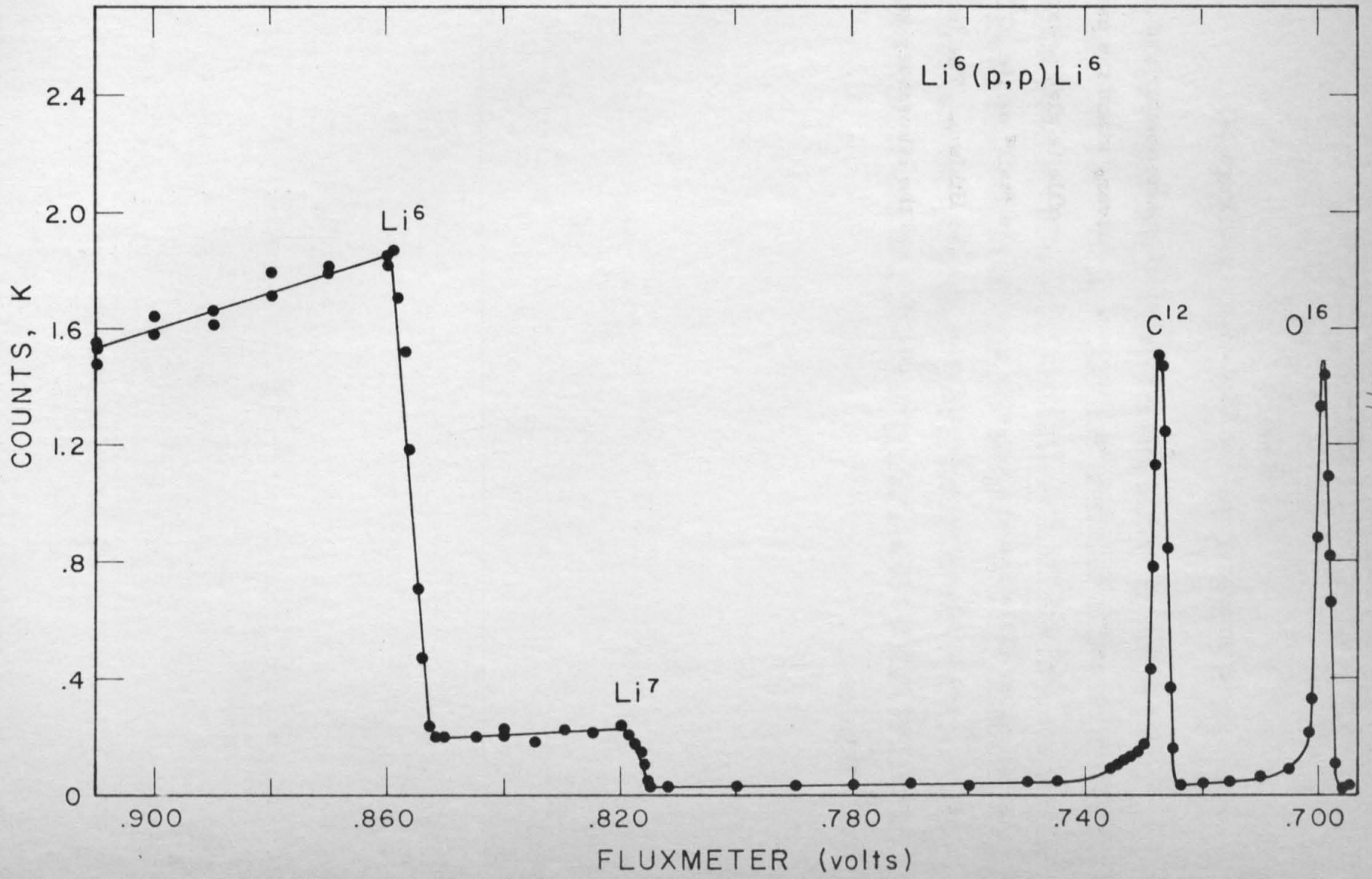
Li⁶(p,p)Li⁶
COUNTS, K
2.4
2.0
1.6
1.2
.8
.4
0
Li⁶
Li⁷
C¹²
O¹⁶
.900
.860
.820
.780
.740
.700
FLUXMETER (volts)

Figure 5

Spectrometer Profile of Lithium Target (Page 21)

This profile was taken with the 16-inch spectrometer and a Li^6 target in the 6-inch scattering chamber. The O^{16} and C^{12} peaks here, however, are much reduced because of the improved vacuum in this chamber. The Li^6 edge also appears to be sharper than the Li^6 edges found with targets in the 2.5-inch scattering chamber. The incident laboratory proton energy was about 1.30 Mev and the laboratory angle $81^{\circ}13'$.

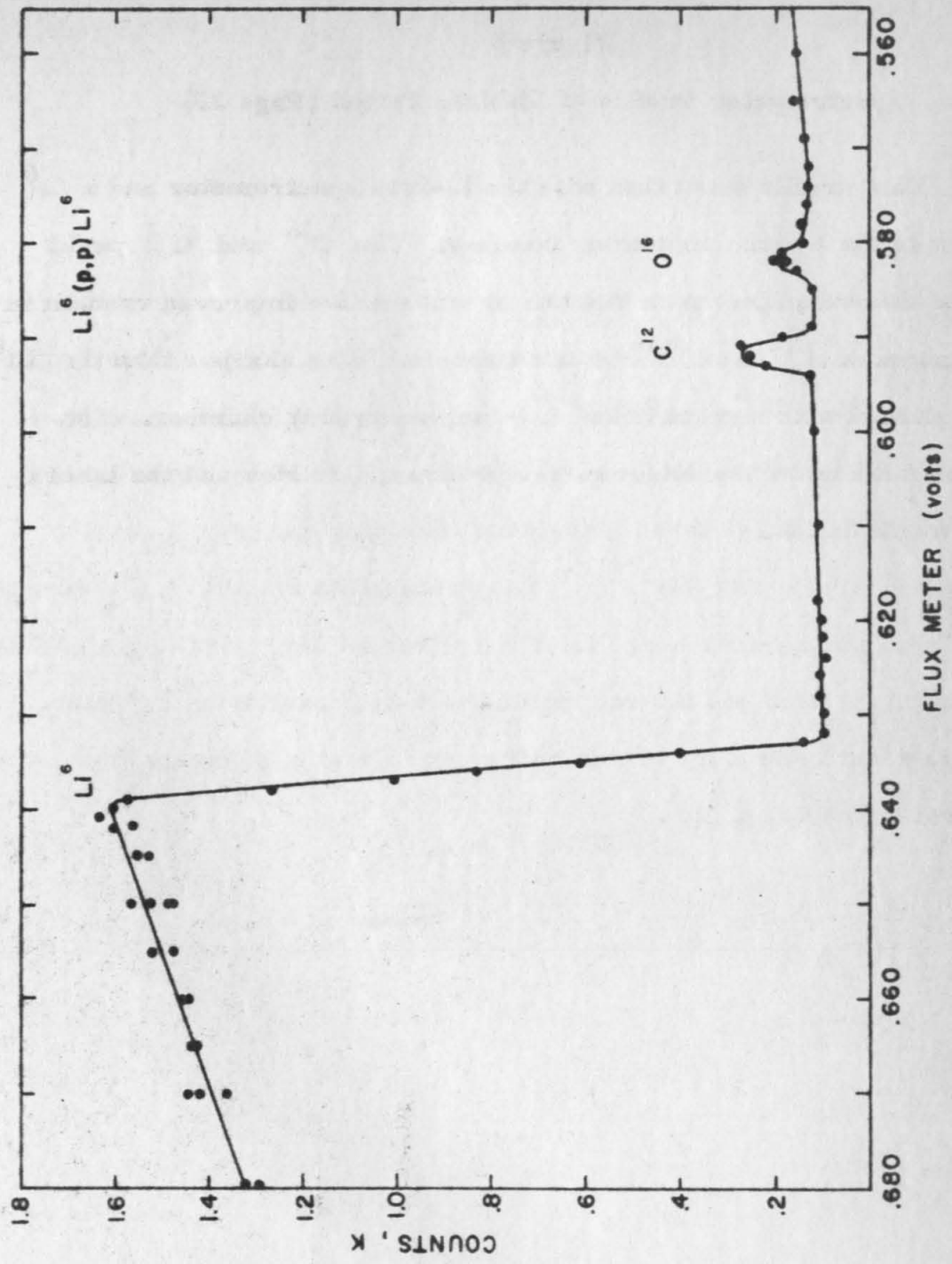
Li⁶(p,p)Li⁶
Li⁶
C¹² O¹⁶
COUNTS, K
FLUX METER (volts)
1.8
1.6
1.4
1.2
1.0
.8
.6
.4
.2
.680
.660
.640
.620
.600
.580
.560

Figure 6

Spectrometer Profile of Lithium Target (Page 24)

This profile was taken with the 16-inch spectrometer and a Li^6 target in the 6-inch scattering chamber. The solid dots represent the profile taken just after the target was made and show very little indication of C^{12} and O^{16} contamination. When a foil, which is thick enough to stop α^{++}'s and He^{3++}'s but not protons at this energy, is placed in front of the detector, the profile indicated by the crosses is found. This then is taken as evidence that the background consists mainly of α^{++}'s and He^{3++}'s. The profile represented by the circles was taken twenty-four hours later and gives an indication of the quality of the target used and the vacuum in the 6-inch scattering chamber. The incident laboratory proton energy was about 2.3 Mev and the laboratory angle $81^{\circ}\ 13'$.

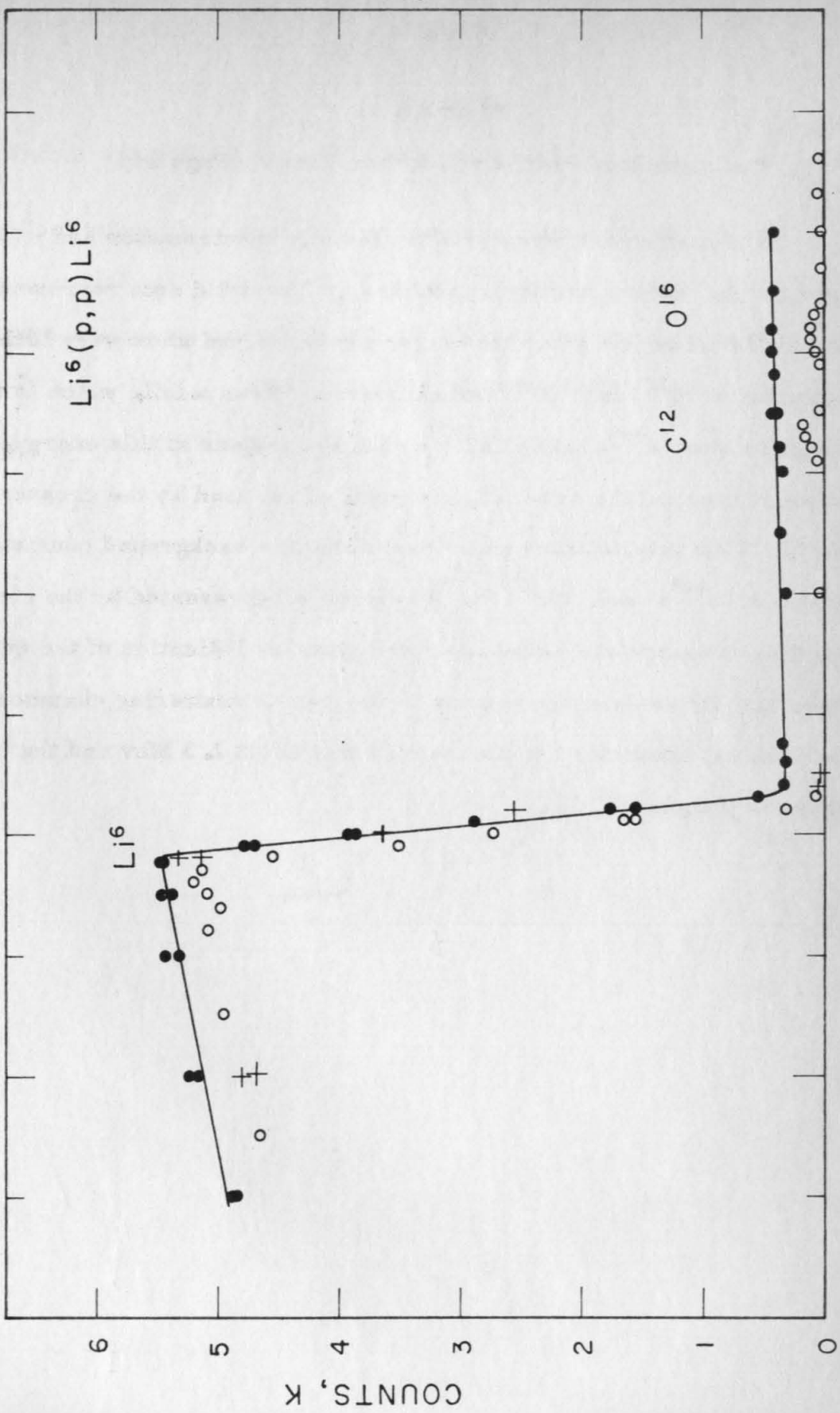
Li⁶(p,p)Li⁶
Li⁶
C¹²
O¹⁶
COUNTS, K
FLUXMETER (volts)
0
1
2
3
4
5
6
.420
.440
.460
.480
.500
.520

Figure 7

Resonant Gamma-ray Yield From the $F^{19}(p, \alpha\gamma)O^{16}$ Reaction (Page 15)

The 80^{o} electrostatic analyzer was calibrated by using the known 872.5 kev resonance in the $F^{19}(p, \alpha\gamma)O^{16}$ reaction. The dots represent the curve taken from left to right and the crosses represent the curve taken immediately afterwards from right to left.

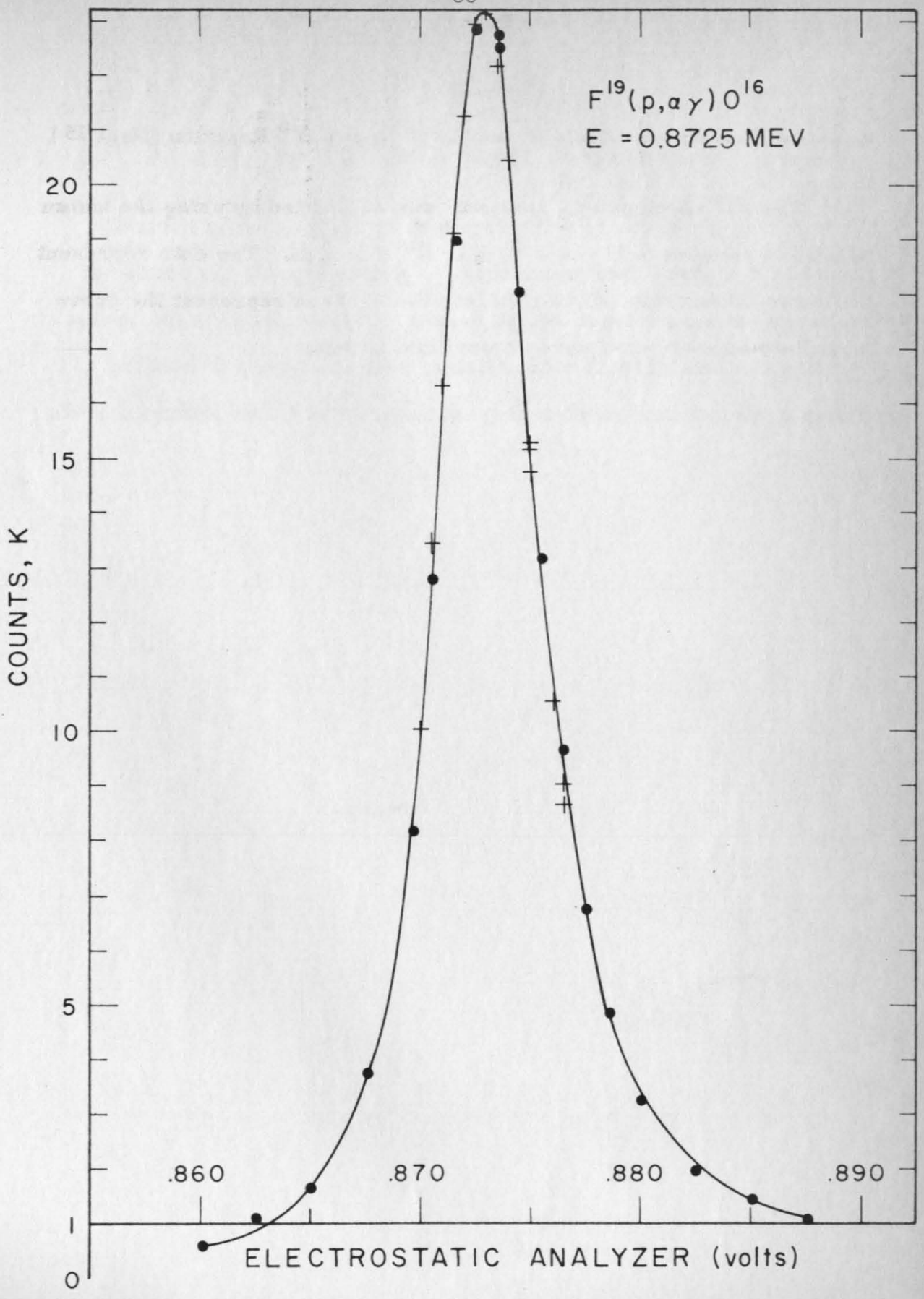
$F^{19}(p,\alpha\gamma)O^{16}$
E = 0.8725 MEV
COUNTS, K
20
15
10
5
1
0
.860
.870
.880
.890
ELECTROSTATIC ANALYZER (volts)

Figure 8

Neutron Threshold for the Reaction $Li^7(p, n)Be^7$ (Page 16)

In this graph the two-thirds power of the number of neutrons counted for a given charge collected is plotted against the setting of the electrostatic analyzer potentiometer. The analyzer is calibrated by using the straight line extrapolation near the threshold and the well-established threshold energy of 1880.7 ± 0.4 kev (Marion, 1961).

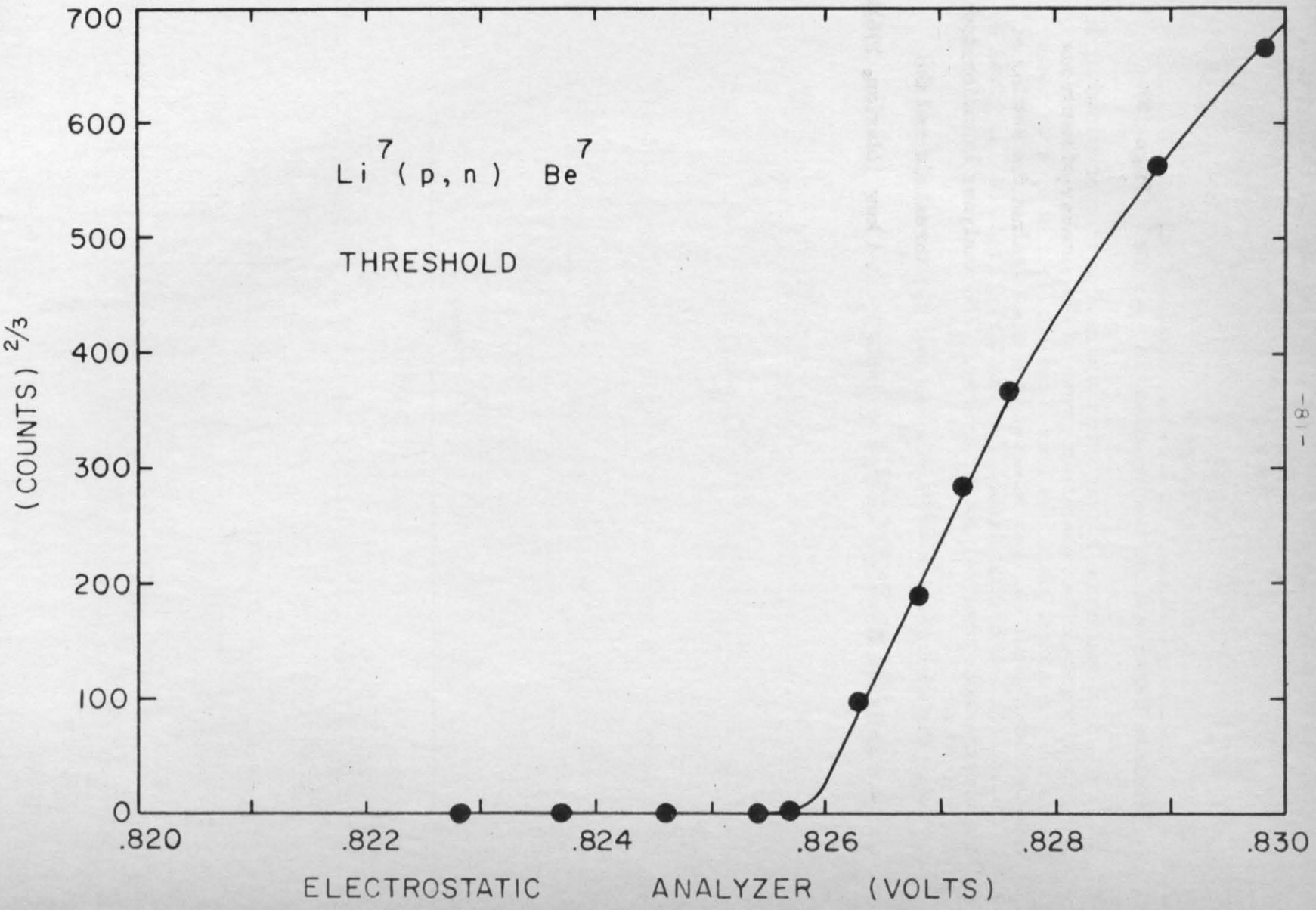
700
600
500
400
300
200
100
0
(COUNTS) 2/3
Li 7 (p, n) Be 7
THRESHOLD
.820
.822
.824
.826
.828
.830
ELECTROSTATIC ANALYZER (VOLTS)

Figure 9

Scattering Geometry of 2.5-inch Chamber (Page 10)

The incident beam comes into the chamber at approximately 10^{o} above the horizontal plane and leaves the chamber at approximately 10^{o} below the horizontal plane. The scattering angle θ_L is given by the relation

$$\sin \frac{\theta_L}{2} = \cos \alpha \sin \frac{\theta_H}{2}$$

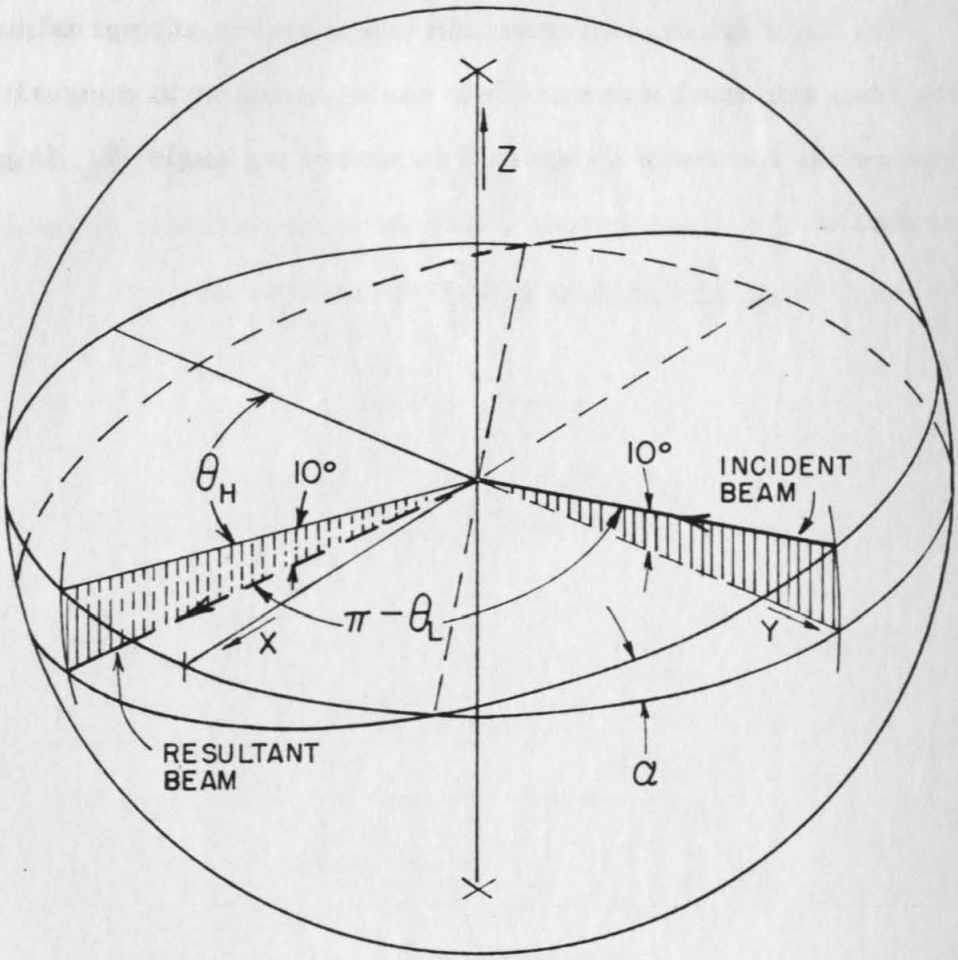

GEOMETRY OF THE SCATTERING PROCESS ILLUSTRATING THE RELATIONSHIP OF THE HORIZONTAL PLANE AND THE BEAM PLANE

Figure 10

The 6-inch Target Chamber and Furnace (Page 20)

This drawing illustrates the relative positions of the scattering chamber and furnace. This arrangement with the cold trap separating the two regions was found to be a very satisfactory way of obtaining a clean copper calibration target and a lithium target in the scattering chamber at the same time.

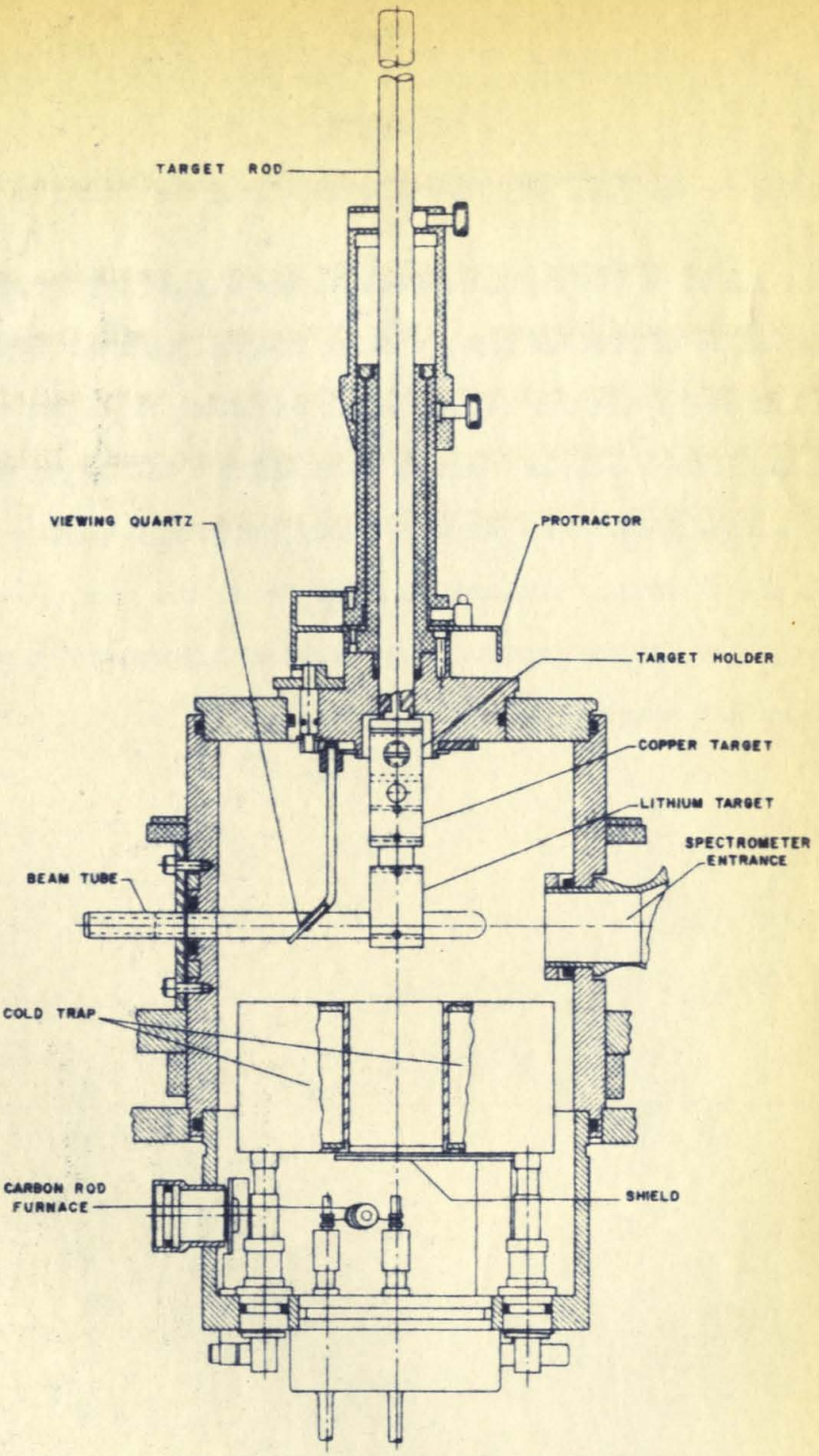
TARGET ROD
VIEWING QUARTZ
PROTRACTOR
TARGET HOLDER
COPPER TARGET
LITHIUM TARGET
SPECTROMETER ENTRANCE
BEAM TUBE
COLD TRAP
CARBON ROD FURNACE
SHIELD

Figure 11

Stopping Power Measurement Spectrometer Profile (Page 21)

The curve on the right represents the copper edge resulting from the scattering of protons from a clean copper surface. The two curves on the left represent the copper edges resulting from the scattering of protons from a copper surface upon which a thin layer of lithium has been deposited. The displacements between the latter two edges and the clean surface copper edge are due to the energy loss of the protons in the lithium layer. The incident laboratory proton energy was about 2.0 Mev and the laboratory angle $90^{\circ}\,44'$.

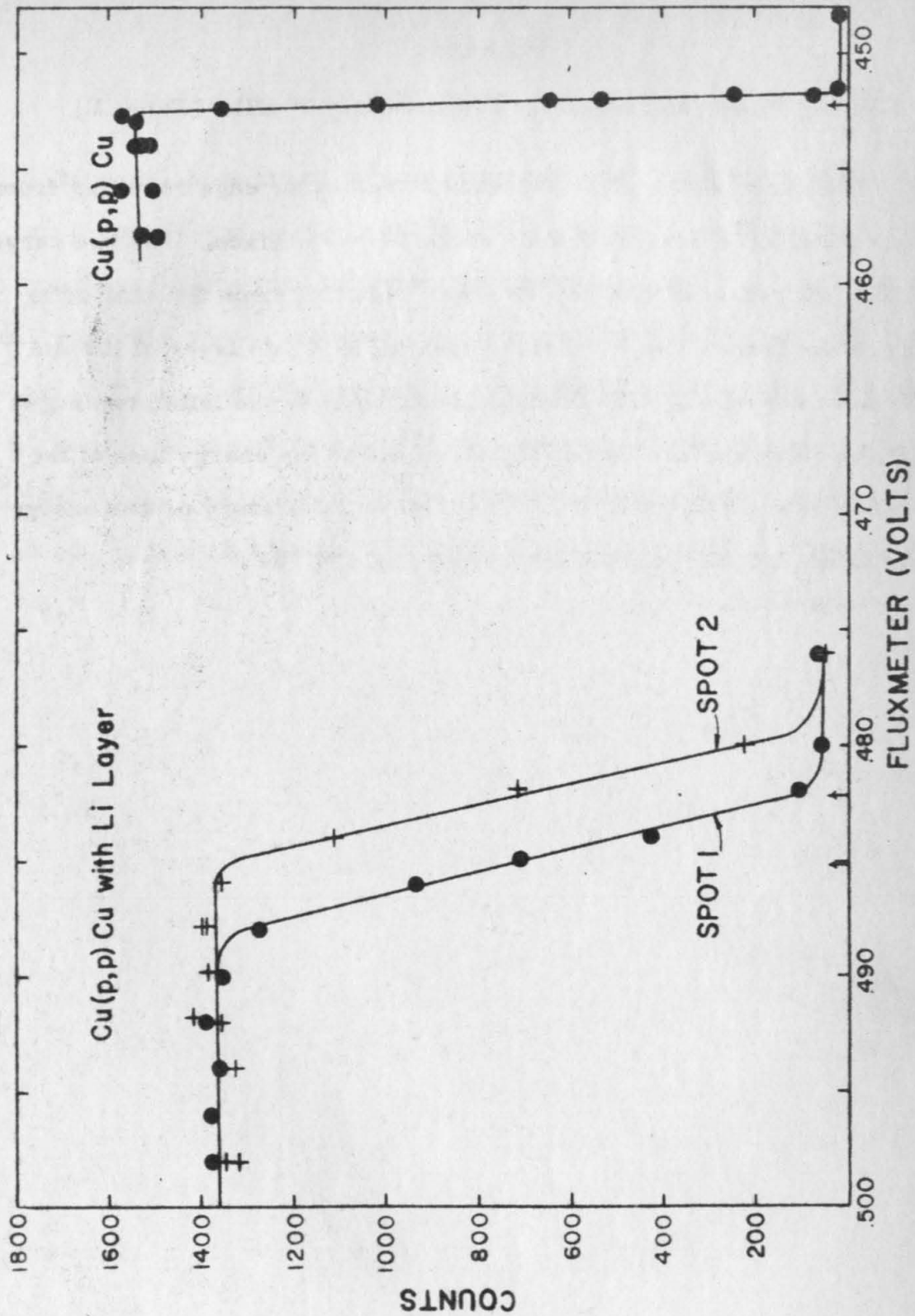
Cu(p,p) Cu with Li Layer
Cu(p,p) Cu
SPOT 2
SPOT 1
COUNTS
FLUXMETER (VOLTS)
1800
1600
1400
1200
1000
800
600
400
200
.500
.490
.480
.470
.460
.450

Figure 12

Atomic Stopping Cross Section for Protons in Li (Page 24)

The solid points are measurements of Bader et al., (Bader, 1956) and Warters et al. (Warters, 1953) of the stopping cross section for protons in Li. The solid points with vertical bars are determined from the α-particle measurements of Rosenblum, (Rosenblum, 1928). The solid curve is the Bloch curve as derived by Whaling, (Whaling, 1958). Relative stopping power measurements made in this experiment are indicated by the crosses and triangles and show that indeed the Bloch curve applies to lithium as well as to all of the other elements (Whaling, 1958).

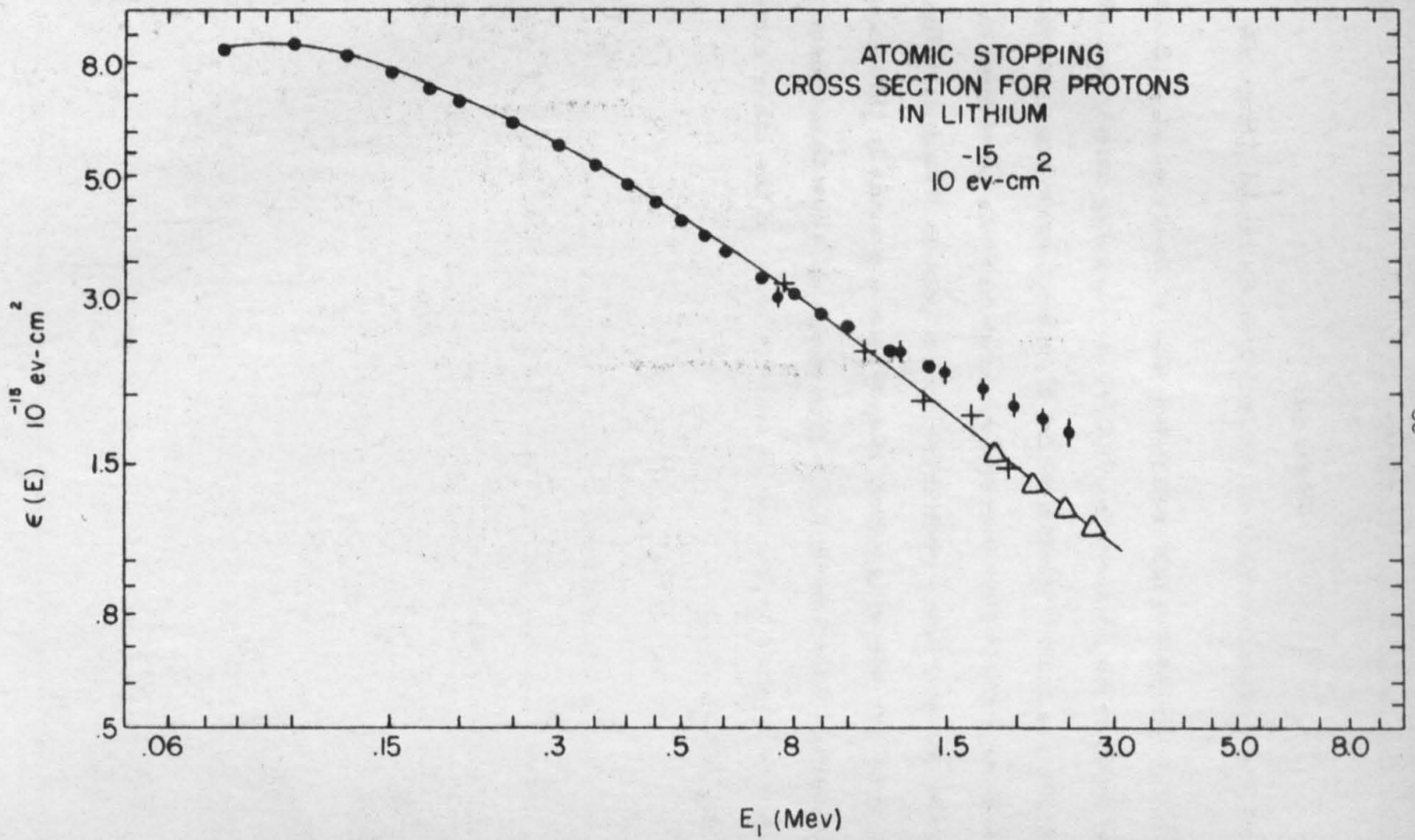
ATOMIC STOPPING
CROSS SECTION FOR PROTONS
IN LITHIUM
10^-15 ev-cm^2
ε (E) 10^-15 ev-cm^2
8.0
5.0
3.0
1.5
.8
.5
.06
.15
.3
.5
.8
1.5
3.0
5.0
8.0
E1 (Mev)

Figure 13

Dead Time Measurement of Scintillation Counter (Page 26)

In this graph the difference between the true number of counts and the number of counts recorded for a given charge collected is plotted against the reciprocal of the time necessary for collection. The counting rate is then varied by increasing the beam current of protons which are being scattered from a copper target. An estimate for the true number of counts is found by counting at a very low counting rate. The dead time is then given approximately by the formula

$$\rho = \frac{\text{slope}}{N^2}$$

where N is the estimate for the true number of counts and the slope of this curve is used. Here $N = 1.828 \times 10^5$ counts and the dead time was found to be $\rho = 10$ μsec.

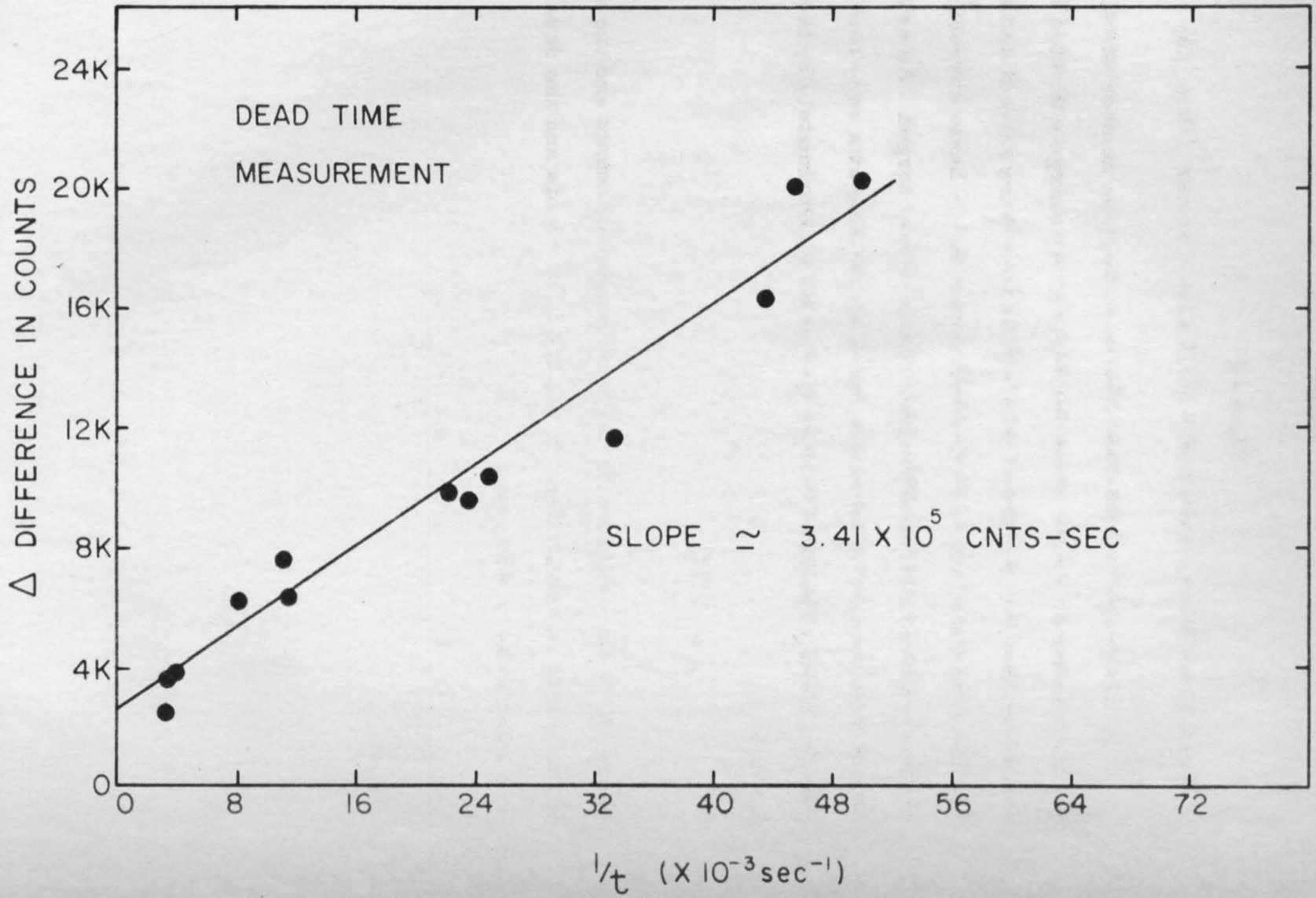
DEAD TIME
MEASUREMENT
SLOPE ≃ 3.41 X 10^5 CNTS-SEC
Δ DIFFERENCE IN COUNTS
24K
20K
16K
12K
8K
4K
0
0
8
16
24
32
40
48
56
64
72
1/t (X 10^-3 sec^-1)

Figure 14

Excitation Function for $Li^6(p, p)Li^6$ (Page 27)

The ratio of the measured elastic scattering cross section to the cross section for Rutherford scattering from a point charge is plotted as a function of laboratory proton energy (in Mev) for three C. M. angles corresponding approximately to the zeros of the first and second Legendre polynomials and the farthest back angle obtainable. The crosses indicate data taken on the 2-Mev machine and the dots indicate data resulting from measurements on the 3-Mev machine.

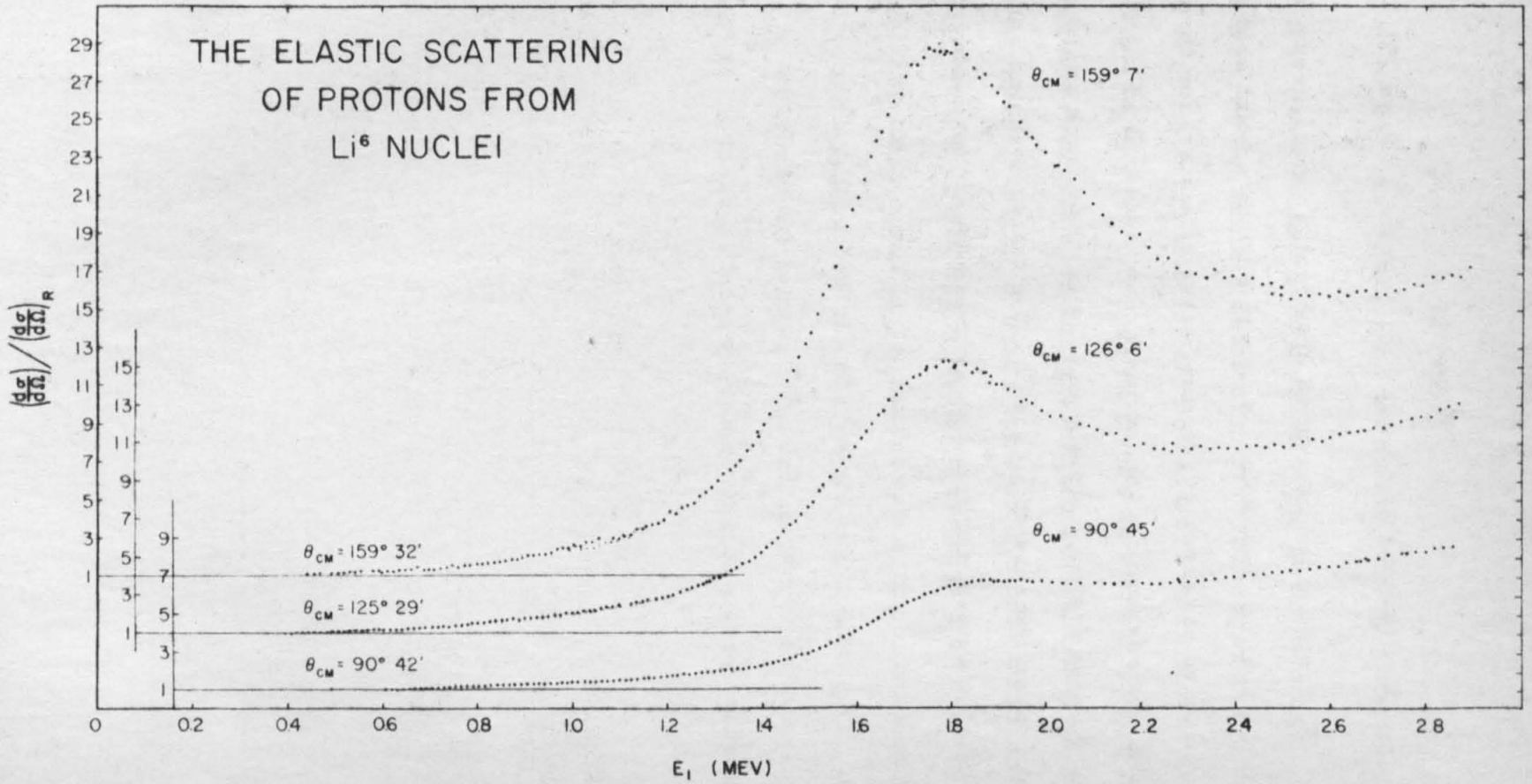
THE ELASTIC SCATTERING
OF PROTONS FROM
Li⁶ NUCLEI
θ_{CM} = 159° 7'
θ_{CM} = 126° 6'
θ_{CM} = 90° 45'
θ_{CM} = 159° 32'
θ_{CM} = 125° 29'
θ_{CM} = 90° 42'
$\left(\frac{d\sigma}{d\Omega}\right) / \left(\frac{d\sigma}{d\Omega}\right)_R$
E_1 (MEV)

Figure 15

Scattering Cross Section for $Li^6(p, p)Li^6$ at $\theta_{CM} = 90^o$ (Page 27)

The measured cross section is indicated by the solid dots. The solid curve represents the calculated Rutherford cross section. The curve indicated by the open circles is that calculated for a $5/2^-$ p-wave resonant state as shown on page 27. The curve indicated by crosses is the sum of the Rutherford cross section and the cross section due to the $5/2^-$ p-wave resonant state. The triangles represent the s-wave scattering cross section calculated from the s-wave scattering amplitudes which were determined in the scattering analysis of the data. The solid curve through the experimental points is the sum of the s-wave background, the $5/2^-$ p-wave resonant state, and the Rutherford cross section; and represents a theoretical fit to the data.

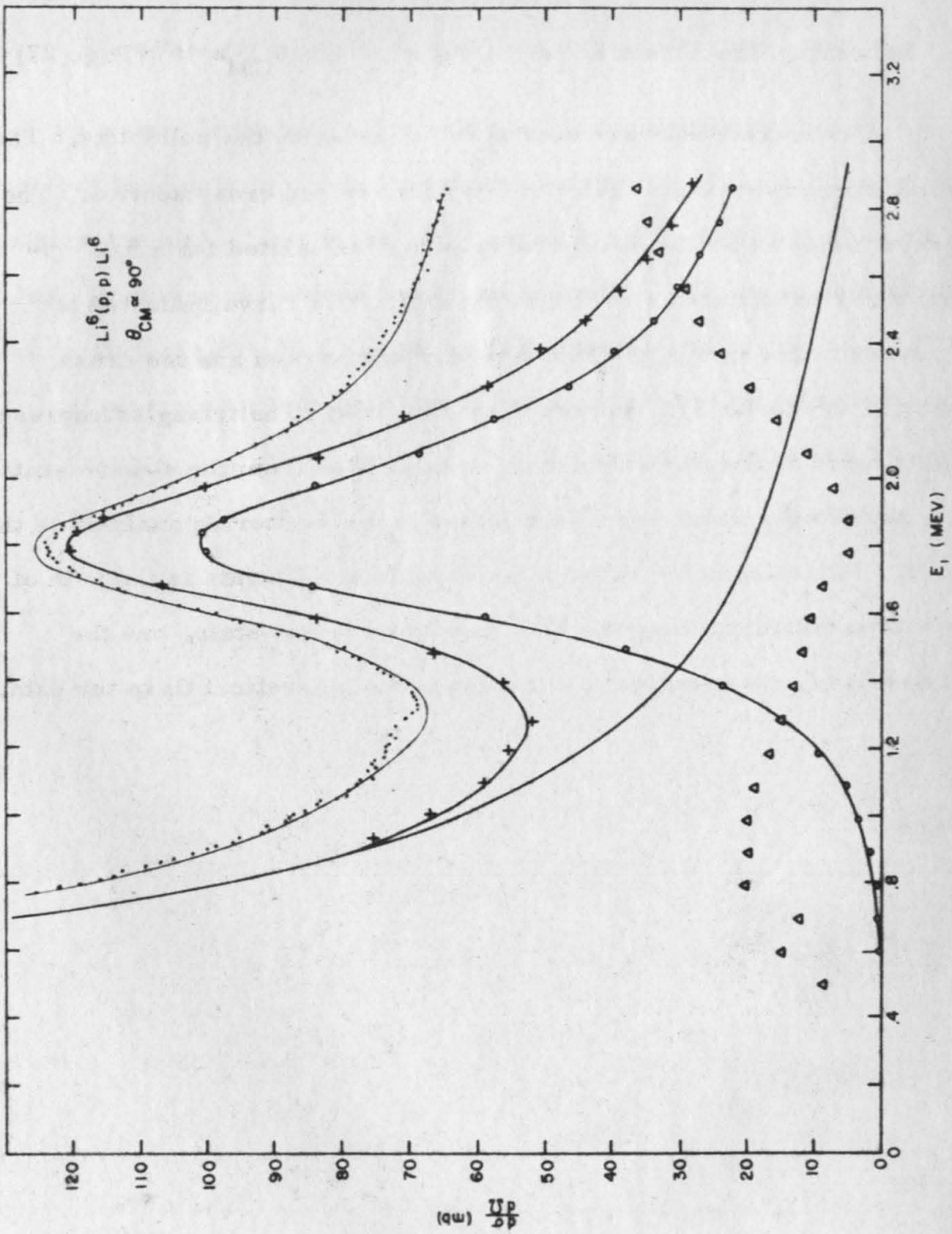
$Li^6(p,p)Li^6$
$\theta_{CM} \approx 90°$
$\frac{d\sigma}{d\Omega}$ (mb)
E_1 (MEV)
0
10
20
30
40
50
60
70
80
90
100
110
120
.4
.8
1.2
1.6
2.0
2.4
2.8
3.2

Figures 16 to 40

Angular Distributions for $Li^6(p, p)Li^6$ Scattering (Page 28)

In the following figures the ratio of the measured scattering cross section to the calculated Rutherford cross section is plotted as a function of center of mass angle. The error marks indicate relative uncertainties and are 3% for the backward angles and 4% for 90° and 70°. The curves are calculated from equation 97 using the values of the scattering amplitudes deduced from the analysis and given in table 3 and shown in figure 48.

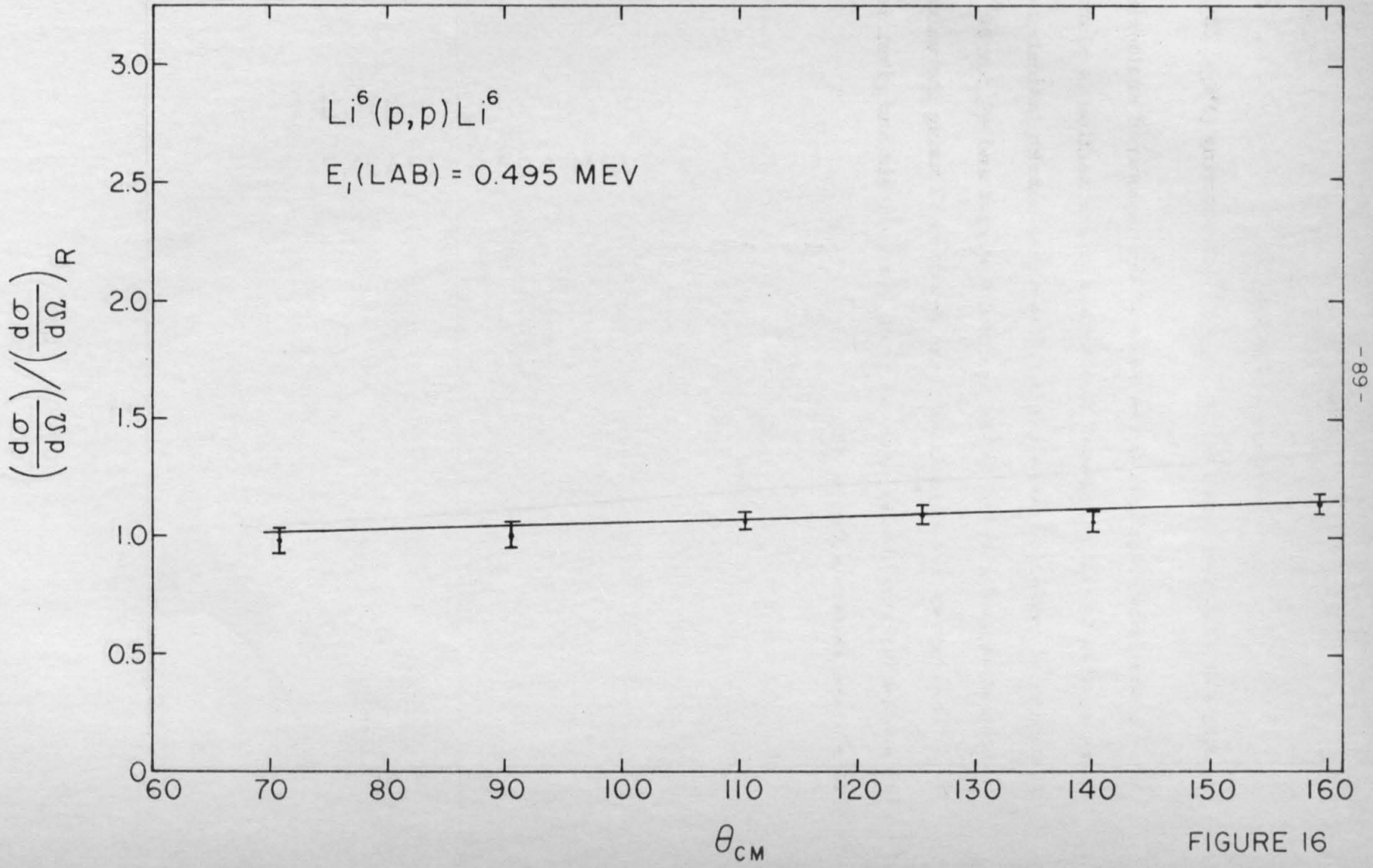
$Li^6(p,p)Li^6$
E_l(LAB) = 0.495 MEV
$\left(\frac{d\sigma}{d\Omega}\right)/\left(\frac{d\sigma}{d\Omega}\right)_R$
3.0
2.5
2.0
1.5
1.0
0.5
0
60
70
80
90
100
110
120
130
140
150
160
θ_{CM}

FIGURE 16

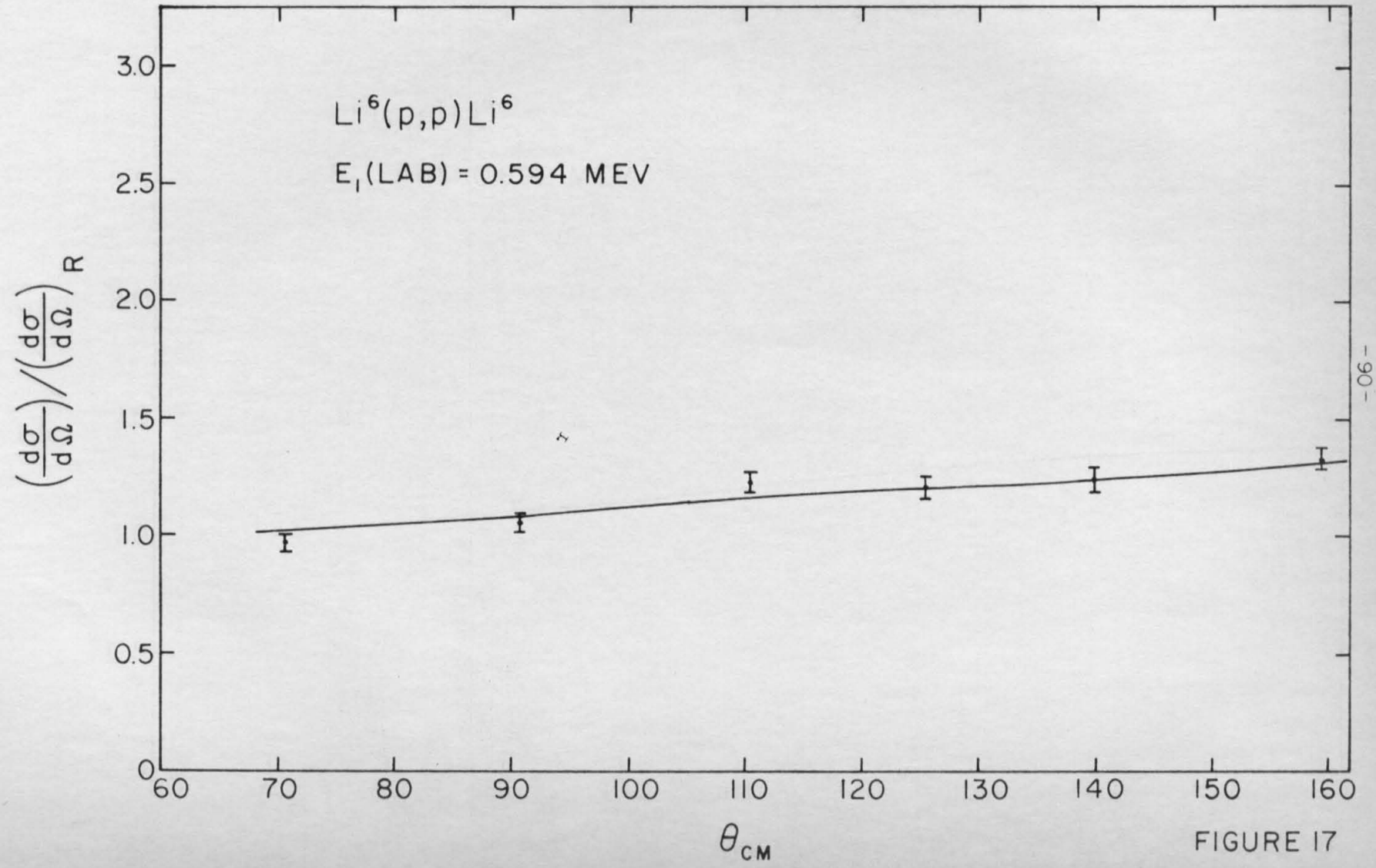
Li⁶(p,p)Li⁶
E₁(LAB) = 0.594 MEV
(dσ/dΩ)/(dσ/dΩ)R
θCM
3.0
2.5
2.0
1.5
1.0
0.5
0
60
70
80
90
100
110
120
130
140
150
160

FIGURE 17

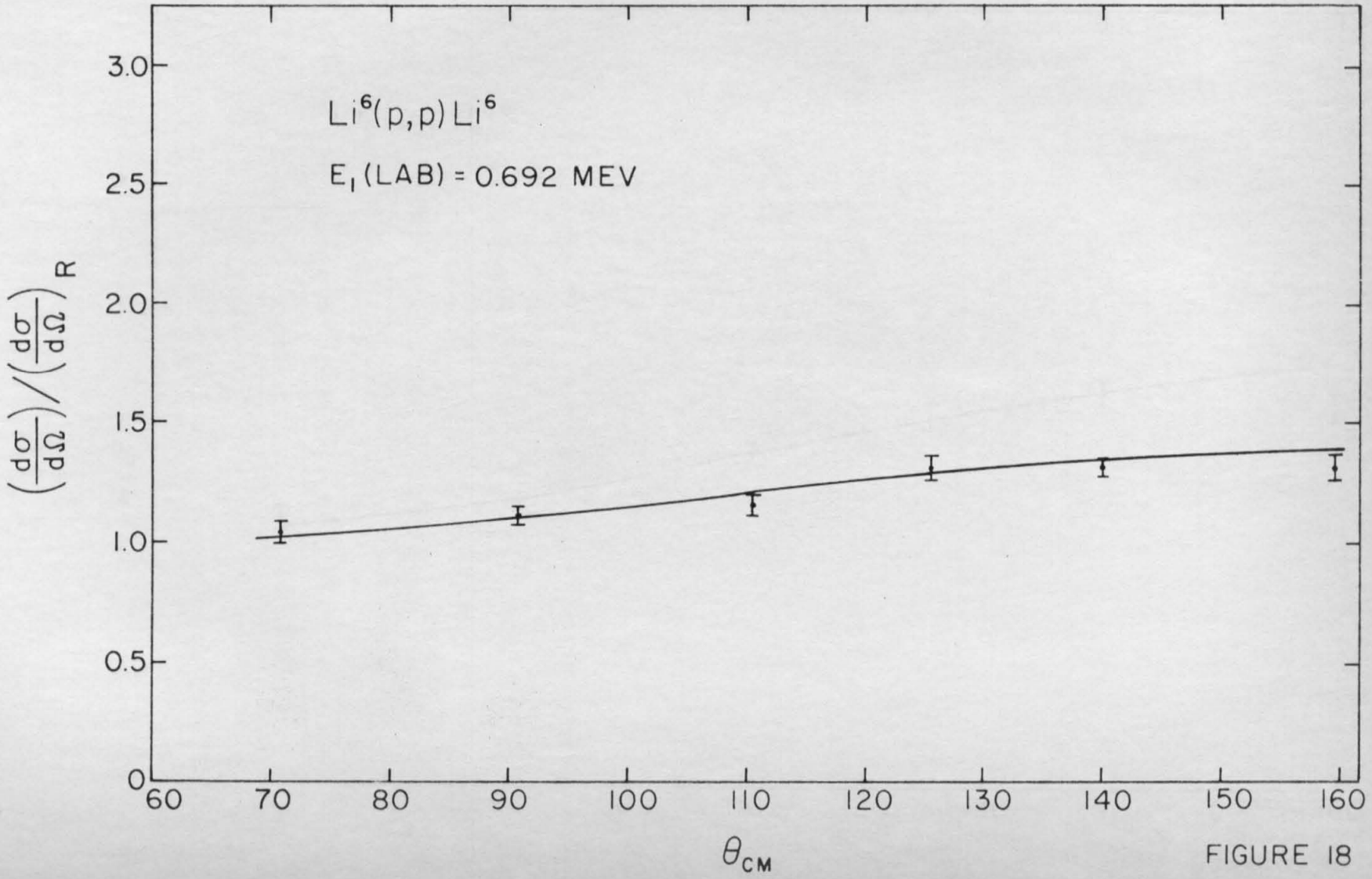
$Li^6(p,p)Li^6$
E_1(LAB) = 0.692 MEV
$\left(\frac{d\sigma}{d\Omega}\right)/\left(\frac{d\sigma}{d\Omega}\right)_R$
3.0
2.5
2.0
1.5
1.0
0.5
0
60
70
80
90
100
110
120
130
140
150
160
θ_{CM}

FIGURE 18

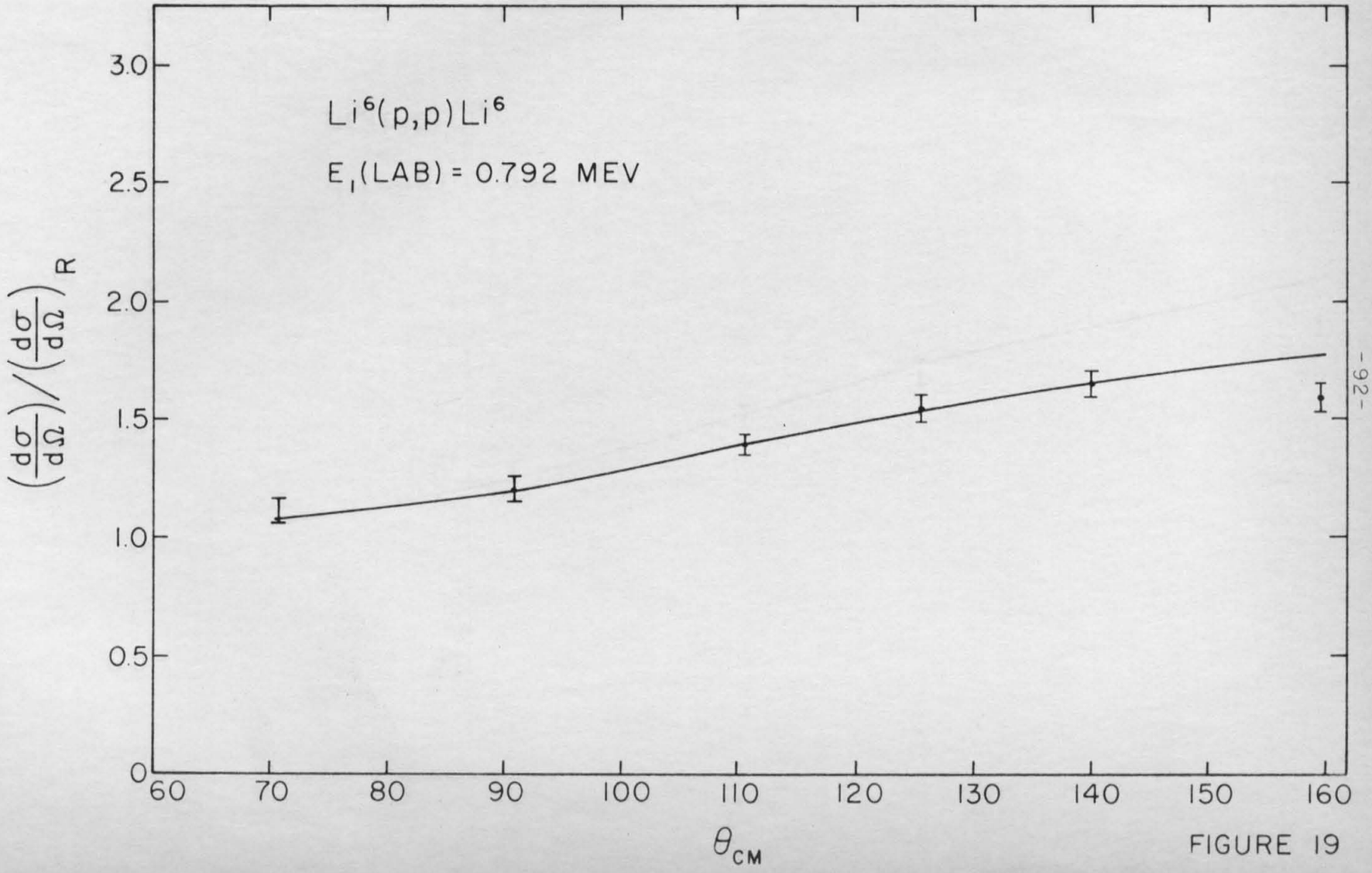
$Li^6(p,p)Li^6$
E_1(LAB) = 0.792 MEV
$\left(\frac{d\sigma}{d\Omega}\right)/\left(\frac{d\sigma}{d\Omega}\right)_R$
θ_{CM}
0
0.5
1.0
1.5
2.0
2.5
3.0
60
70
80
90
100
110
120
130
140
150
160

FIGURE 19

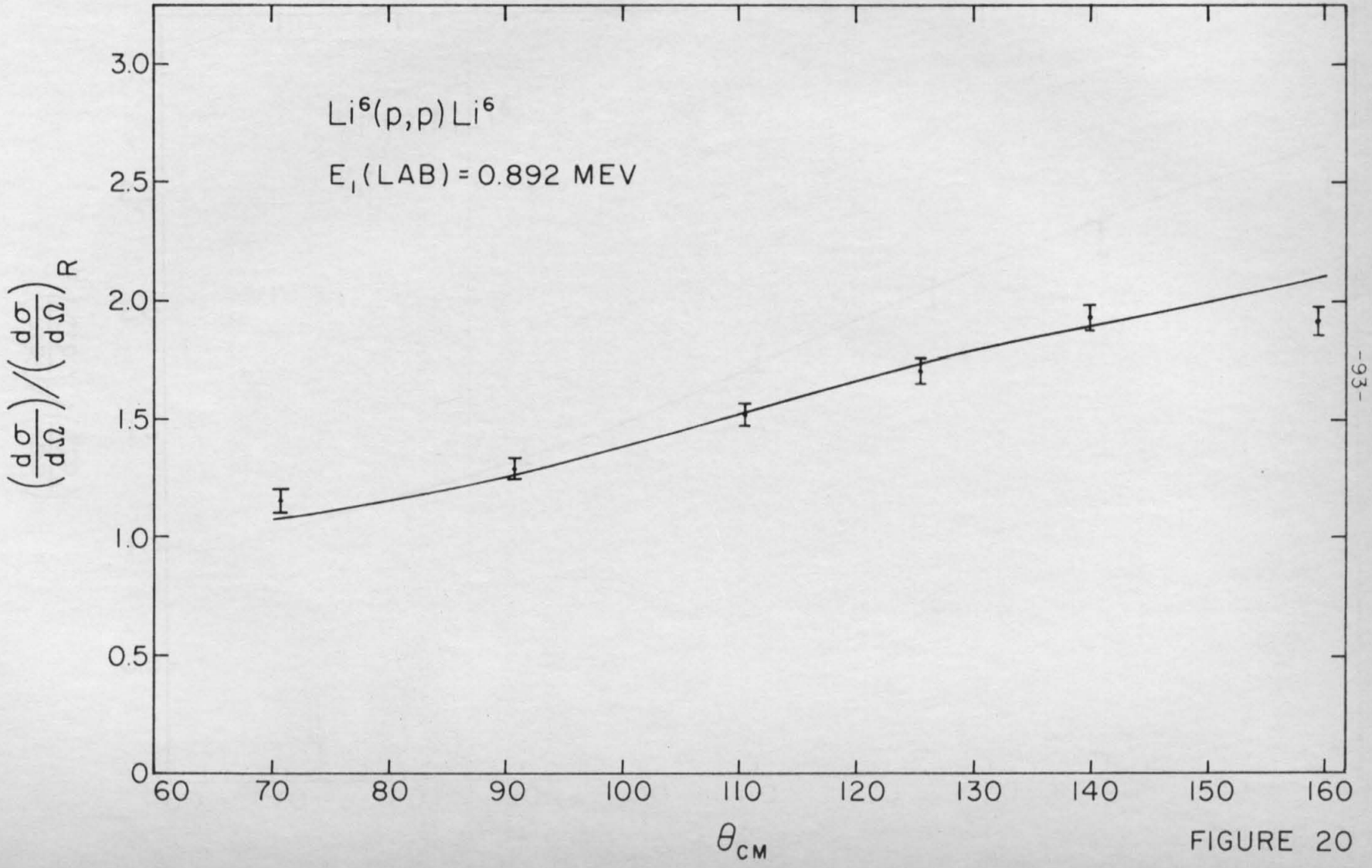
$Li^6(p,p)Li^6$
E_1(LAB) = 0.892 MEV
$\left(\frac{d\sigma}{d\Omega}\right)/\left(\frac{d\sigma}{d\Omega}\right)_R$
θ_{CM}
0
0.5
1.0
1.5
2.0
2.5
3.0
60
70
80
90
100
110
120
130
140
150
160

FIGURE 20

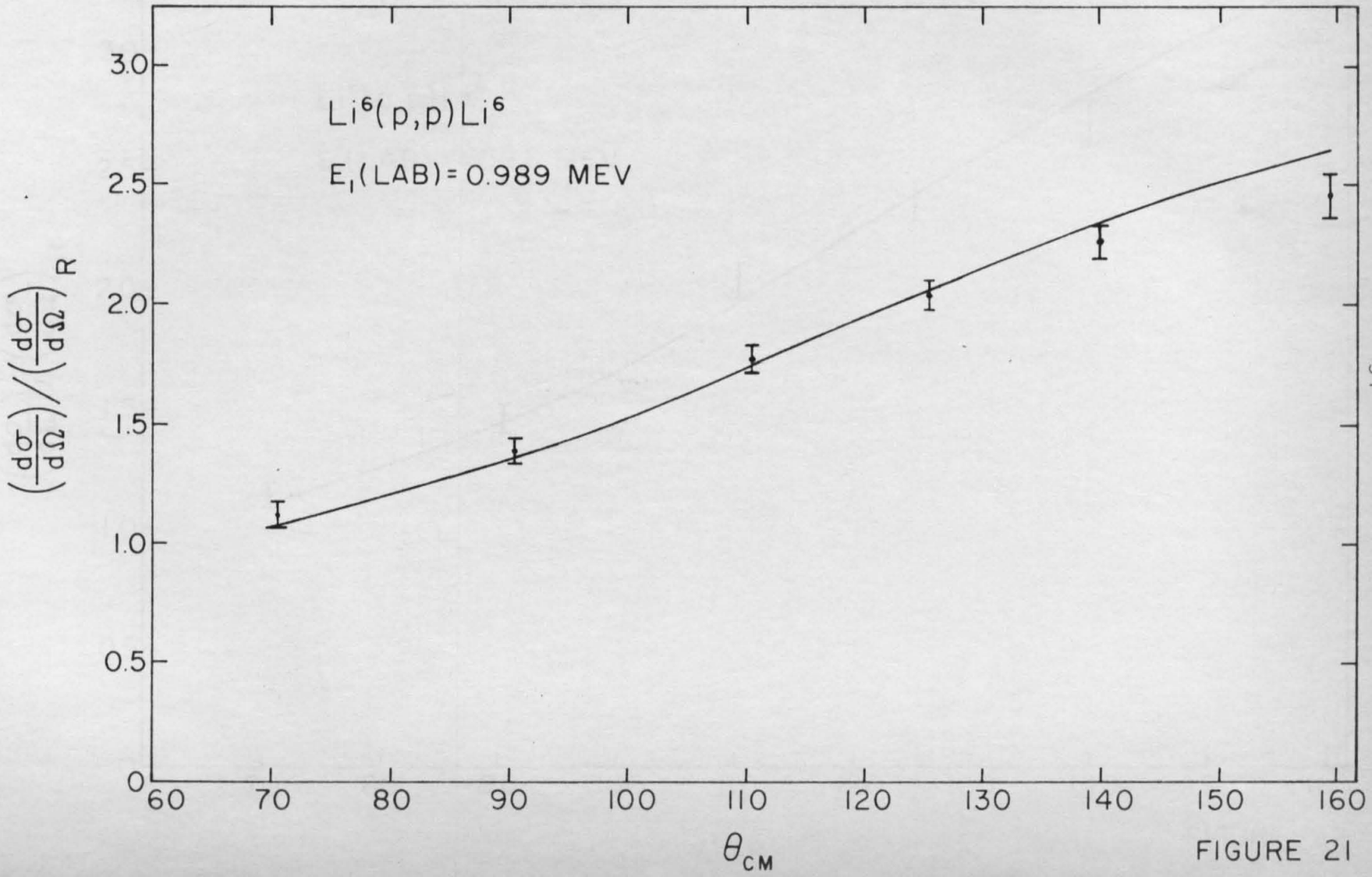
$Li^6(p,p)Li^6$
E_1(LAB) = 0.989 MEV
$\left(\frac{d\sigma}{d\Omega}\right)/\left(\frac{d\sigma}{d\Omega}\right)_R$
θ_{CM}
0
0.5
1.0
1.5
2.0
2.5
3.0
60
70
80
90
100
110
120
130
140
150
160

FIGURE 21

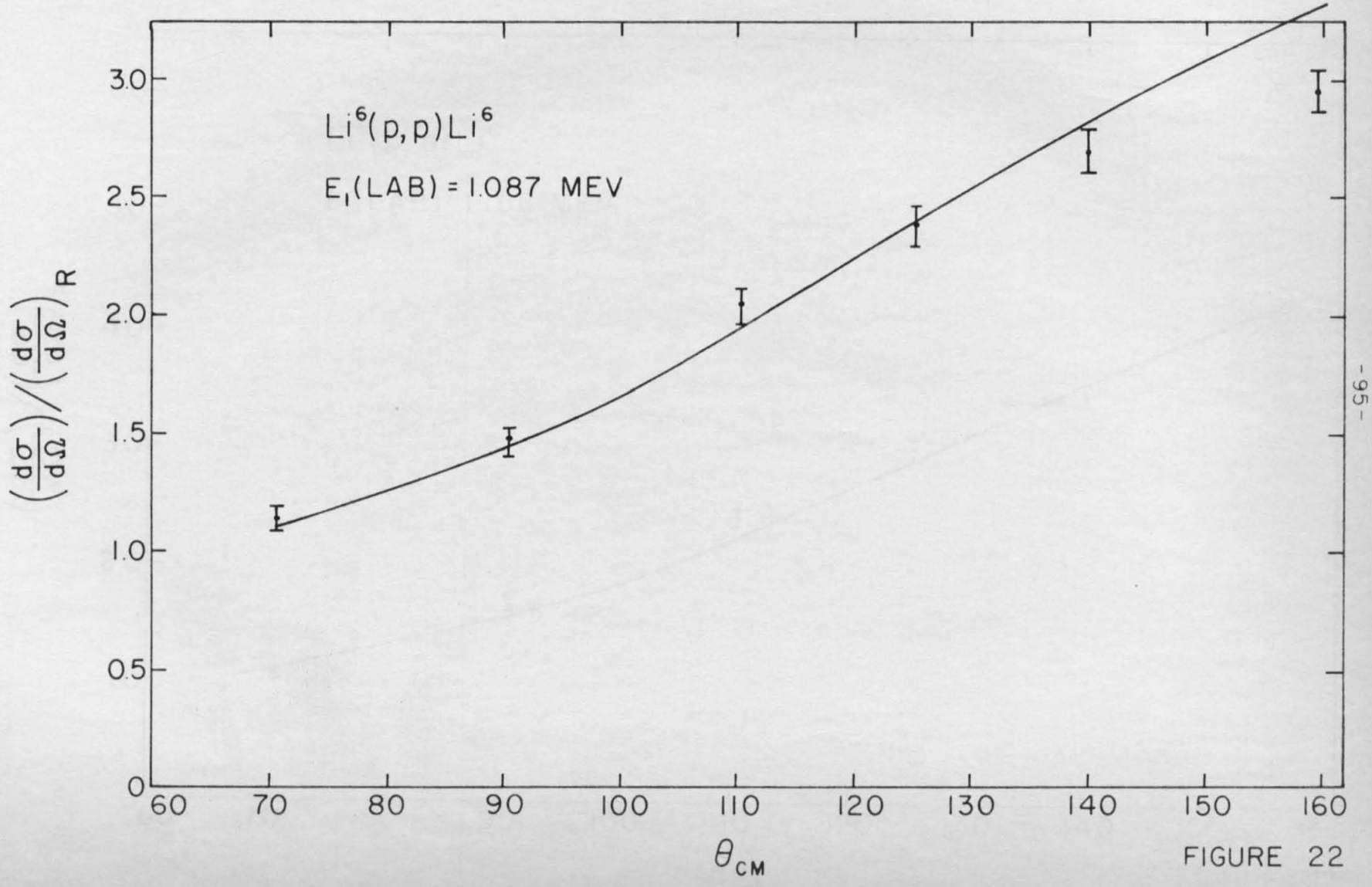
$Li^6(p,p)Li^6$
E_1(LAB) = 1.087 MEV
$\left(\frac{d\sigma}{d\Omega}\right)/\left(\frac{d\sigma}{d\Omega}\right)_R$
θ_{CM}
0
0.5
1.0
1.5
2.0
2.5
3.0
60
70
80
90
100
110
120
130
140
150
160

FIGURE 22

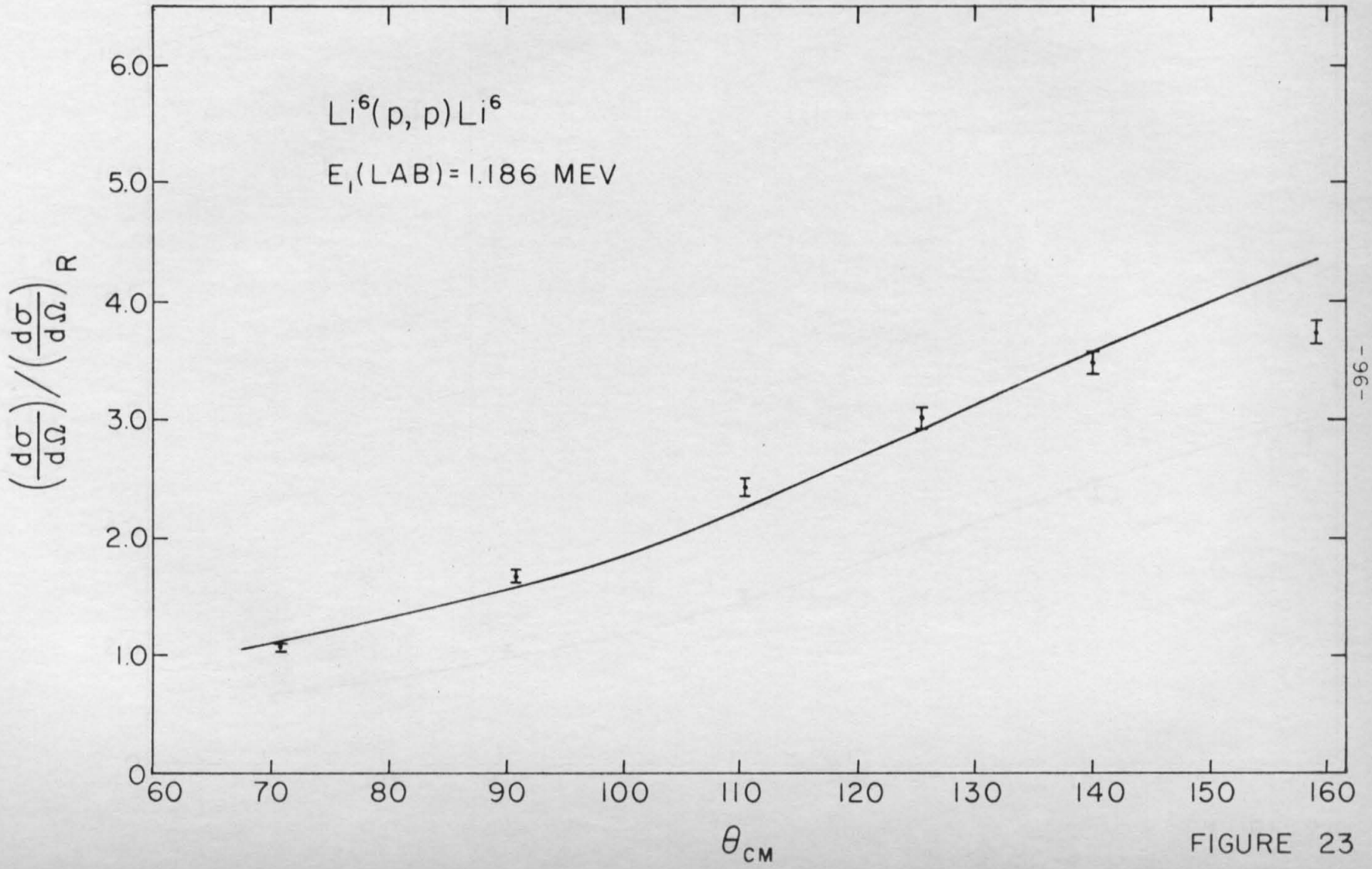
$Li^6(p, p)Li^6$
E_1(LAB) = 1.186 MEV
$\left(\frac{d\sigma}{d\Omega}\right)/\left(\frac{d\sigma}{d\Omega}\right)_R$
θ_{CM}
0
1.0
2.0
3.0
4.0
5.0
6.0
60
70
80
90
100
110
120
130
140
150
160

FIGURE 23

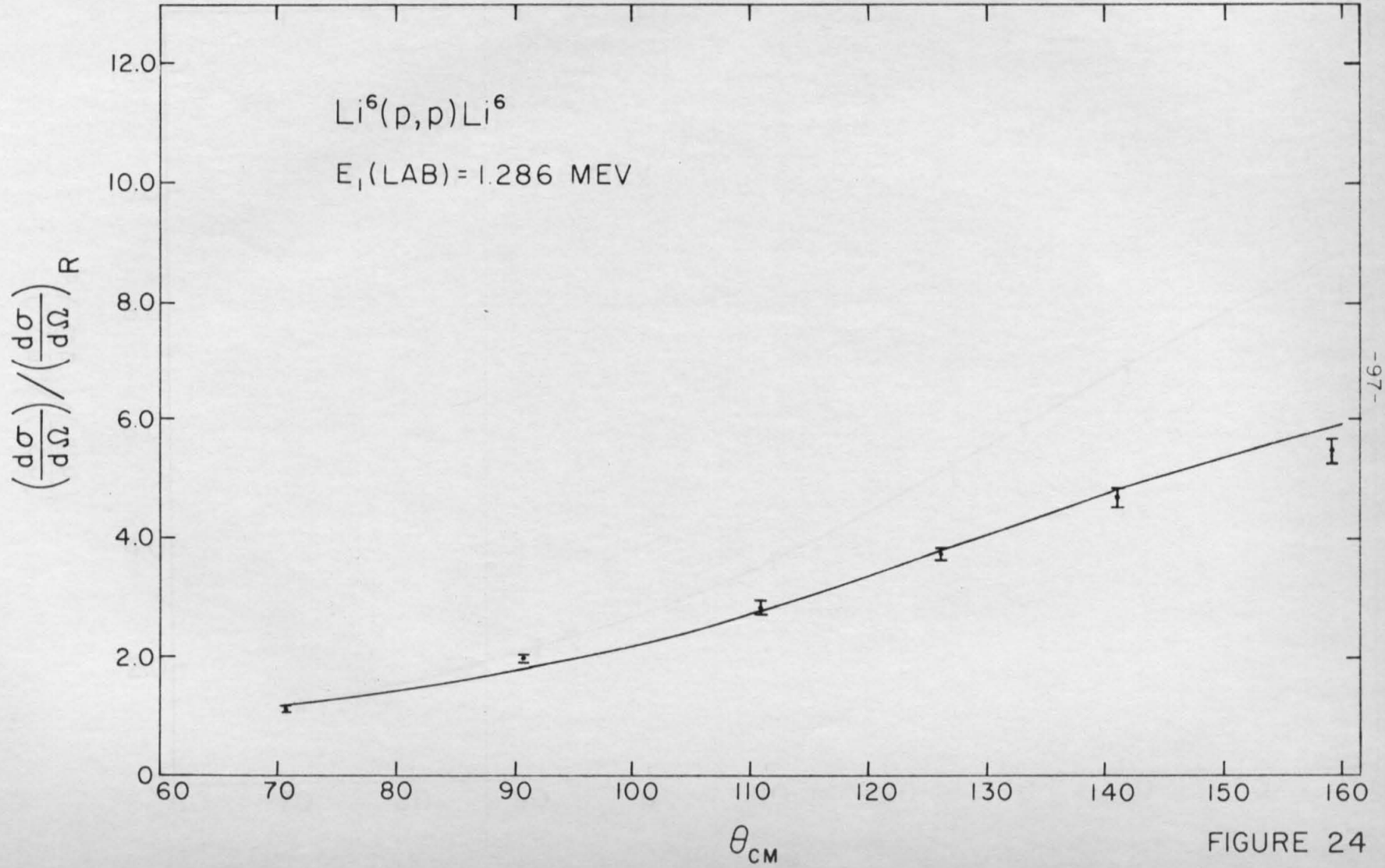
$Li^6(p,p)Li^6$
E_1(LAB) = 1.286 MEV
$\left(\frac{d\sigma}{d\Omega}\right)/\left(\frac{d\sigma}{d\Omega}\right)_R$
θ_{CM}
0
2.0
4.0
6.0
8.0
10.0
12.0
60
70
80
90
100
110
120
130
140
150
160

FIGURE 24

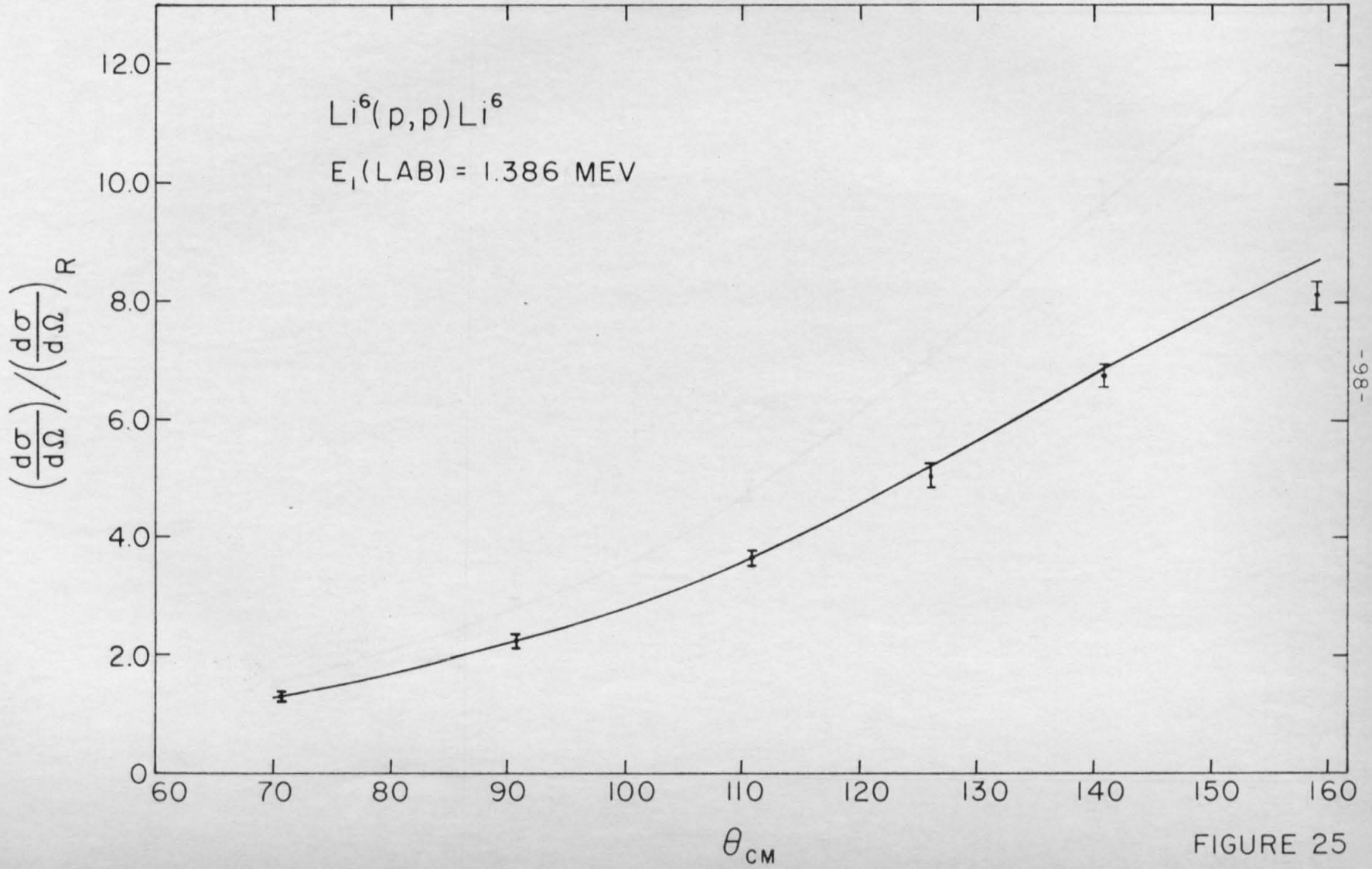
$Li^6(p,p)Li^6$
E_1(LAB) = 1.386 MEV
$\left(\frac{d\sigma}{d\Omega}\right)/\left(\frac{d\sigma}{d\Omega}\right)_R$
θ_{CM}
0
2.0
4.0
6.0
8.0
10.0
12.0
60
70
80
90
100
110
120
130
140
150
160

FIGURE 25

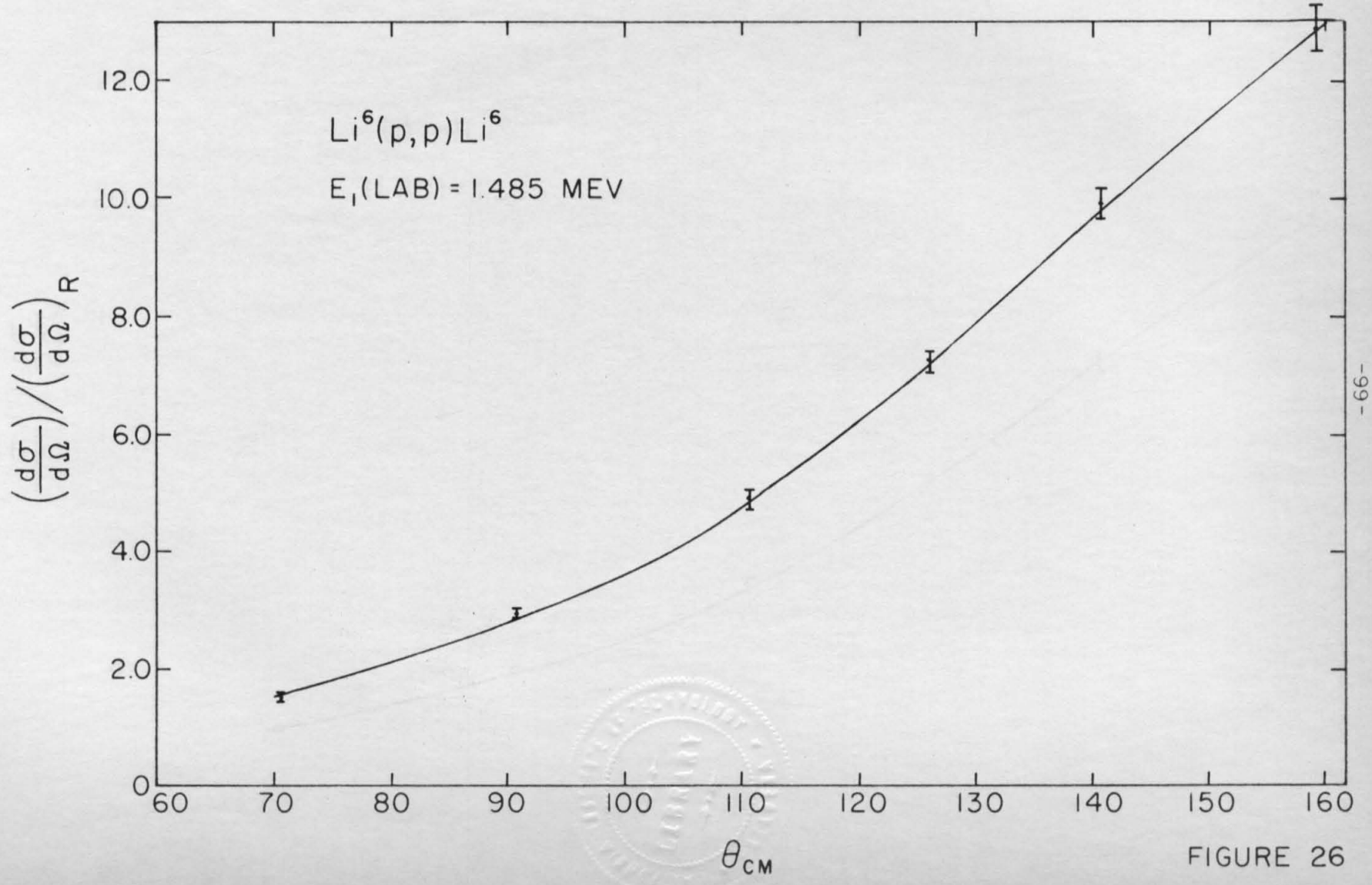
$Li^6(p,p)Li^6$
E_1(LAB) = 1.485 MEV
$\left(\frac{d\sigma}{d\Omega}\right)/\left(\frac{d\sigma}{d\Omega}\right)_R$
12.0
10.0
8.0
6.0
4.0
2.0
0
60
70
80
90
100
110
120
130
140
150
160
θ_{CM}

FIGURE 26

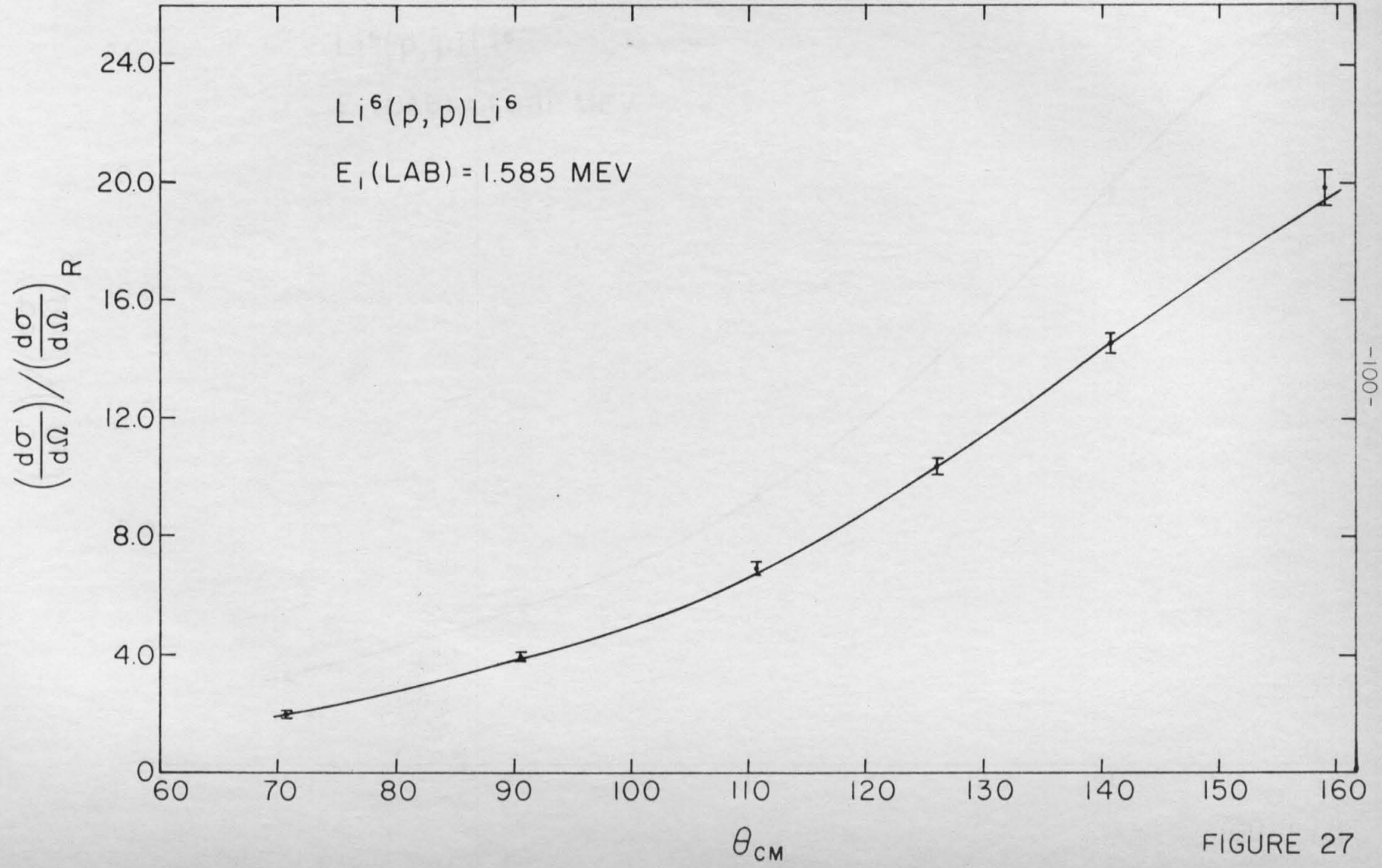
$Li^6(p, p)Li^6$
E_1(LAB) = 1.585 MEV
$\left(\frac{d\sigma}{d\Omega}\right)/\left(\frac{d\sigma}{d\Omega}\right)_R$
24.0
20.0
16.0
12.0
8.0
4.0
0
60
70
80
90
100
110
120
130
140
150
160
θ_{CM}

FIGURE 27

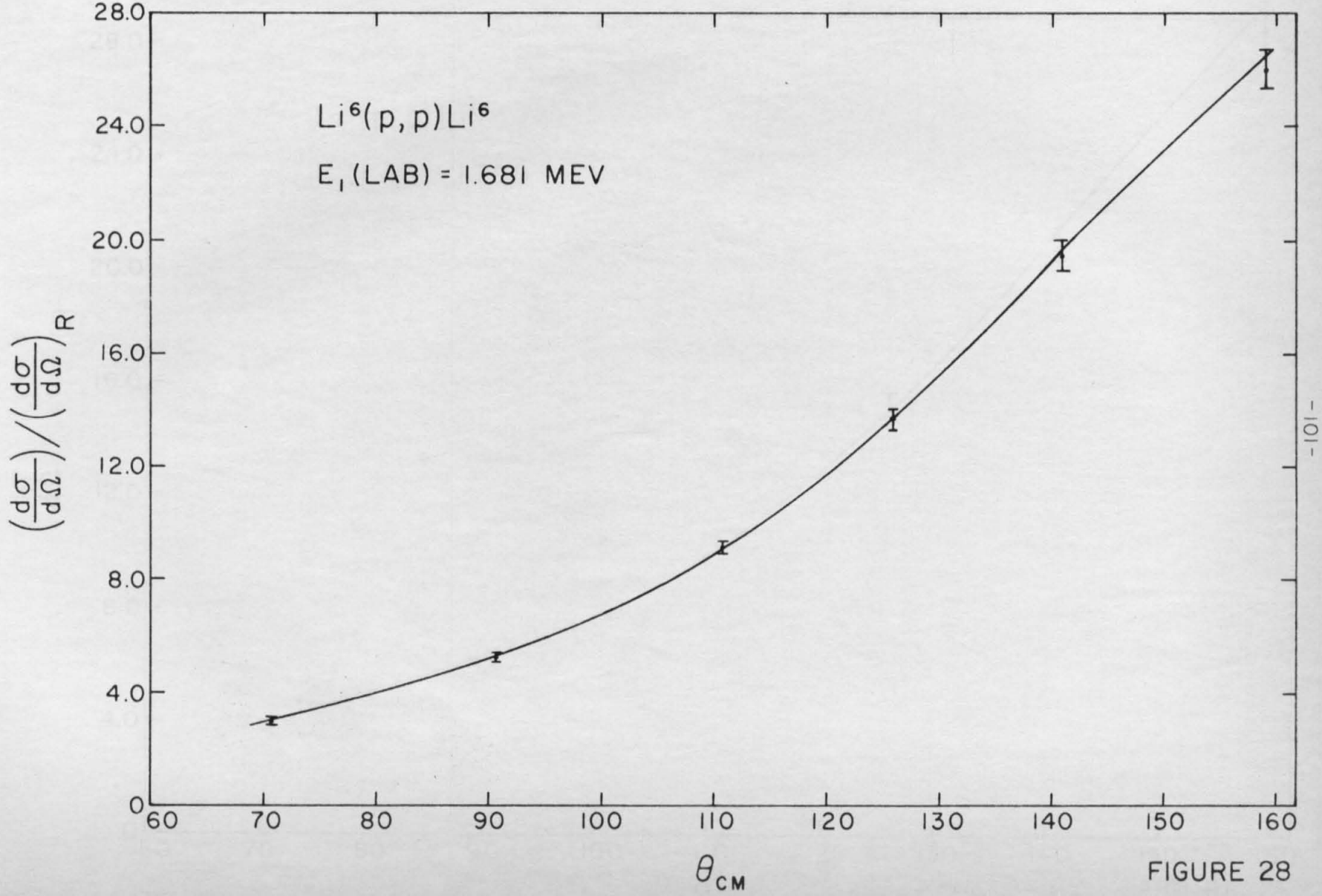
Li⁶(p, p)Li⁶
E₁(LAB) = 1.681 MEV
$\left(\frac{d\sigma}{d\Omega}\right)/\left(\frac{d\sigma}{d\Omega}\right)_R$
28.0
24.0
20.0
16.0
12.0
8.0
4.0
0
60
70
80
90
100
110
120
130
140
150
160
θ_{CM}

FIGURE 28

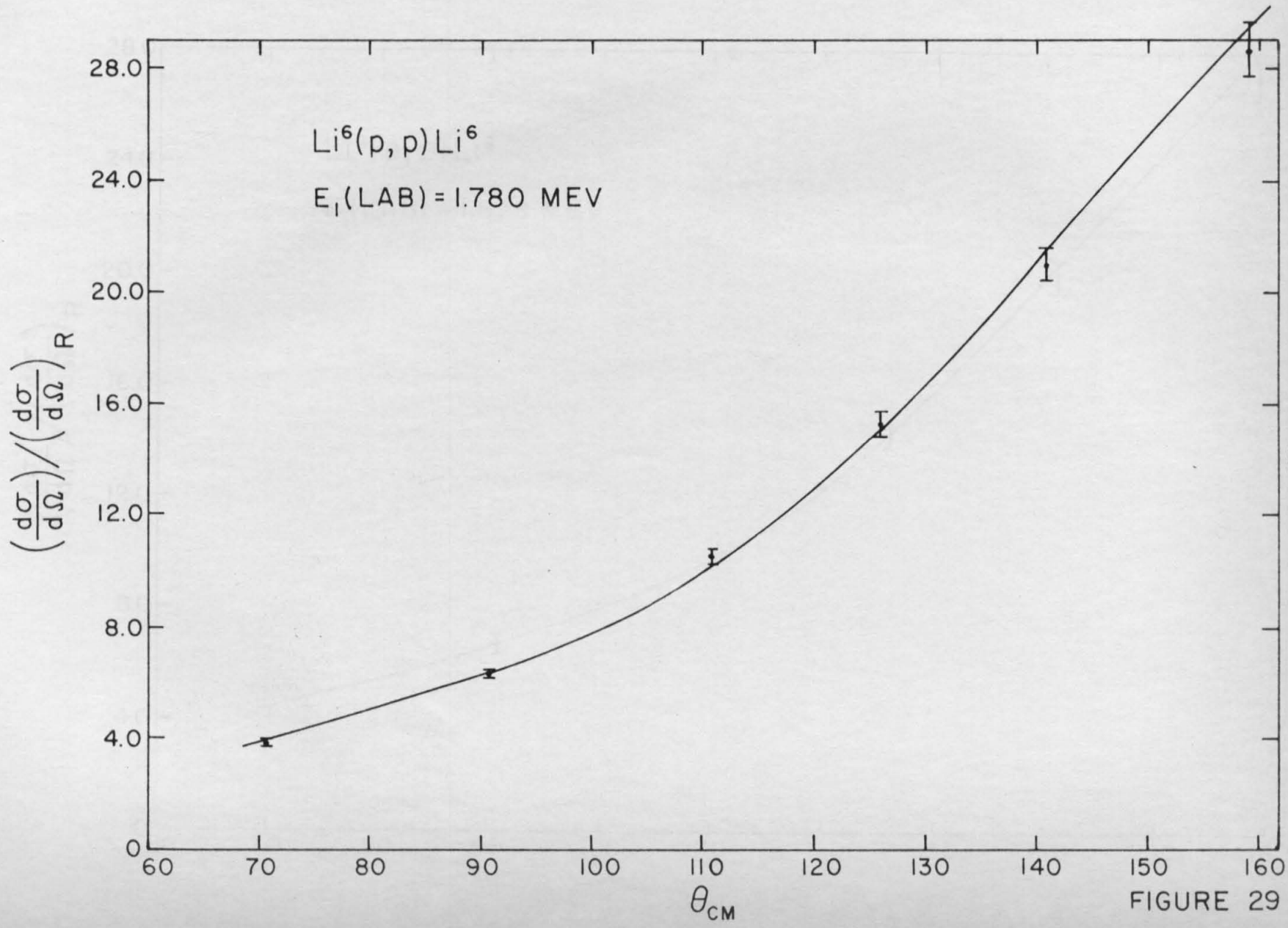
$Li^6(p, p)Li^6$
E_1(LAB) = 1.780 MEV
$\left(\frac{d\sigma}{d\Omega}\right)/\left(\frac{d\sigma}{d\Omega}\right)_R$
28.0
24.0
20.0
16.0
12.0
8.0
4.0
0
60
70
80
90
100
110
120
130
140
150
160
θ_{CM}

FIGURE 29

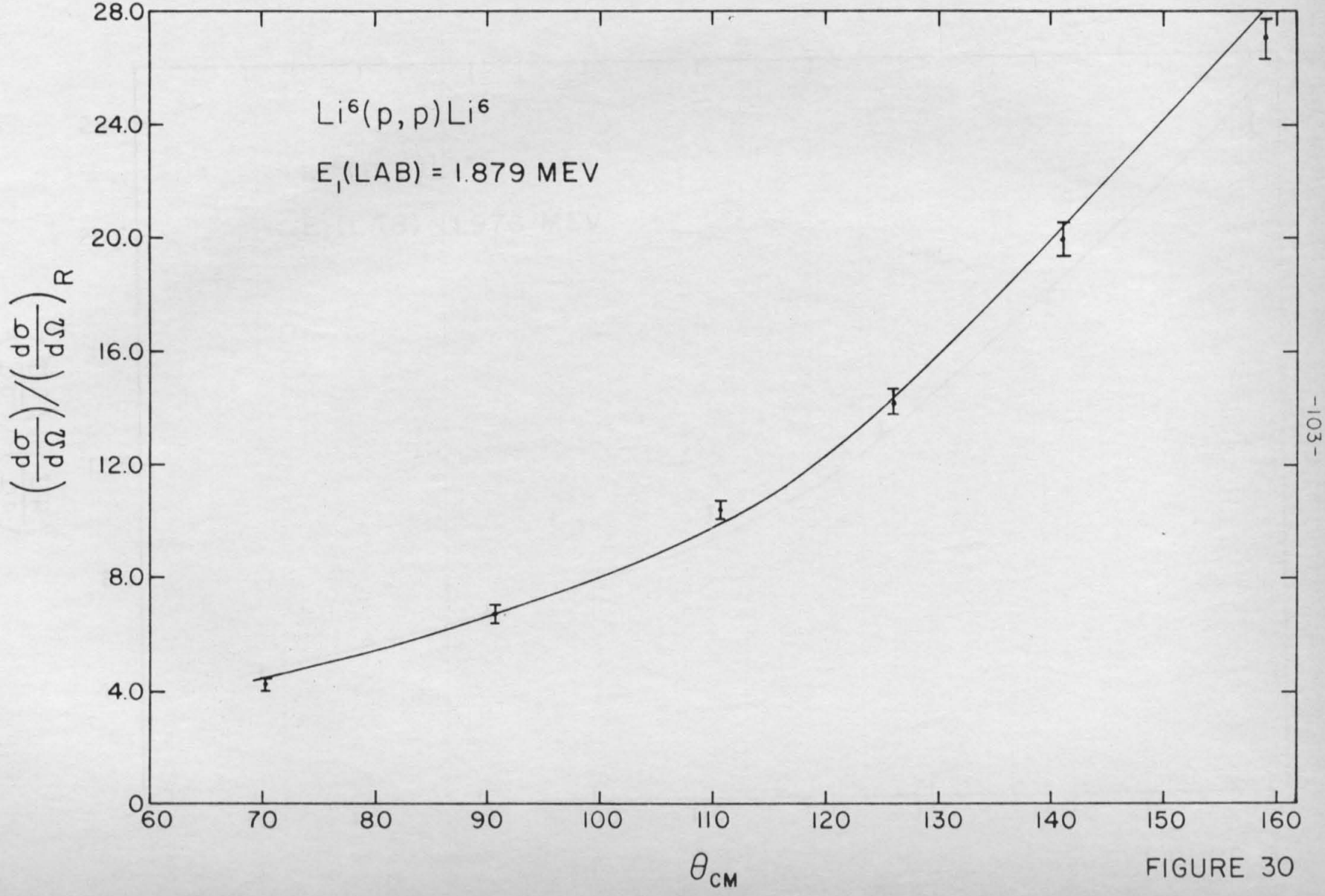
Li⁶(p, p)Li⁶
E₁(LAB) = 1.879 MEV
(dσ/dΩ)/(dσ/dΩ)R
θCM
28.0
24.0
20.0
16.0
12.0
8.0
4.0
0
60
70
80
90
100
110
120
130
140
150
160

FIGURE 30

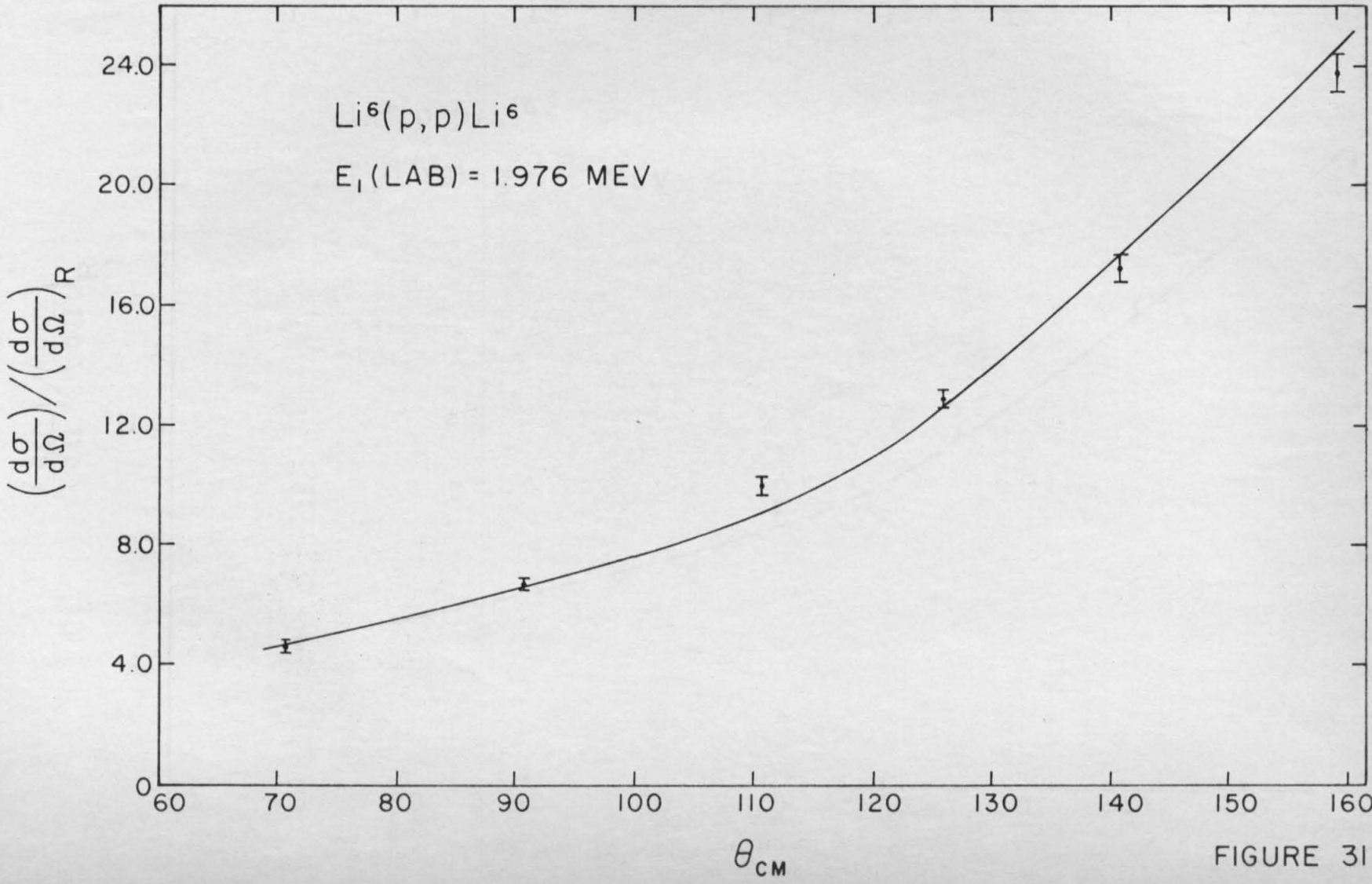
$Li^6(p,p)Li^6$
E_1(LAB) = 1.976 MEV
$\left(\frac{d\sigma}{d\Omega}\right)/\left(\frac{d\sigma}{d\Omega}\right)_R$
24.0
20.0
16.0
12.0
8.0
4.0
0
60
70
80
90
100
110
120
130
140
150
160
θ_{CM}

FIGURE 31

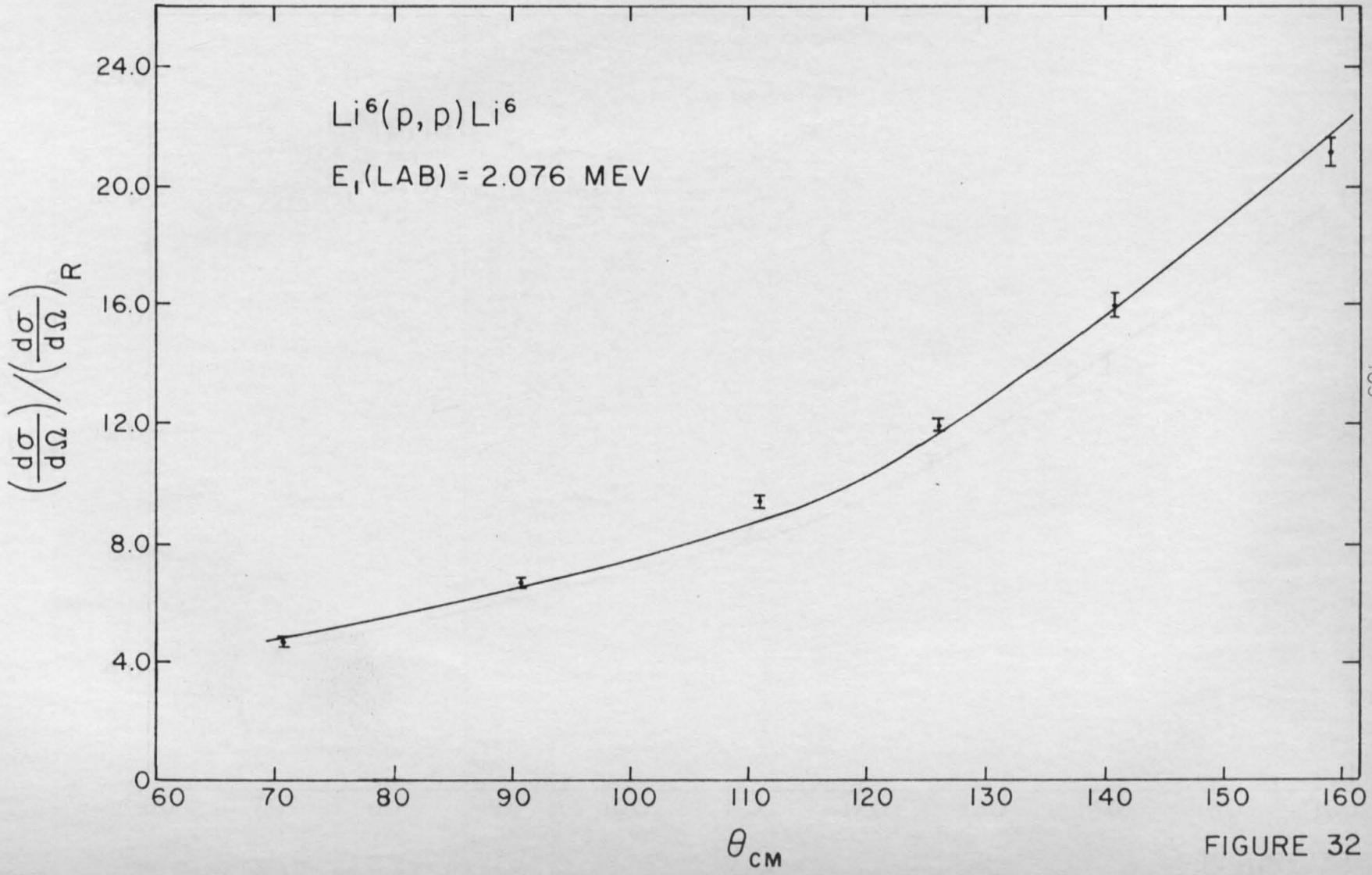
$Li^6(p,p)Li^6$
E_1(LAB) = 2.076 MEV
$\left(\frac{d\sigma}{d\Omega}\right)/\left(\frac{d\sigma}{d\Omega}\right)_R$
24.0
20.0
16.0
12.0
8.0
4.0
0
60
70
80
90
100
110
120
130
140
150
160
θ_{CM}

FIGURE 32

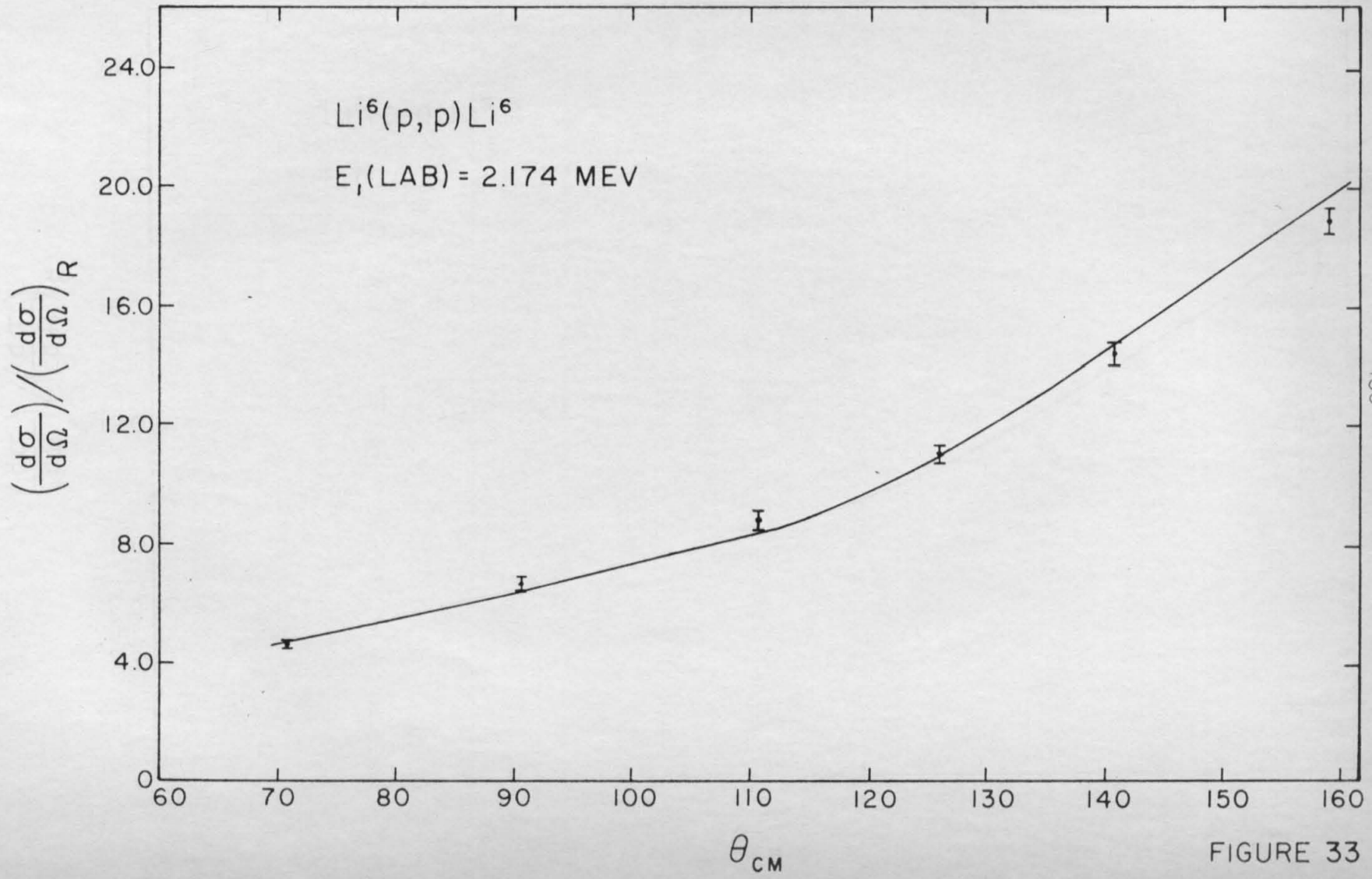
$Li^6(p, p)Li^6$
E_1(LAB) = 2.174 MEV
$\left(\frac{d\sigma}{d\Omega}\right)/\left(\frac{d\sigma}{d\Omega}\right)_R$
24.0
20.0
16.0
12.0
8.0
4.0
0
60
70
80
90
100
110
120
130
140
150
160
θ_{CM}

FIGURE 33

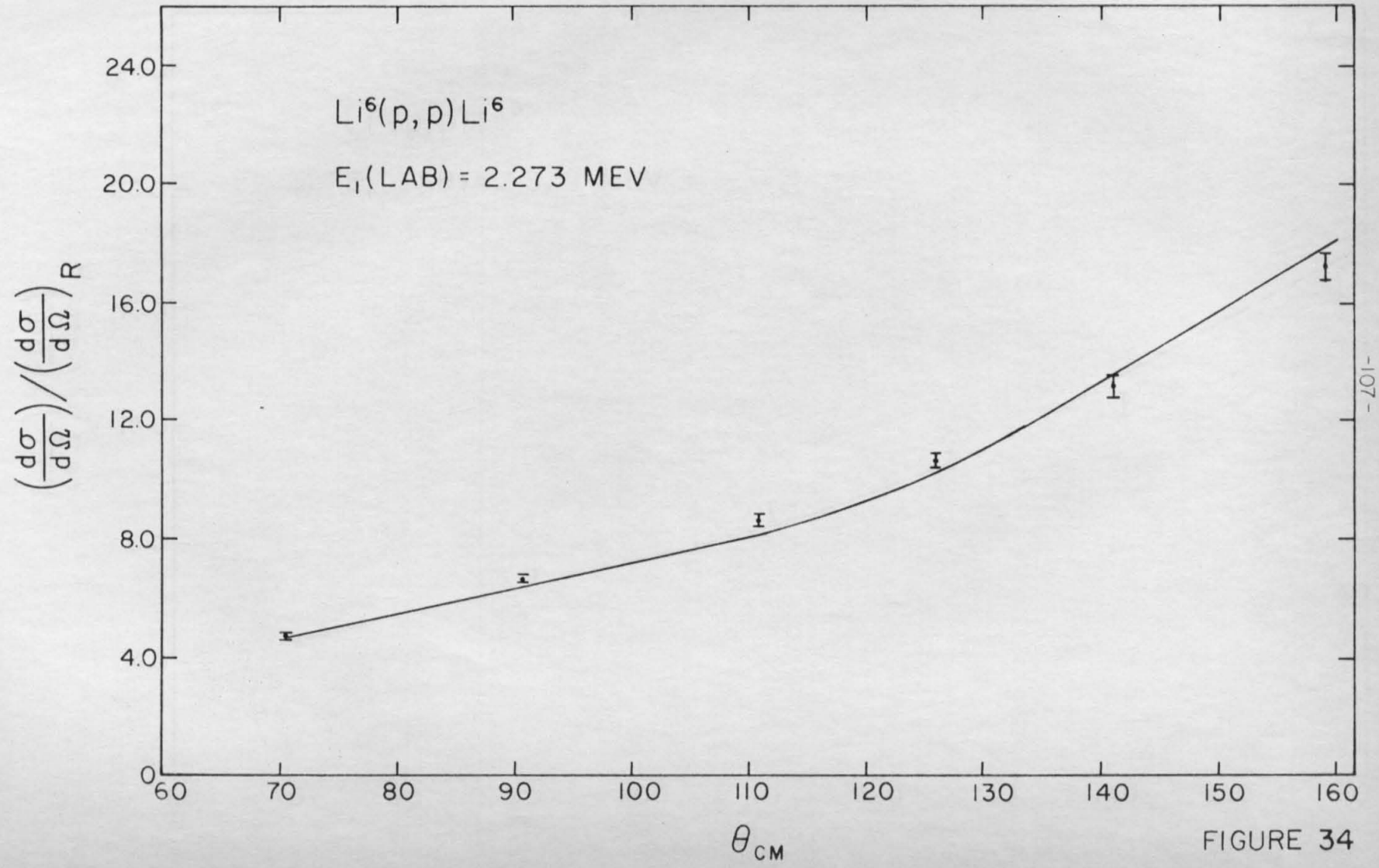
$Li^6(p,p)Li^6$
E_1(LAB) = 2.273 MEV
$\left(\frac{d\sigma}{d\Omega}\right)/\left(\frac{d\sigma}{d\Omega}\right)_R$
24.0
20.0
16.0
12.0
8.0
4.0
0
60
70
80
90
100
110
120
130
140
150
160
θ_{CM}

FIGURE 34

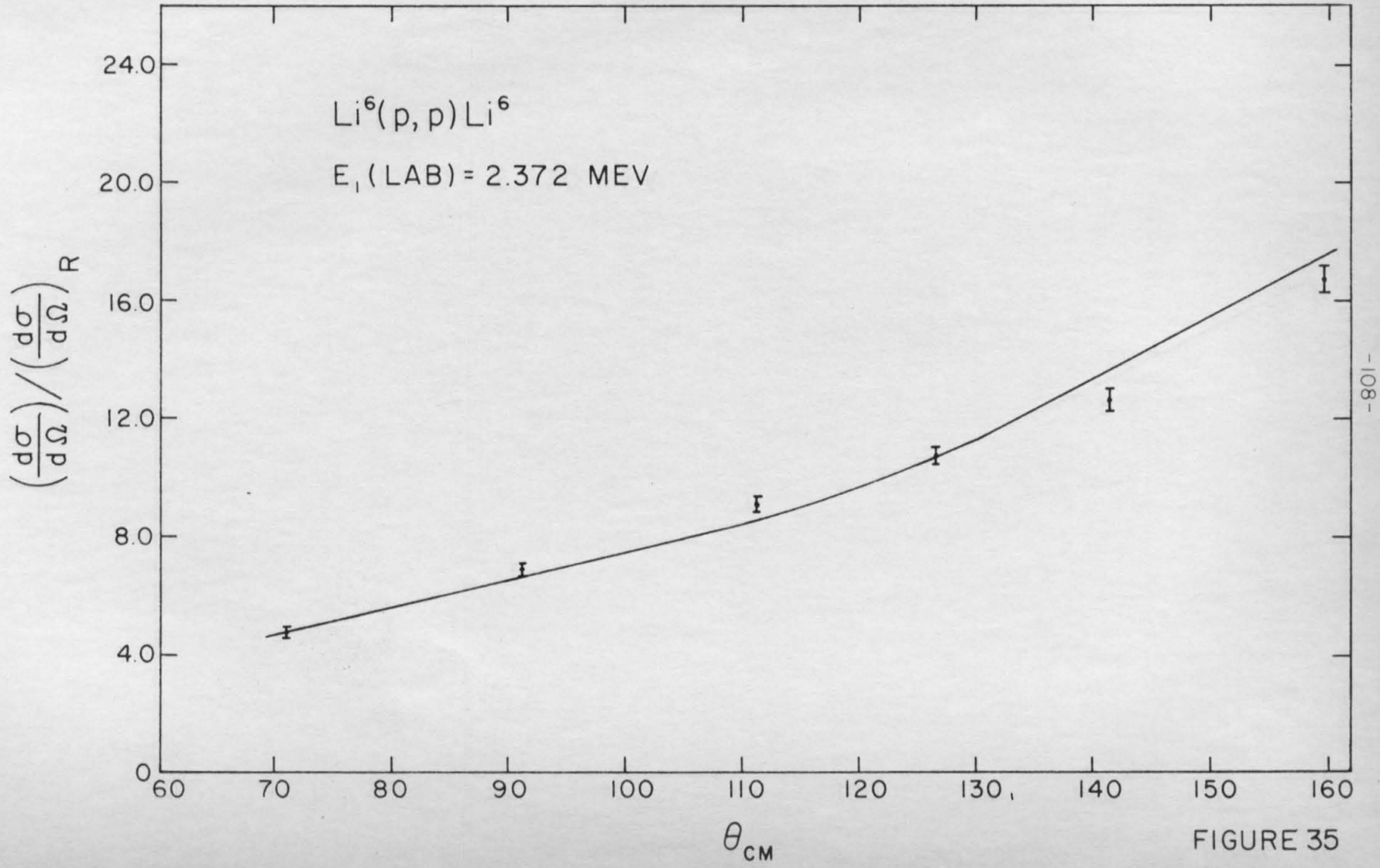
$Li^6(p,p)Li^6$
E_1 (LAB) = 2.372 MEV
$\left(\frac{d\sigma}{d\Omega}\right)/\left(\frac{d\sigma}{d\Omega}\right)_R$
24.0
20.0
16.0
12.0
8.0
4.0
0
60
70
80
90
100
110
120
130
140
150
160
θ_{CM}

FIGURE 35

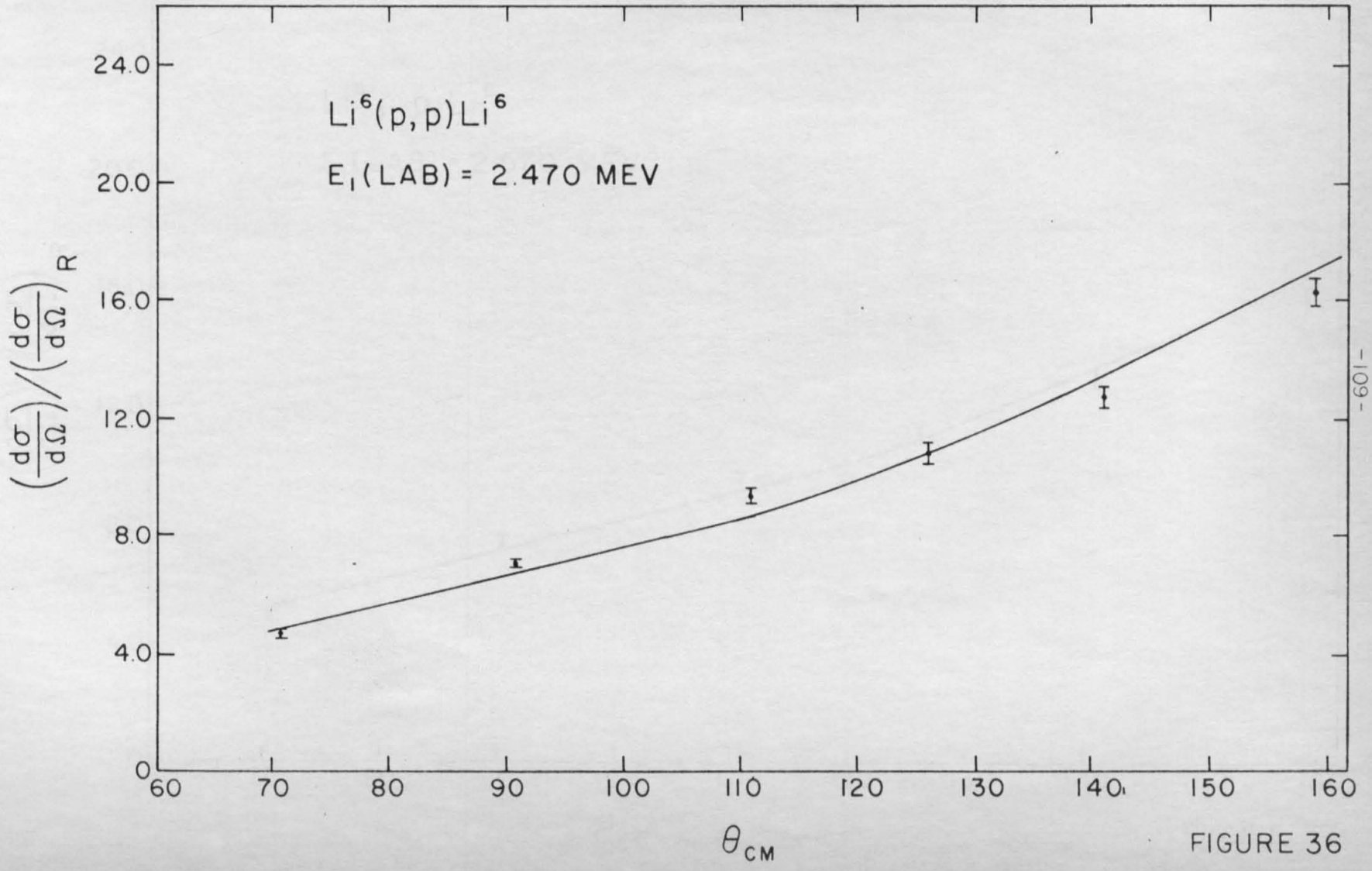
$Li^6(p,p)Li^6$
E_1(LAB) = 2.470 MEV
$\left(\frac{d\sigma}{d\Omega}\right)/\left(\frac{d\sigma}{d\Omega}\right)_R$
θ_{CM}
24.0
20.0
16.0
12.0
8.0
4.0
0
60
70
80
90
100
110
120
130
140
150
160
-109-

FIGURE 36

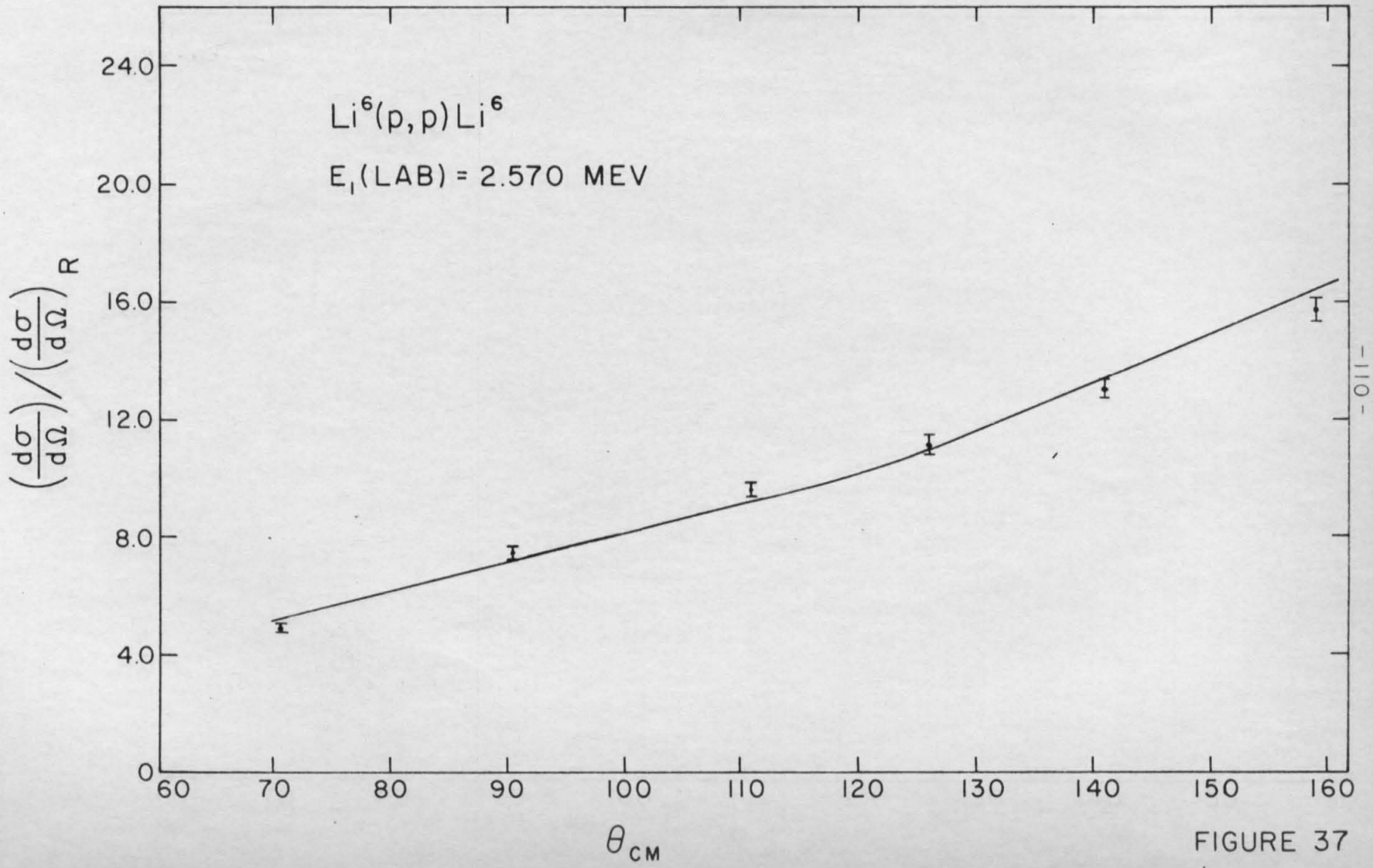
$Li^6(p,p)Li^6$
E_1(LAB) = 2.570 MEV
$\left(\frac{d\sigma}{d\Omega}\right)/\left(\frac{d\sigma}{d\Omega}\right)_R$
24.0
20.0
16.0
12.0
8.0
4.0
0
60
70
80
90
100
110
120
130
140
150
160
θ_{CM}

FIGURE 37

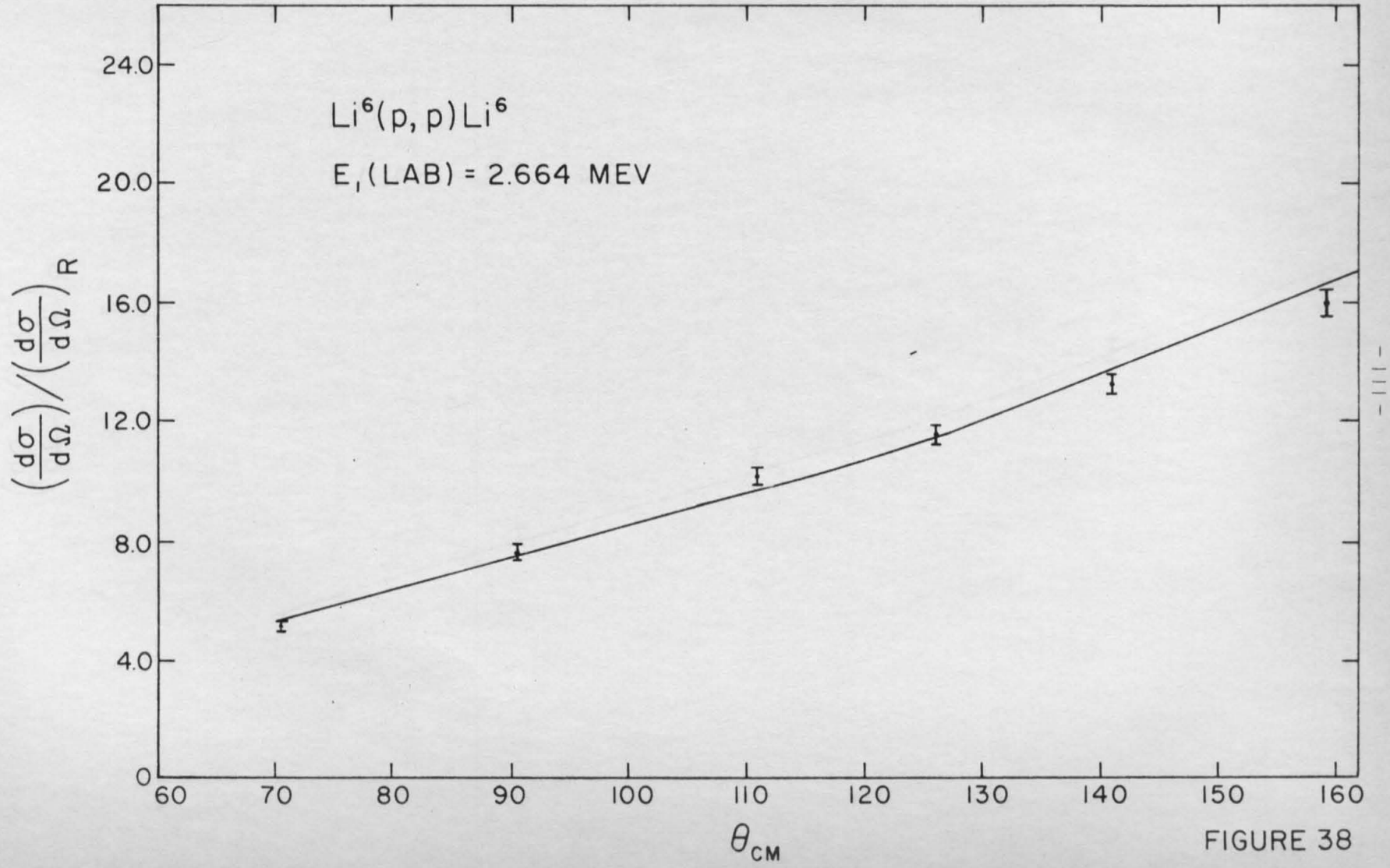
$Li^6(p, p)Li^6$
E_1(LAB) = 2.664 MEV
$\left(\frac{d\sigma}{d\Omega}\right)/\left(\frac{d\sigma}{d\Omega}\right)_R$
θ_{CM}
0
4.0
8.0
12.0
16.0
20.0
24.0
60
70
80
90
100
110
120
130
140
150
160

FIGURE 38

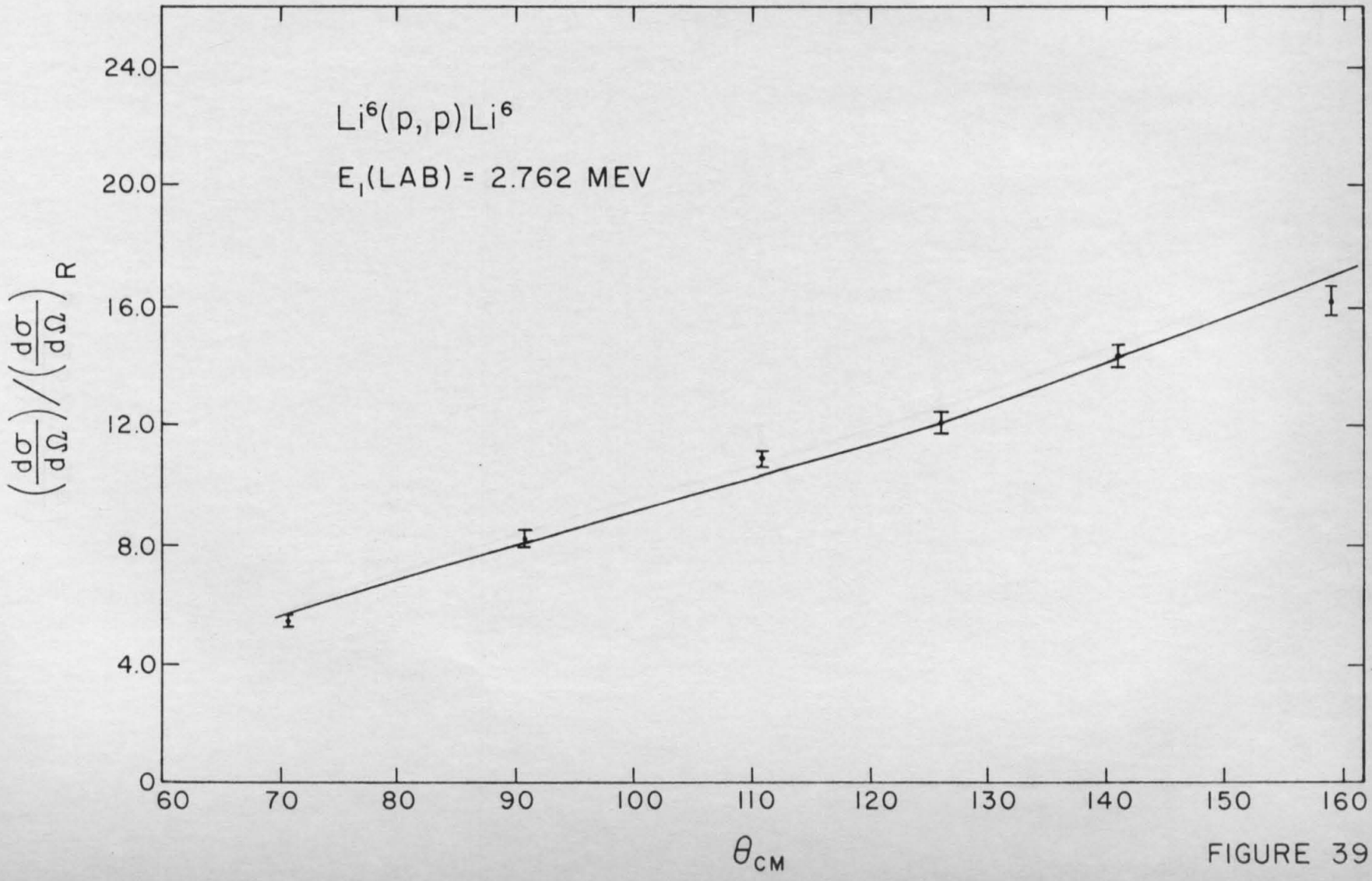
$Li^6(p, p)Li^6$
E_1(LAB) = 2.762 MEV
$\left(\frac{d\sigma}{d\Omega}\right)/\left(\frac{d\sigma}{d\Omega}\right)_R$
24.0
20.0
16.0
12.0
8.0
4.0
0
60
70
80
90
100
110
120
130
140
150
160
θ_{CM}

FIGURE 39

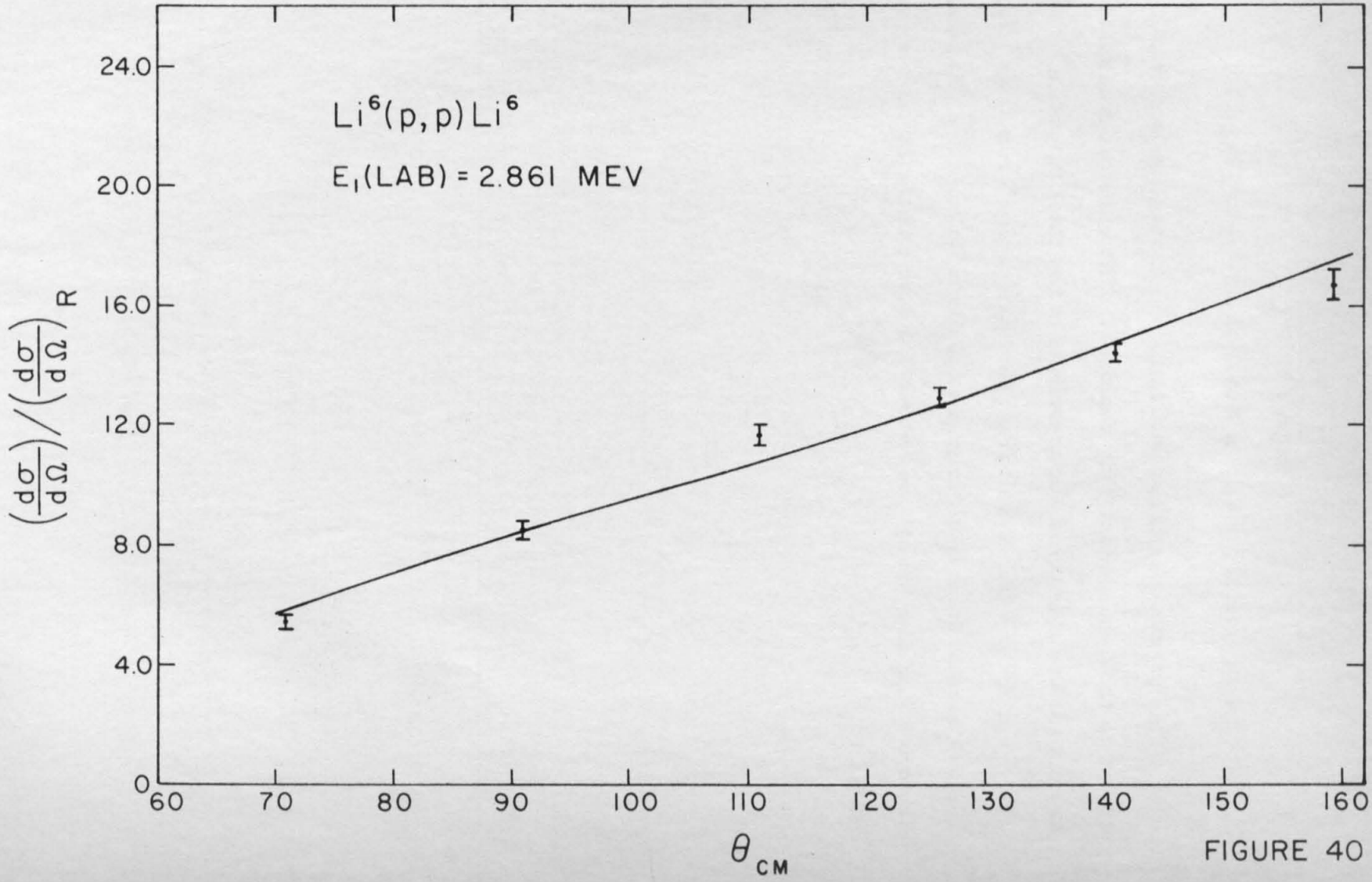
$Li^6(p,p)Li^6$
E_1(LAB) = 2.861 MEV
$\left(\frac{d\sigma}{d\Omega}\right)/\left(\frac{d\sigma}{d\Omega}\right)_R$
24.0
20.0
16.0
12.0
8.0
4.0
0
60
70
80
90
100
110
120
130
140
150
160
θ_{CM}

FIGURE 40

Figure 41

Spectrometer Profile of Reaction Products (Page 28)

This profile was taken with the 16-inch spectrometer and a Li^6 target in the 6-inch scattering chamber. The curve represented by the dots is the measured superposition of the thick target α^{++} and He^{3++} profiles which result from the $Li^6(p, \alpha)He^3$ reaction. The method used to interpret the profile is given on page 28. The incident laboratory proton energy was about 2.3 Mev and the laboratory angle $95^o45'$.

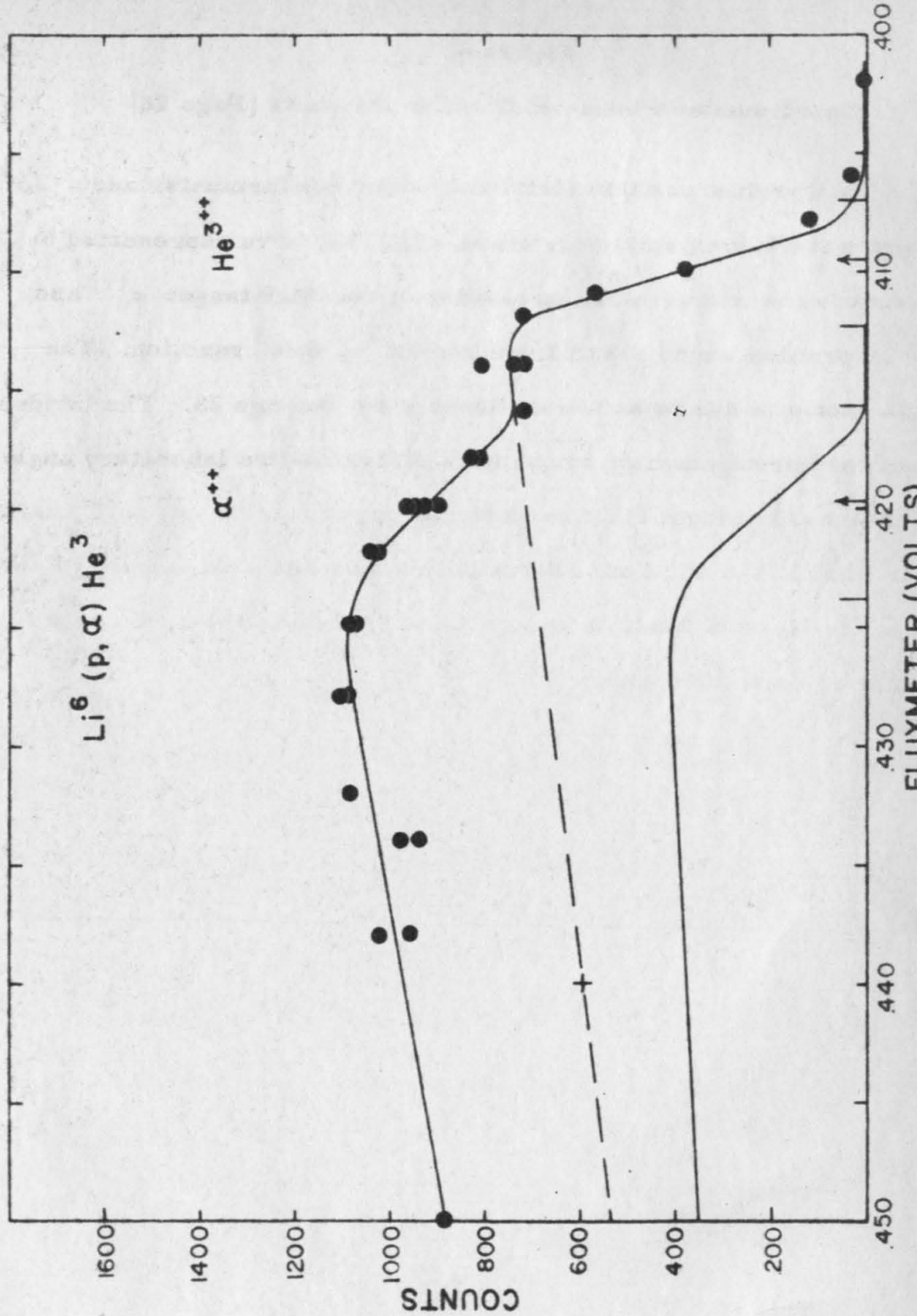
Li^6 (p, α) He^3
α^{++}
He^{3++}
COUNTS
1600
1400
1200
1000
800
600
400
200
400
410
420
430
440
450
FLUXMETER (VOLTS)

Figure 42

Integrated Reaction Cross Section for $Li^6(p, \alpha)He^3$ (Page 30)

The low energy data indicated by the solid line are those of Sawyer and Phillips, (Sawyer, 1953). The data indicated by solid dots are those of Marion, Weber and Mozer, (Marion, 1956), normalized to measurements made in this experiment. The energy E_1 (Mev) is the energy of the proton in the laboratory system.

The curve indicated by the open circles is that calculated for a $5/2^-$ p-wave resonant state as shown on page 49. The curve indicated by crosses is the difference between this curve and the measured curve and is the s-wave reaction background assumed in the analysis of the scattering data. (See Table 5.)

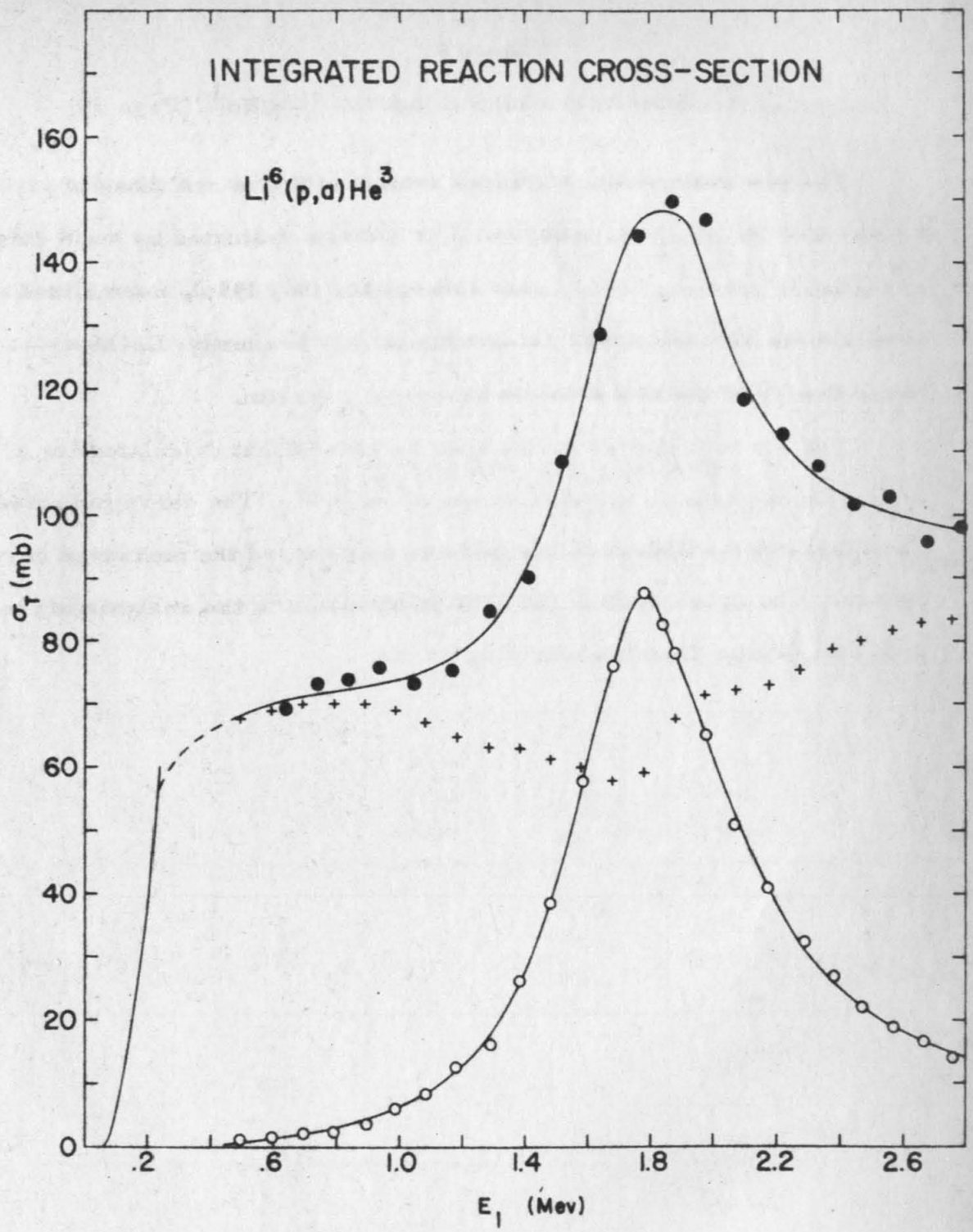
INTEGRATED REACTION CROSS-SECTION
Li⁶(p,α)He³
σT (mb)
E1 (Mev)
0
20
40
60
80
100
120
140
160
.2
.6
1.0
1.4
1.8
2.2
2.6

Figure 43

Amplitude Matrix Diagram (Page 35)

The elements of the amplitude matrix (equation 68) are displayed for the case of s- and p-waves. For convenience the factors $\frac{i\sqrt{\pi}}{k_a}(2\ell+1)^{1/2}e^{i(\eta_\ell+\eta_{\ell'}-2\eta_0)}$ are left out and only the Clebsch Gordan coefficients, the exit spherical harmonics and the nuclear amplitudes are given. The general notation is

$$(\ell\, s\, o\nu/JM)(\ell' s' m_{\ell'}\nu'/JM) f^J_{ss'\ell\ell'} Y^{m_{\ell'}}_{\ell'}$$

The amplitudes within each box add and correspond to coherent processes. The cross section for scattering then is found by squaring each box, adding them and dividing by six.

AMPLITUDE MATRIX

$Li^6(p,p)Li^6$

J_f^π, T_f \ J_i^π, T_i	$\frac{1}{2}, \frac{1}{2}$	$\frac{1}{2}, -\frac{1}{2}$	$\frac{3}{2}, \frac{3}{2}$	$\frac{3}{2}, \frac{1}{2}$	$\frac{3}{2}, -\frac{1}{2}$	$\frac{3}{2}, -\frac{3}{2}$
$\frac{1}{2}, \frac{1}{2}$	$f_c + f^{\frac{1}{2}}_{\frac{1}{2}\frac{1}{2}}{}_{ss}\, Y_0^0$ $+\frac{1}{3} f^{\frac{1}{2}}_{\frac{1}{2}\frac{1}{2}}{}_{pp}\, Y_1^0$ $+\frac{2}{3} f^{\frac{3}{2}}_{\frac{1}{2}\frac{1}{2}}{}_{pp}\, Y_1^0$	$-\sqrt{\frac{2}{9}} f^{\frac{1}{2}}_{\frac{1}{2}\frac{1}{2}}{}_{pp}\, Y_1^1$ $+\sqrt{\frac{2}{9}} f^{\frac{3}{2}}_{\frac{1}{2}\frac{1}{2}}{}_{pp}\, Y_1^1$	$-\sqrt{\frac{1}{6}} f^{\frac{1}{2}}_{\frac{1}{2}\frac{3}{2}}{}_{pp}\, Y_1^{-1}$ $+\sqrt{\frac{4}{15}} f^{\frac{3}{2}}_{\frac{1}{2}\frac{3}{2}}{}_{pp}\, Y_1^{-1}$	$+\frac{1}{3} f^{\frac{1}{2}}_{\frac{1}{2}\frac{1}{2}}{}_{pp}\, Y_1^0$ $+\sqrt{\frac{2}{45}} f^{\frac{3}{2}}_{\frac{1}{2}\frac{1}{2}}{}_{pp}\, Y_1^0$	$-\sqrt{\frac{1}{18}} f^{\frac{1}{2}}_{\frac{1}{2}\frac{1}{2}}{}_{pp}\, Y_1^1$ $-\sqrt{\frac{16}{45}} f^{\frac{3}{2}}_{\frac{1}{2}\frac{1}{2}}{}_{pp}\, Y_1^1$	
$\frac{1}{2}, -\frac{1}{2}$	$-\sqrt{\frac{2}{9}} f^{\frac{1}{2}}_{\frac{1}{2}\frac{1}{2}}{}_{pp}\, Y_1^{-1}$ $+\sqrt{\frac{2}{9}} f^{\frac{3}{2}}_{\frac{1}{2}\frac{1}{2}}{}_{pp}\, Y_1^{-1}$	$f_c + f^{\frac{1}{2}}_{\frac{1}{2}\frac{1}{2}}{}_{ss}\, Y_0^0$ $+\frac{1}{3} f^{\frac{1}{2}}_{\frac{1}{2}\frac{1}{2}}{}_{pp}\, Y_1^0$ $+\frac{2}{3} f^{\frac{3}{2}}_{\frac{1}{2}\frac{1}{2}}{}_{pp}\, Y_1^0$		$+\sqrt{\frac{1}{18}} f^{\frac{1}{2}}_{\frac{1}{2}\frac{3}{2}}{}_{pp}\, Y_1^{-1}$ $+\sqrt{\frac{16}{45}} f^{\frac{3}{2}}_{\frac{1}{2}\frac{3}{2}}{}_{pp}\, Y_1^{-1}$	$-\frac{1}{3} f^{\frac{1}{2}}_{\frac{1}{2}\frac{3}{2}}{}_{pp}\, Y_1^0$ $-\sqrt{\frac{2}{45}} f^{\frac{3}{2}}_{\frac{1}{2}\frac{3}{2}}{}_{pp}\, Y_1^0$	$+\sqrt{\frac{1}{6}} f^{\frac{1}{2}}_{\frac{1}{2}\frac{3}{2}}{}_{pp}\, Y_1^1$ $-\sqrt{\frac{4}{15}} f^{\frac{3}{2}}_{\frac{1}{2}\frac{3}{2}}{}_{pp}\, Y_1^1$
$\frac{3}{2}, \frac{3}{2}$	$+\sqrt{\frac{10}{3}} f^{\frac{3}{2}}_{\frac{1}{2}\frac{1}{2}}{}_{pp}\, Y_1^1$		$f_c + f^{\frac{3}{2}}_{\frac{3}{2}\frac{3}{2}}{}_{ss}\, Y_0^0$ $+\frac{3}{5} f^{\frac{1}{2}}_{\frac{3}{2}\frac{3}{2}}{}_{pp}\, Y_1^0$ $+\frac{2}{5} f^{\frac{3}{2}}_{\frac{3}{2}\frac{3}{2}}{}_{pp}\, Y_1^0$	$-\sqrt{\frac{6}{25}} f^{\frac{3}{2}}_{\frac{3}{2}\frac{1}{2}}{}_{pp}\, Y_1^1$ $+\sqrt{\frac{6}{25}} f^{\frac{3}{2}}_{\frac{3}{2}\frac{3}{2}}{}_{pp}\, Y_1^1$		
$\frac{3}{2}, \frac{1}{2}$	$+\frac{1}{3} f^{\frac{1}{2}}_{\frac{3}{2}\frac{1}{2}}{}_{pp}\, Y_1^0$ $+\sqrt{\frac{2}{45}} f^{\frac{3}{2}}_{\frac{3}{2}\frac{1}{2}}{}_{pp}\, Y_1^0$	$-\sqrt{\frac{2}{9}} f^{\frac{1}{2}}_{\frac{3}{2}\frac{1}{2}}{}_{pp}\, Y_1^1$ $+\sqrt{\frac{1}{45}} f^{\frac{3}{2}}_{\frac{3}{2}\frac{1}{2}}{}_{pp}\, Y_1^1$	$-\sqrt{\frac{1}{6}} f^{\frac{1}{2}}_{\frac{3}{2}\frac{3}{2}}{}_{pp}\, Y_1^{-1}$ $+\sqrt{\frac{2}{75}} f^{\frac{3}{2}}_{\frac{3}{2}\frac{3}{2}}{}_{pp}\, Y_1^{-1}$ $+\sqrt{\frac{3}{50}} f^{\frac{5}{2}}_{\frac{3}{2}\frac{3}{2}}{}_{pp}\, Y_1^{-1}$	$f_c + f^{\frac{3}{2}}_{\frac{3}{2}\frac{1}{2}}{}_{ss}\, Y_0^0$ $+\frac{1}{3} f^{\frac{1}{2}}_{\frac{3}{2}\frac{1}{2}}{}_{pp}\, Y_1^0$ $+\frac{1}{15} f^{\frac{3}{2}}_{\frac{3}{2}\frac{1}{2}}{}_{pp}\, Y_1^0$ $+\frac{3}{5} f^{\frac{5}{2}}_{\frac{3}{2}\frac{1}{2}}{}_{pp}\, Y_1^0$	$-\sqrt{\frac{1}{18}} f^{\frac{1}{2}}_{\frac{3}{2}\frac{3}{2}}{}_{pp}\, Y_1^1$ $-\sqrt{\frac{8}{225}} f^{\frac{3}{2}}_{\frac{3}{2}\frac{3}{2}}{}_{pp}\, Y_1^1$ $+\sqrt{\frac{9}{50}} f^{\frac{5}{2}}_{\frac{3}{2}\frac{3}{2}}{}_{pp}\, Y_1^1$	
$\frac{3}{2}, -\frac{1}{2}$	$+\sqrt{\frac{2}{9}} f^{\frac{1}{2}}_{\frac{3}{2}\frac{1}{2}}{}_{pp}\, Y_1^{-1}$ $-\sqrt{\frac{1}{45}} f^{\frac{3}{2}}_{\frac{3}{2}\frac{1}{2}}{}_{pp}\, Y_1^{-1}$	$-\frac{1}{3} f^{\frac{1}{2}}_{\frac{3}{2}\frac{1}{2}}{}_{pp}\, Y_1^0$ $-\sqrt{\frac{2}{45}} f^{\frac{3}{2}}_{\frac{3}{2}\frac{1}{2}}{}_{pp}\, Y_1^0$		$-\sqrt{\frac{1}{18}} f^{\frac{1}{2}}_{\frac{3}{2}\frac{3}{2}}{}_{pp}\, Y_1^{-1}$ $-\sqrt{\frac{8}{225}} f^{\frac{3}{2}}_{\frac{3}{2}\frac{3}{2}}{}_{pp}\, Y_1^{-1}$ $+\sqrt{\frac{9}{50}} f^{\frac{5}{2}}_{\frac{3}{2}\frac{3}{2}}{}_{pp}\, Y_1^{-1}$	$f_c + f^{\frac{3}{2}}_{\frac{3}{2}\frac{3}{2}}{}_{ss}\, Y_0^0$ $+\frac{1}{5} f^{\frac{1}{2}}_{\frac{3}{2}\frac{3}{2}}{}_{pp}\, Y_1^0$ $+\frac{1}{15} f^{\frac{3}{2}}_{\frac{3}{2}\frac{3}{2}}{}_{pp}\, Y_1^0$ $+\frac{3}{5} f^{\frac{5}{2}}_{\frac{3}{2}\frac{3}{2}}{}_{pp}\, Y_1^0$	$-\sqrt{\frac{1}{6}} f^{\frac{1}{2}}_{\frac{3}{2}\frac{3}{2}}{}_{pp}\, Y_1^1$ $+\sqrt{\frac{2}{75}} f^{\frac{3}{2}}_{\frac{3}{2}\frac{3}{2}}{}_{pp}\, Y_1^1$ $+\sqrt{\frac{3}{50}} f^{\frac{5}{2}}_{\frac{3}{2}\frac{3}{2}}{}_{pp}\, Y_1^1$
$\frac{3}{2}, -\frac{3}{2}$		$-\sqrt{\frac{3}{5}} f^{\frac{3}{2}}_{\frac{3}{2}\frac{3}{2}}{}_{pp}\, Y_1^{-1}$			$-\sqrt{\frac{6}{25}} f^{\frac{3}{2}}_{\frac{3}{2}\frac{3}{2}}{}_{pp}\, Y_1^{-1}$ $+\sqrt{\frac{6}{25}} f^{\frac{5}{2}}_{\frac{3}{2}\frac{3}{2}}{}_{pp}\, Y_1^{-1}$	$f_c + f^{\frac{3}{2}}_{\frac{3}{2}\frac{3}{2}}{}_{ss}\, Y_0^0$ $+\frac{3}{5} f^{\frac{1}{2}}_{\frac{3}{2}\frac{3}{2}}{}_{pp}\, Y_1^0$ $+\frac{2}{5} f^{\frac{5}{2}}_{\frac{3}{2}\frac{3}{2}}{}_{pp}\, Y_1^0$

Figure 44

Energy Level Diagram for Mirror Nuclei Li^7 and Be^7 (Page 39)

The corresponding nuclear levels of Li^7 and Be^7 are shown here with their assigned spins and parties. (Ajzenberg-Selove, 1959.)

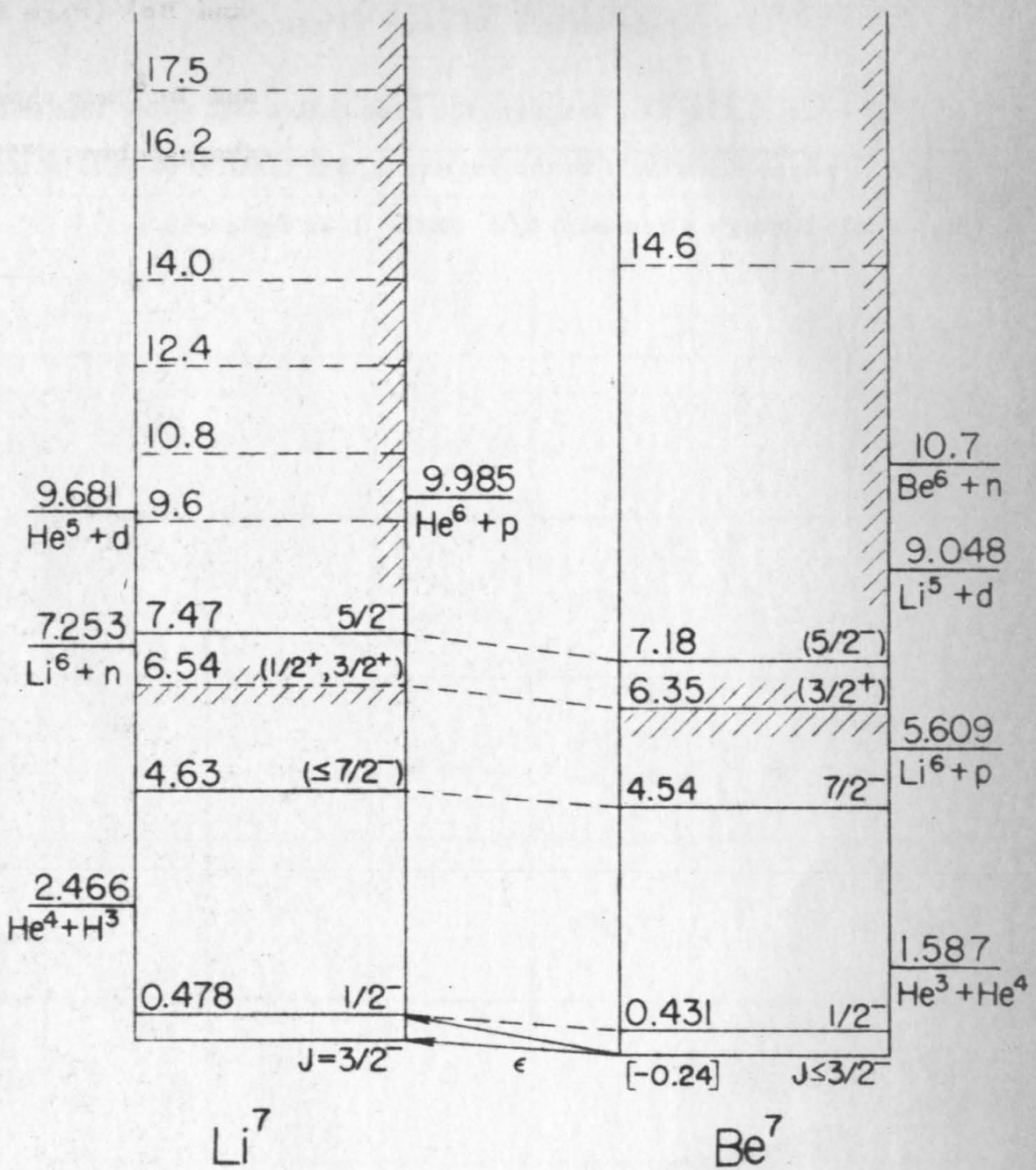
17.5
16.2
14.0
12.4
10.8
9.681
He5 + d
9.6
9.985
He6 + p
7.253
Li6 + n
7.47
5/2−
6.54
(1/2+, 3/2+)
4.63
(≤7/2−)
2.466
He4+H3
0.478
1/2−
J=3/2−
ε
14.6
7.18
(5/2−)
6.35
(3/2+)
4.54
7/2−
0.431
1/2−
[-0.24]
J≤3/2−
10.7
Be6 + n
9.048
Li5 + d
5.609
Li6 + p
1.587
He3 + He4
Li7
Be7

Figure 45

Amplitude Matrix Diagram (Page 40)

In constructing this diagram the assumption was made that only s- and p-waves contribute to the scattering and that the p-wave scattering is only through a resonant $5/2^-$ state. (See figure 43.)

AMPLITUDE MATRIX

$Li^6(p,p)Li^6$

Channel Spin, S_{in} / S_{out}	$\frac{1}{2},\frac{1}{2}$	$\frac{1}{2},-\frac{1}{2}$	$\frac{3}{2},\frac{3}{2}$	$\frac{3}{2},\frac{1}{2}$	$\frac{3}{2},-\frac{1}{2}$	$\frac{3}{2},-\frac{3}{2}$
$\frac{1}{2},\frac{1}{2}$	$f_c+f^{\frac{1}{2}\frac{1}{2}}_{\frac{1}{2}\frac{1}{2}\,ss}\,Y_0^0$					
$\frac{1}{2},-\frac{1}{2}$		$f_c+f^{\frac{1}{2}\frac{1}{2}}_{\frac{1}{2}\frac{1}{2}\,ss}\,Y_0^0$				
$\frac{3}{2},\frac{3}{2}$			$f_c+f^{\frac{3}{2}\frac{3}{2}}_{\frac{3}{2}\frac{3}{2}\,ss}\,Y_0^0$ $+\frac{2}{5}f^{\frac{1}{2}\frac{1}{2}}_{\frac{1}{2}\frac{1}{2}\,pp}\,Y_1^0$	$+\sqrt{\frac{6}{25}}\,f^{\frac{3}{2}\frac{1}{2}}_{\frac{3}{2}\frac{1}{2}\,pp}\,Y_1^1$		
$\frac{3}{2},\frac{1}{2}$			$+\sqrt{\frac{3}{50}}\,f^{\frac{3}{2}\frac{1}{2}}_{\frac{3}{2}\frac{1}{2}\,pp}\,Y_1^{-1}$	$f_c+f^{\frac{3}{2}\frac{1}{2}}_{\frac{3}{2}\frac{1}{2}\,ss}\,Y_0^0$ $+\frac{3}{5}f^{\frac{1}{2}\frac{3}{2}}_{\frac{1}{2}\frac{3}{2}\,pp}\,Y_1^0$	$+\sqrt{\frac{3}{50}}\,f^{\frac{1}{2}\frac{1}{2}}_{\frac{1}{2}\frac{3}{2}\,pp}\,Y_1^1$	
$\frac{3}{2},-\frac{1}{2}$				$+\sqrt{\frac{3}{50}}\,f^{\frac{1}{2}\frac{1}{2}}_{\frac{1}{2}\frac{3}{2}\,pp}\,Y_1^{-1}$	$f_c+f^{\frac{3}{2}\frac{1}{2}}_{\frac{3}{2}\frac{1}{2}\,ss}\,Y_0^0$ $+\frac{3}{5}f^{\frac{1}{2}\frac{3}{2}}_{\frac{1}{2}\frac{3}{2}\,pp}\,Y_1^0$	$+\sqrt{\frac{3}{50}}\,f^{\frac{3}{2}\frac{1}{2}}_{\frac{3}{2}\frac{3}{2}\,pp}\,Y_1^1$
$\frac{3}{2},-\frac{3}{2}$					$+\sqrt{\frac{6}{25}}\,f^{\frac{3}{2}\frac{3}{2}}_{\frac{3}{2}\frac{3}{2}\,pp}\,Y_1^{-1}$	$f_c+f^{\frac{3}{2}\frac{3}{2}}_{\frac{3}{2}\frac{3}{2}\,ss}\,Y_0^0$ $+\frac{2}{5}f^{\frac{1}{2}\frac{1}{2}}_{\frac{3}{2}\frac{3}{2}\,pp}\,Y_1^0$

Figure 46

S-wave Scattering Amplitude Diagram (Page 44)

The equation $Y = A(\theta)X + B(\theta)$, where $B(\theta)$ is the s-wave intercept, is plotted in the complex plane for the six C. M. angles used in the experiment. At this low energy the six lines do come to an intersection within the experimental relative errors. The complex point (X, Y) must be the same for all angles at a given energy and must fall within the inner circle with radius equal to $(1 - U)^{1/2}$.

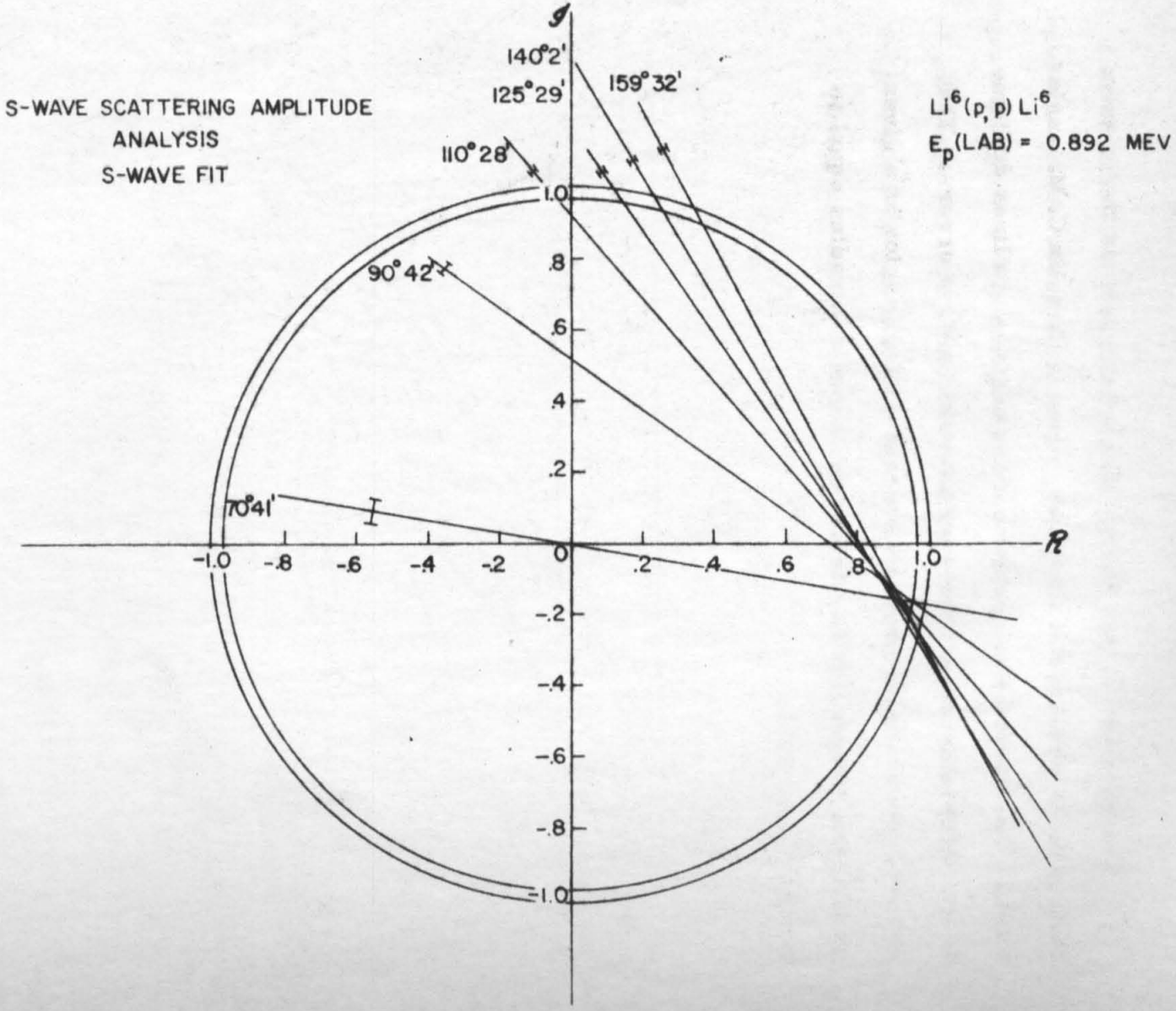
S-WAVE SCATTERING AMPLITUDE
ANALYSIS
S-WAVE FIT
Li⁶(p, p) Li⁶
Ep(LAB) = 0.892 MEV
I
R
140°2'
125°29'
159°32'
110°28'
90°42'
70°41'
1.0
.8
.6
.4
.2
0
-.2
-.4
-.6
-.8
-1.0

Figure 47

S-wave Scattering Amplitude Diagram (Page 44)

The six lines at this energy do not intersect and indicate that the resonant structure at this energy cannot be described by s-waves alone. The dashed lines represent the addition of the $H(\theta)$ intercepts to the $B(\theta)$ intercepts. Since an intersection is still not possible, the s-wave, p-wave interference intercept $ZG(\theta)$ must be computed for each angle. Figure 49 illustrates the solution which was finally taken as acceptable.

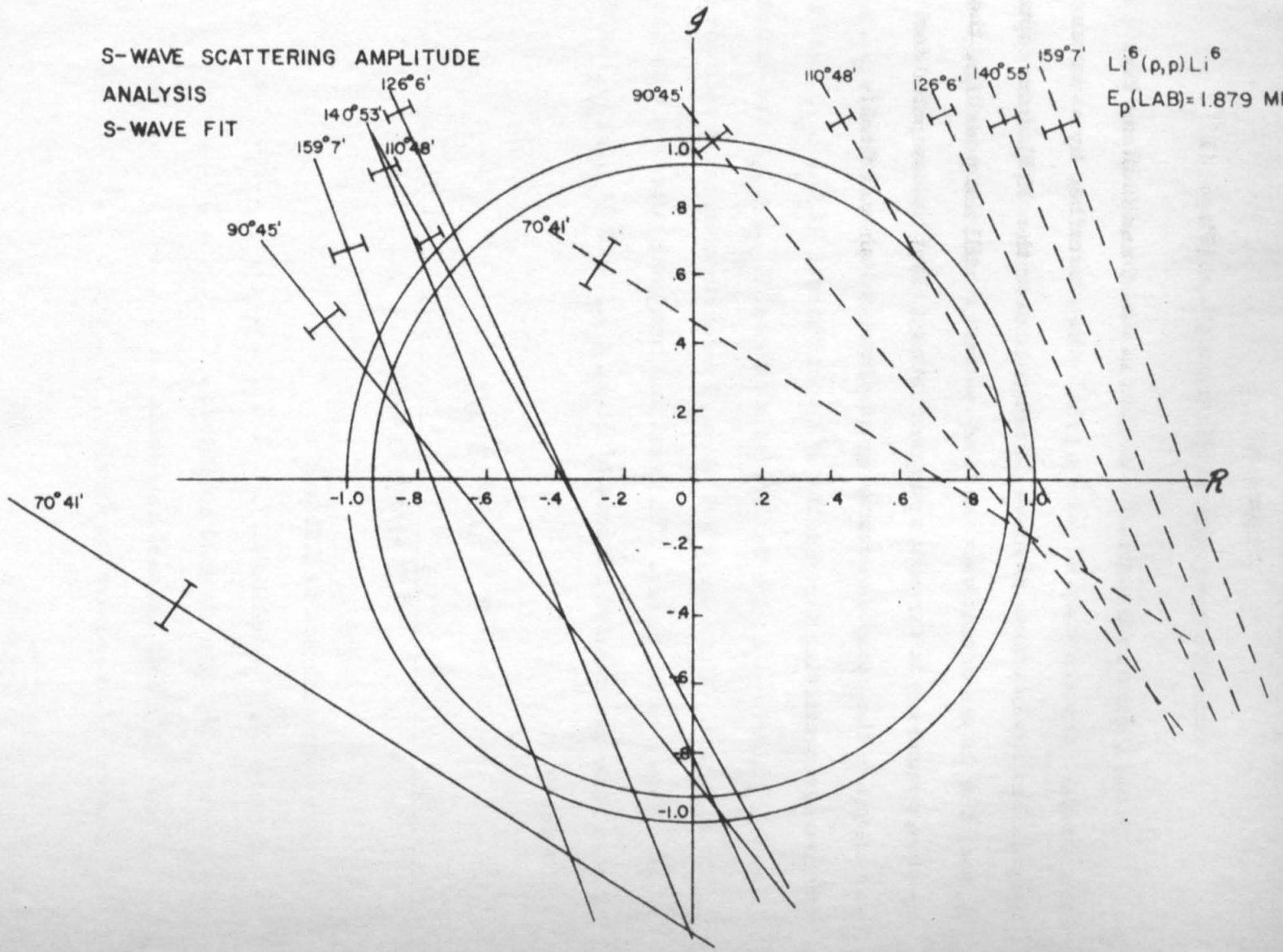
S-WAVE SCATTERING AMPLITUDE
ANALYSIS
S-WAVE FIT
$Li^6(p,p)Li^6$
E_p(LAB)= 1.879 MEV
126°6'
140°53'
159°7'
110°48'
90°45'
70°41'
I
R
1.0
.8
.6
.4
.2
-1.0
-.8
-.6
-.4
-.2
0
-.2
-.4
-.6
-.8
-1.0

Figure 48

Scattering Amplitude Diagram (Page 49)

This figure represents the region in the complex plane within the unit circle. For the case of $Li^6(p, p)Li^6$ the scattering cross section may be written in terms of three complex scattering amplitudes. The assumption is made that only s- and p-waves contribute and that the p-wave scattering is through a single resonant $5/2^-$ state. The energy variations of the complex scattering amplitudes for this state $(f_{5/2}, g_{5/2})$, for s-wave scattering through the 3/2 spin channel $(f_{3/2}, g_{3/2})$ and for s-wave scattering through the 1/2 spin channel $(f_{1/2}, g_{1/2})$ are indicated in the diagram. The energy variation of a fourth complex amplitude (X, Y) is also shown in the figure. The real and imaginary parts of this complex number are related to those of $(f_{1/2}, g_{1/2})$ and $(f_{3/2}, g_{3/2})$ in the following way:

$$X = \frac{1}{3} f_{1/2} + \frac{2}{3} f_{3/2}$$

$$Y = \frac{1}{3} g_{1/2} + \frac{2}{3} g_{3/2}$$

The curves are labeled as follows:

s-wave X, Y amplitude . . . . . •

s-wave 1/2 spin channel amplitude . . . . . o

s-wave 3/2 spin channel amplitude x

p-wave 5/2 resonant amplitude . . . . . △

SCATTERING AMPLITUDE DIAGRAM

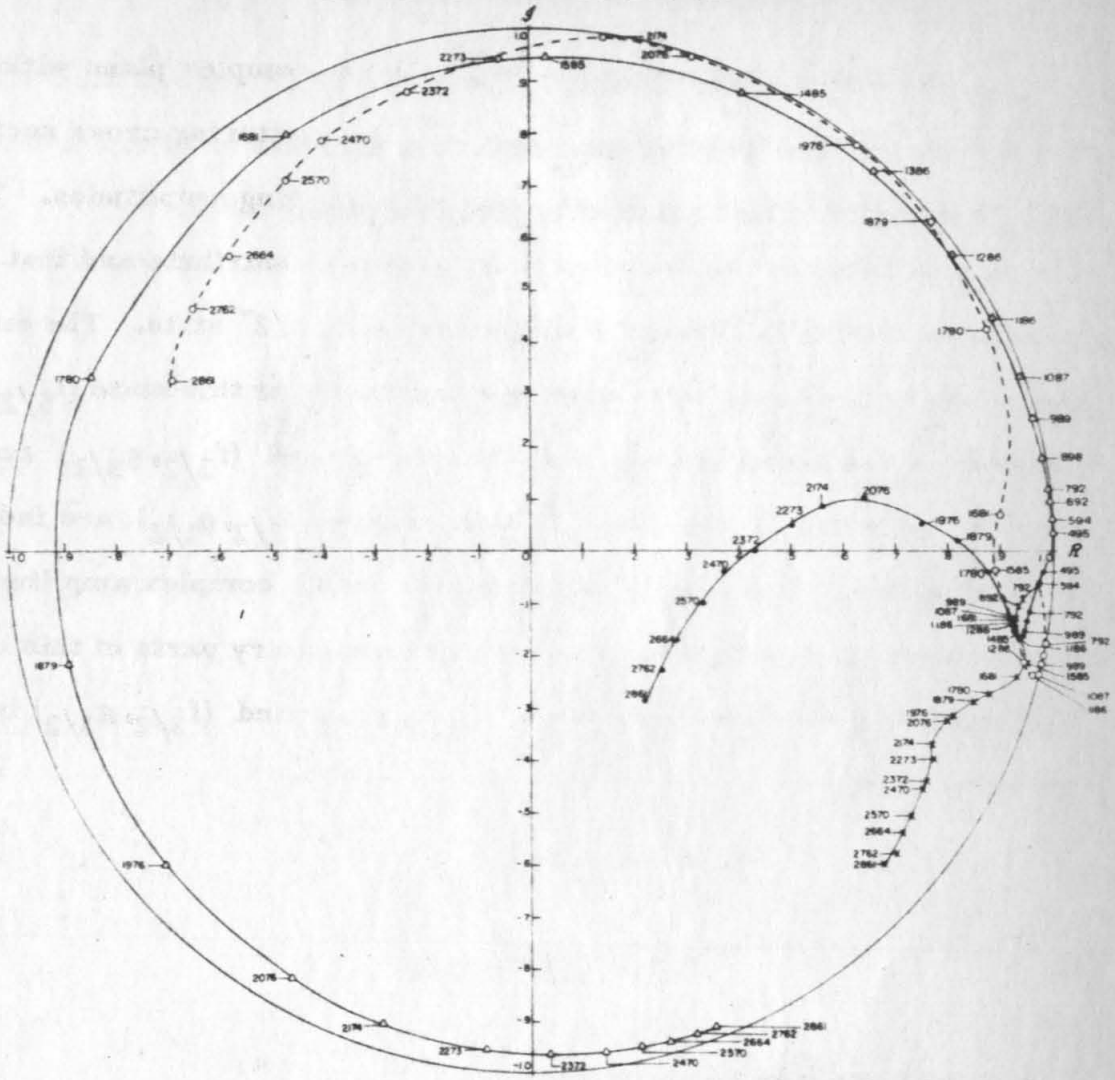

Figure 49

S-wave Scatterimg Amplitude Diagram (Page 51)

In this diagram the six lines $Y = A(\theta)X + C(\theta)$ are plotted where $C(\theta)$ is the s- plus p-wave intercept. An explanation of the procedure used to obtain this final solution is given on pages 49-51.

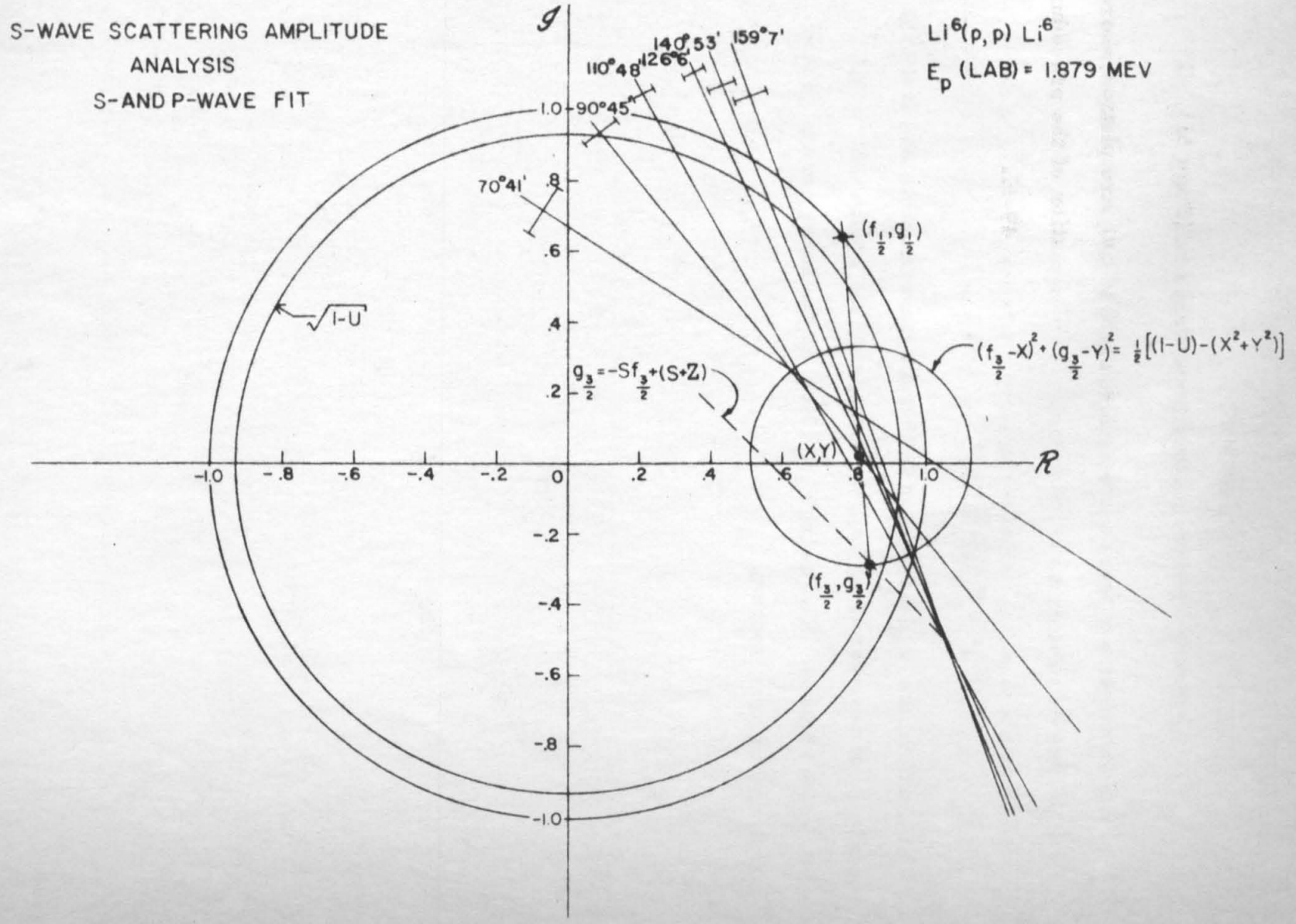
S-WAVE SCATTERING AMPLITUDE
ANALYSIS
S-AND P-WAVE FIT
$Li^6(p,p)\ Li^6$
E_p (LAB) = 1.879 MEV
$\mathcal{I}$
$\mathcal{R}$
110°48'
126°6'
140°53'
159°7'
90°45'
70°41'
$(f_{\frac{1}{2}}, g_{\frac{1}{2}})$
$\sqrt{1-U}$
$g_{\frac{3}{2}} = -Sf_{\frac{3}{2}} + (S+Z)$
$(f_{\frac{3}{2}} - X)^2 + (g_{\frac{3}{2}} - Y)^2 = \frac{1}{2}[(1-U) - (X^2+Y^2)]$
(X,Y)
$(f_{\frac{3}{2}}, g_{\frac{3}{2}})$
1.0
.8
.6
.4
.2
0
-.2
-.4
-.6
-.8
-1.0

Figure 50

S-Wave - P-Wave Interference Cross Section (Page 51)

The s-wave - p-wave interference term in the scattering cross section may be written as

$$\sigma_{s1}(E_1, \theta) = \sigma_{s1}(E_1) \cos \theta$$

The coefficients $\sigma_{s1}(E_1)$ shown in this diagram are obtained from the analysis of the scattering data directly from the coefficient Z as shown on page 51. The energy E_1 (Mev) is the energy of the proton in the laboratory system.

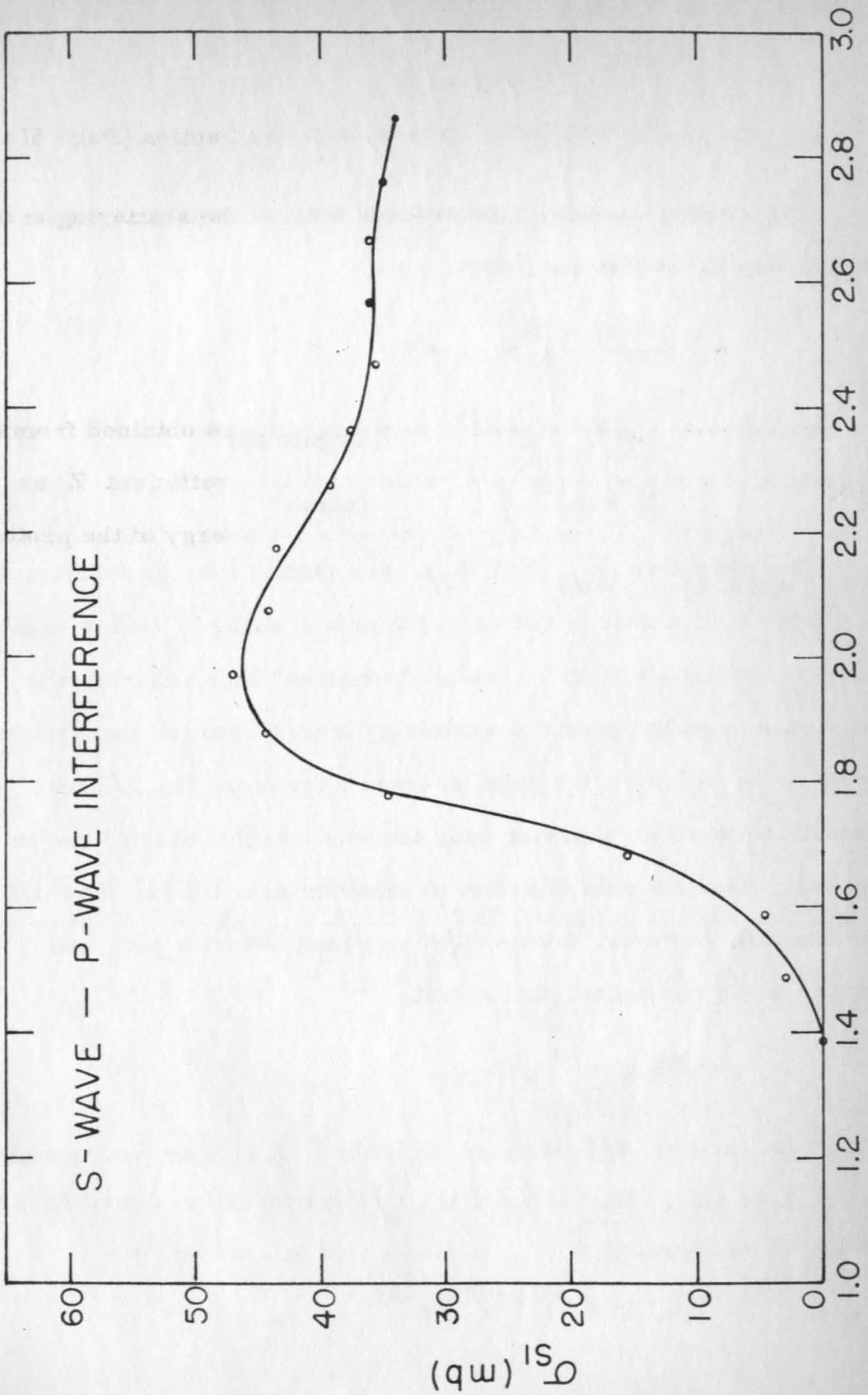
S-WAVE — P-WAVE INTERFERENCE
σ_{si} (mb)
0
10
20
30
40
50
60
1.0
1.2
1.4
1.6
1.8
2.0
2.2
2.4
2.6
2.8
3.0
E_1 (Mev)

Figure 51

S-wave Phase Shifts (Page 35)

The s-wave scattering amplitudes may be written in terms of phase shifts in the following way:

$$f + ig = Ne^{2i\delta'}$$

where

$$N = (f^2 + g^2)^{1/2} \qquad \text{(magnitude)}$$

$$2\delta' = \tan^{-1} \frac{g}{f} \qquad \text{(phase)}$$

The quantities $\delta'_{1/2}$ and $\delta'_{3/2}$ are plotted here as functions of laboratory proton energy and as C. M. proton energy. At low energy both spin channels appear to exhibit "potential" type behavior and would correspond to potential scattering from a charged hard sphere (equation 81) with a radius equal to about 2 fermis. The 3/2 spin channel exhibits this behavior over the whole region studied and in particular does not exhibit resonant behavior near 1 Mev. The 1/2 spin channel, however, does exhibit resonant behavior and would correspond to a resonant phase shift,

$$\delta = \tan^{-1} \frac{\Gamma}{2(E_R - E)}$$

which goes through $\pi/2$ at about $E_p(\text{Lab}) \simeq 2.76$ Mev with a width of $\Gamma \simeq 1.44$ Mev. This is valid if $\Gamma_p/\Gamma \approx 1$ for the resonance since then equation 79 becomes

$$f + ig = e^{2i(\phi + \delta)} = e^{2i\delta'}$$

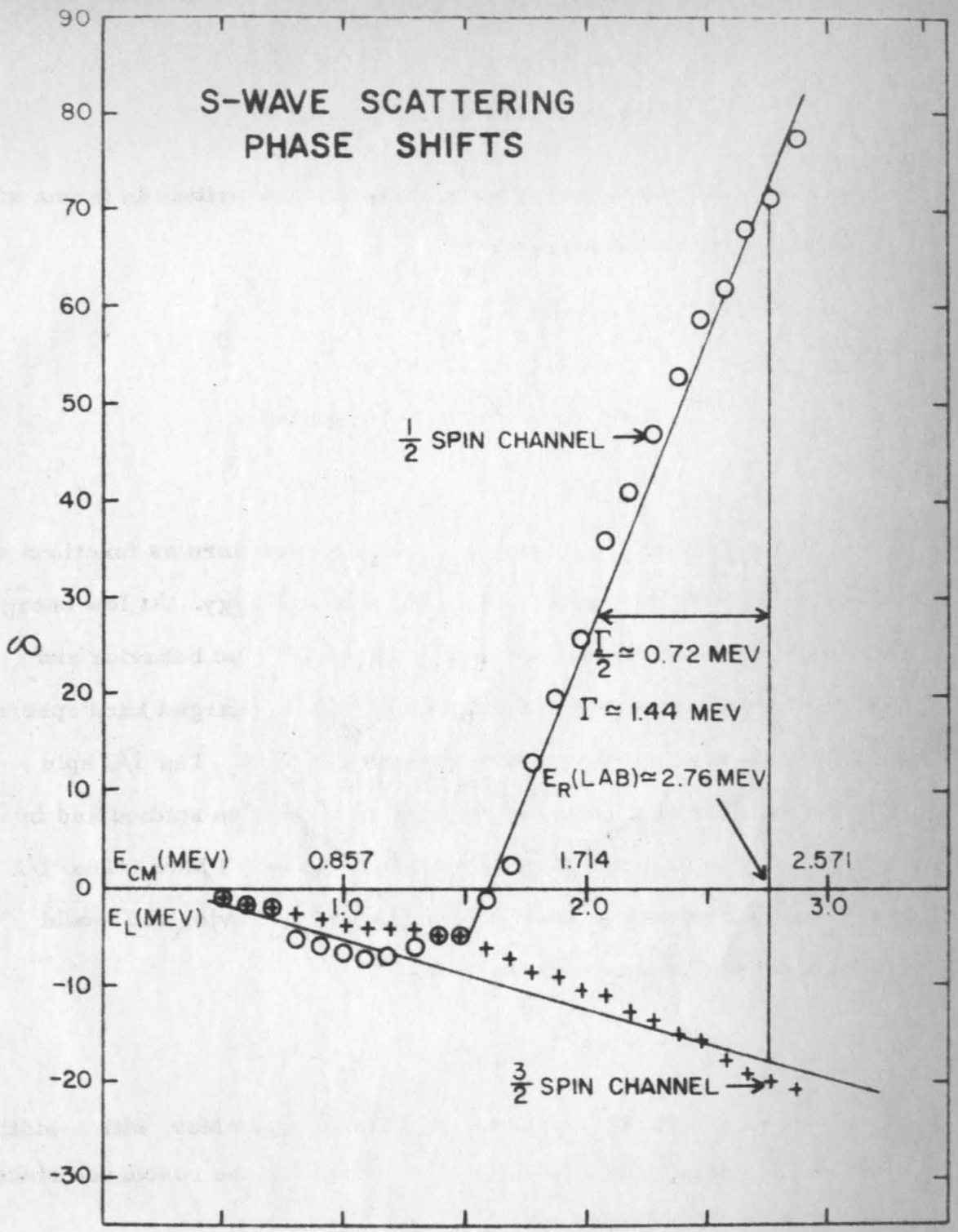
S-WAVE SCATTERING
PHASE SHIFTS
90
80
70
60
50
40
30
20
10
0
-10
-20
-30
δ
1/2 SPIN CHANNEL
Γ/2 ≃ 0.72 MEV
Γ ≃ 1.44 MEV
E_R(LAB)≃2.76 MEV
E_CM(MEV)
0.857
1.714
2.571
E_L(MEV)
1.0
2.0
3.0
3/2 SPIN CHANNEL